Deformation Behavior of Co-Sputtered and Nanolaminated Metal/Ceramic Composites

by

Somya Singh

A Dissertation Presented in Partial Fulfillment
of the Requirements for the Degree
Doctor of Philosophy

Approved November 2018 by the
Graduate Supervisory Committee:

Nikhilesh Chawla, Chair
Narayanan Neithalath
Yang Jiao
Nathan A. Mara

ARIZONA STATE UNIVERSITY

December 2018

ABSTRACT

Nanolaminate materials are layered composites with layer thickness ≤ 100 nm. They exhibit unique properties due to their small length scale, the presence of a high number of interfaces and the effect of imposed constraint. This thesis focuses on the mechanical behavior of Al/SiC nanolaminates. The high strength of ceramics combined with the ductility of Al makes this combination desirable. Al/SiC nanolaminates were synthesized through magnetron sputtering and have an overall thickness of ~ 20 μm which limits the characterization techniques to microscale testing methods. A large amount of work has already been done towards evaluating their mechanical properties under indentation loading and micropillar compression. The effects of temperature, orientation and layer thickness have been well established. Al/SiC nanolaminates exhibited a flaw dependent deformation, anisotropy with respect to loading direction and strengthening due to imposed constraint. However, the mechanical behavior of nanolaminates under tension and fatigue loading has not yet been studied which is critical for obtaining a complete understanding of their deformation behavior. This thesis fills this gap and presents experiments which were conducted to gain an insight into the behavior of nanolaminates under tensile and cyclic loading. The effect of layer thickness, tension-compression asymmetry and effect of a wavy microstructure on mechanical response have been presented. Further, results on *in situ* micropillar compression using lab-based X-ray microscope through novel experimental design are also presented. This was the first time when a resolution of 50 nms was achieved during *in situ* micropillar compression in a lab-based setup. Pores present in the microstructure were characterized in 3D and sites of damage initiation were correlated with the channel of pores present in the microstructure.

The understanding of these deformation mechanisms paved way for the development of co-sputtered Al/SiC composites. For these composites, Al and SiC were sputtered together in a layer. The effect of change in the atomic fraction of SiC on the microstructure and mechanical properties were evaluated. Extensive microstructural characterization was performed at the nanoscale level and Al nanocrystalline aggregates were observed dispersed in an amorphous matrix. The modulus and hardness of co-sputtered composites were much higher than their traditional counterparts owing to denser atomic packing and the absence of synthesis induced defects such as pores and columnar boundaries.

DEDICATION

To my sister Shrishti and my brother Udbhav, for being a constant source of happiness in my life.

ACKNOWLEDGMENTS

First and foremost, I would like to thank my advisor, Professor Nikhilesh Chawla for his constant guidance and support. I am very thankful for all the opportunities he gave me, for motivating me to think independently and for encouraging me to come with new ideas to push boundaries in the field. I would also like to express my gratitude towards members of my committee, Dr. Nathan A. Mara, Dr. Yang Jiao, and Dr. Narayanan Neithalath for taking out time to evaluate my doctoral research. I would like to acknowledge the financial support of the National Science Foundation, DMR-Ceramics Program (Grant Number DMR-1647568, Dr. Lynnette Madsen, Program Manager). I would also like to acknowledge our collaborators at the Center for Integrated Nanotechnologies (CINT) in Los Alamos National Laboratory, Dr. Nate Mara and Mr. Kevin Baldwin in areas of sample preparation. I also gratefully acknowledge the facilities within the Center for 4D Materials Science and the Lerory Erying Center for Solid State Science at Arizona State University.

In addition, I would like to acknowledge the advice of Research Scientist, Dr. Jason Williams at various stages during my research work. I would like to thank all my friends in Professor Chawla's Research Group for making this journey memorable. A special thanks to Sudhanshu, Shashank and Carl for their guidance. And last, I would like to thank my family: my grandparents for sharing their unconditional love, my parents for always believing in me, my sister and brother for always encouraging me.

TABLE OF CONTENTS

CHAPTER Page

CHAPTER Page

LIST OF TABLES

Table Page

LIST OF FIGURES

Figure Page

Figure Page

Figure Page

Figure Page

CHAPTER 1

INTRODUCTION

Composite materials are a blend of two or more distinct constituent phases whose combination often renders properties that are superior to that of the individual components. Laminate composites consist of layered dissimilar materials that span across length scales in both natural and engineered form. Certain geological formations such as abalone shells are examples of natural laminates whereas applications in aerospace utilize certain man-made laminates as shown in Figure 1.

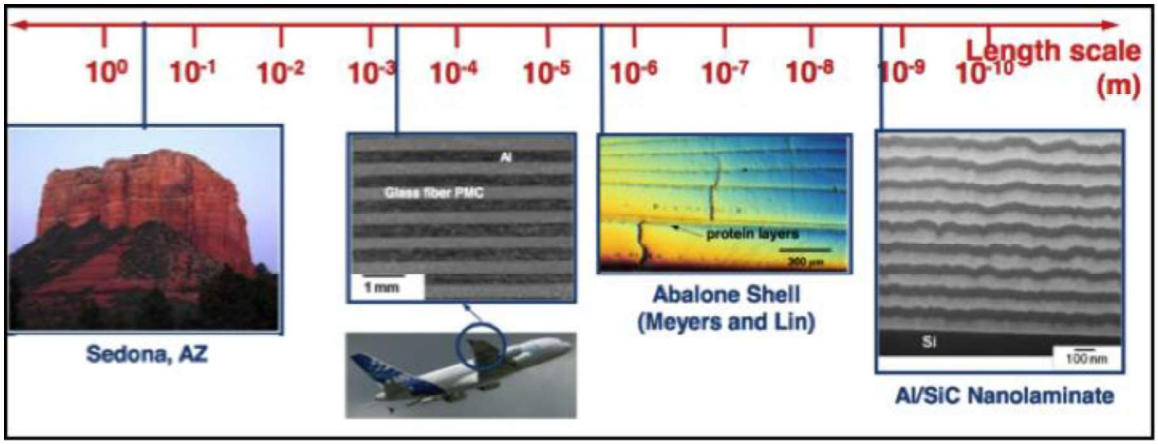

Figure 1: Examples of natural and manmade laminate composite structures over a wide range of length scales (after Chawla, 2008).

In the present work, laminates having layer thickness on the order of nanometers are of interest. In the last two decades, materials designed at the nanoscale have exhibited exciting properties including extremely high strength, toughness, wear resistance, and biocompatibility (Hickey et al. 2002; Windt & Bellotti 2009; X. Deng et al. 2005). Diamond like carbon (DLC) coatings, thin film metallic glasses, nanolayered structures,

nanotwinned metals etc. have been developed and studied (Escudeiro et al. 2015; Apreutesei et al. 2014; Pei et al. 2005; Schuster et al. 2008; Chou et al. 2010; Ye et al. 2012; Dao et al. 2006). A lot of work has been done in achieving films with high strength as well as toughness through addition of ductile phase (Musil et al. 2001; Mišina et al. 1998), nanograin structure design (Veprek et al. 2000; Procházka et al. 2004) and phase transformation induced toughening (Ji et al. 2001). However, among these, nanolayered structures are particularly interesting as their microstructure can be conveniently tailored by changing the composition and layer thickness. Thus, designing nanolayered structures is an attractive strategy for developing a new generation of multifunctional materials with wide range of applications.

This work focuses on metal-ceramic nanolaminates containing alternating layers of Al and SiC, having layer thickness ≤ 100 nm. These materials are interesting due to the large elastic modulus mismatch between the layers leading to plastic deformation of metals under extreme amounts of constraint. Moreover, the ductility of metals along with the stiffness and high temperature properties of ceramics offers a promising combination.

However, one of the limitations associated with nanolayered structures is that their mode of synthesis, physical vapor deposition (PVD), which is a time consuming and complicated process. Alternate methods also follow the top down or bottom up approach such as electrodeposition (Ross 1994), solidification (Shen et al. 2005; Wang et al. 2011) and accumulative roll bonding (Carpenter et al. 2012). Some of these techniques add a restriction on the sample thickness to tens of microns. Mechanical behavior of nanolaminates is thus being studied through micromechanical testing techniques. These

techniques range from a simple nanoindentation testing (Pharr et al. 1992), which requires minimal sample preparation to extremely complicated focused ion beam (FIB) milled specimens, which require sophisticated experimental design and execution. Since it is imperative to obtain a complete understanding of the deformation mechanism to establish structure-property relationships, focus has increased on developing and perfecting these micromechanical testing techniques. Special importance has been given to *in situ* studies, which provide real time deformation information using scanning electron microscope (SEM), transmission electron microscope (TEM) and X-ray tomography. These studies range in scale from atomic level to several microns, from giving 2D surface information to visualization of the whole sample volume.

The properties of nanolaminates depend on its constituents: metal, ceramic, metallic glass etc. With a wide range of available materials the possibilities of desirable combinations are endless. A majority of the work done till now focuses on metal-metal combinations of nanolaminates. Their strengthening as well as deformation mechanisms are well established. However, such extensive work has not been done for metal-ceramic nanolaminates. The huge stiffness difference in their constituent layers makes this problem more complex by making their behavior extremely anisotropic.

This work is aimed at creating a better understanding of the structure-property relationships of Al/SiC nanolaminates. It answers some very important questions for metal/ceramic nanolaminates that have not been previously investigated. The nature of microstructural defects present in nanolaminates was studied through 3D X-ray microscopy. Its effect on the mechanical response to the applied load was also evaluated

through interrupted *in situ* micropillar compression. Further, the deformation of nanolaminates under tensile loading and the tension-compression asymmetry in its mechanical behavior was evaluated. Microtensile testing has not been performed earlier owing to the complex nature of experimental design and execution that is required. The mechanical response of nanolaminates under cyclic loading was also studied to probe into the effect of imposed constraints and pores present in the microstructure under fatigue loading. A number of compled experiments were designed to answer these questions and hence, this work also presents information about the experimental design of testing techniques itself.

Further, these insights into the mechanical behavior of Al/SiC nanolaminates were used to design a new class of materials containing co-sputtered layer of aluminum and silicon carbide. Different compositions of co-sputtered samples were synthesized and the evolution of the microstructure was studied with respect to atomic fraction of SiC. The mechanical properties of these co-sputtered samples were evaluated and correlated with the sample composition and microstructure.

CHAPTER 2

LITERATURE REVIEW

2.1 Nanolaminate Materials

There are three important parameters that control the mechanical behavior of nanolaminates: type of constituents (metal, ceramic, metallic glass), layer thickness and type of interface (coherent, semicoherent and incoherent). To date, a number of metal-metal (Chen et al. 2012; Mara et al. 2008; Carpenter et al. 2012; Misra & Hoagland 2007), ceramic-ceramic (Freyman & Chung 2008; Chu & Barnett 1995; Wiklund et al. 1997) and metal-ceramic (Mayer et al. 2015; X. Deng et al. 2005; Mook et al. 2013; Pathak et al. 2015; Bhattacharyya et al. 2008; Bhattacharyya et al. 2011; Han et al. 2009; Wang et al. 2016; Wang et al. 2015; Phillips et al. 2003) nanolaminates have been developed. Each of the above mentioned parameters contribute towards strengthening of nanolaminates as discussed in the next section thus nanolaminates are expected to have superior properties than their bulk counterparts. For example, bulk metal-ceramic composites exhibit limited ductility due to presence of triaxial tensile stresses (Llorca & Poza 1994). These tensile stresses generate from the constraint imposed by stiff ceramic component and lead to reduction in fracture toughness of the composite. In nanolaminates, however, the layer thicknesses can be altered with ease and therefore is a promising route to obtain the desirable balance of strength and toughness.

2.2 Strengthening of Nanolaminates

One of the most important reasons for strengthening of nanolaminates is the reduced layer thickness. For metallic nanolaminates, the grain size usually scales with the layer thickness and therefore is expected to have a direct effect on the mechanical behavior (Li et al. 2016). For ceramic layers as well, small layer thickness indicates lesser number of defects and therefore superior mechanical property (Callisti & Polcar 2017). In metallic layers, with a decrease in layer thickness the deformation mechanism changes as shown in Figure 2 (Misra & Hoagland 2007). When the individual layer thickness is greater than 50 nm for nanocrsytalline systems, nanolaminate strength usually follows the traditional Hall-Petch (H-P) relationship:

$$\sigma_y = \sigma_0 + kd^{-\frac{1}{2}} \tag{1}$$

Here, σ_0 is the yield stress when the grain size is infinitely large and d is the grain size. These grains are big enough to accommodate dislocation pile-up, the extent of which is dependent on layer thickness. Hence, nanolaminate strength follows the same linear trend as seen for bulk materials.

However, with the reduction of layer thickness, a deviation from the linear trend is seen. This is because the grains are not large enough to accommodate dislocations for layer thickness < 50 nm. The deformation mode therefore changes to confined layer slip (CLS), as shown in the figure. Here the dislocations are bowed between the interfaces and this Orowan bowing leads to strengthening. Finally, at extremely small layer thickness the dislocation cuts through the interface and limited to no increase is seen in

the strength.

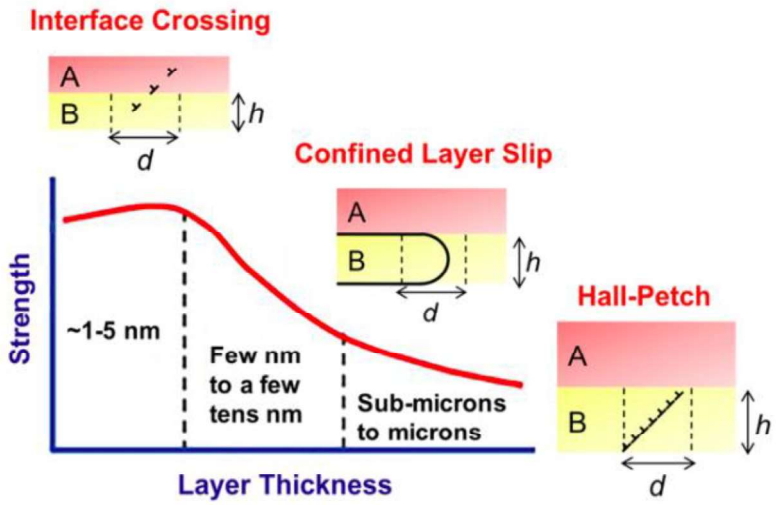

Figure 2: Changes in the deformation mechanism with respect to changes in layer thickness. Reprinted from (Misra & Hoagland 2007).

For metal-ceramic nanolaminates however the interface-crossing regime is not feasible. Dislocation motion is impossible in the amorphous ceramic layers and highly unlikely in the crystalline ceramic layers. Therefore, the metal-ceramic interface is impenetrable to dislocations.

The effect of layer thickness and volume fraction differs remarkably with change in system. Wang et al. showed that with increase in Fe volume fraction the hardness value does not change for Fe/VC nanolaminates (Figure 3(a)) (Wang et al. 2016). However, in some other cases, such as Cu/TiN (Misra et al. 1998), strength is influenced by volume fraction. This is mainly because of the difference in their microstructure. The layer thickness in Fe/VC nanolaminates is less than 10 nm as shown in Figure 3(b) and

they reported to have a similar modulus with change in the Fe thickness fraction. Therefore, it was speculated that the hardness of these samples was also independent of layer thickness. However, in the other cases a columnar grain structure is observed and therefore with a decrease in layer thickness an increase in hardness is observed. Similar discrepancy was reported by Pathak et al. for Al/TiN and Cu/TiN systems, highlighting the competing forces of interface and grain size in controlling the mechanical property (Pathak et al. 2015). The grain size of Al/TiN ~ 100 nm was larger than the layer thickness hence the hardness is governed by layer thickness. However, the grain size of Cu/TiN was smaller than the layer thickness making grain size the controlling parameter for hardness. Therefore, a strikingly different behavior is seen for metal/ceramic nanolaminates depending on the controlling parameter.

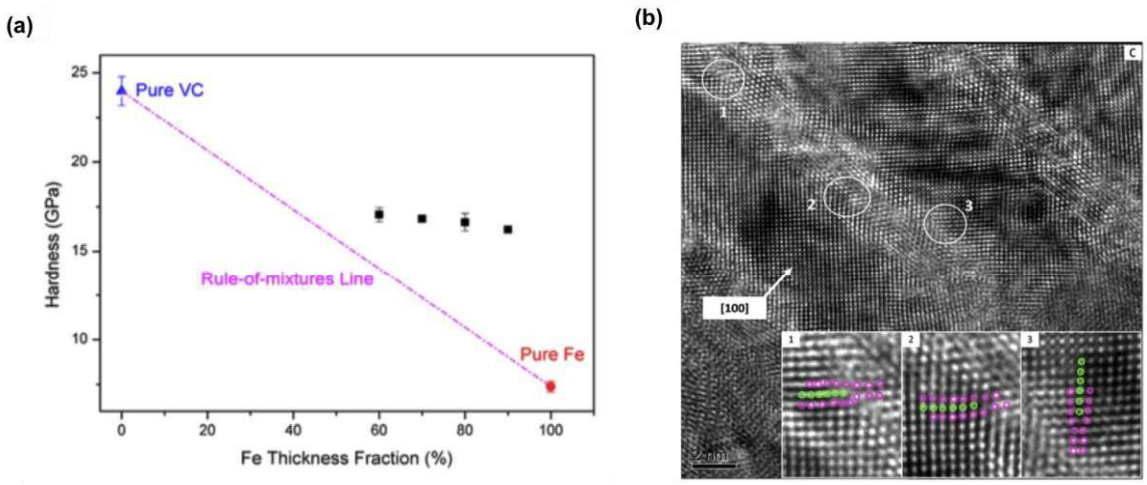

Figure 3: (a) Hardness versus volume fraction for Fe/VC nanolaminates. (b) high resolution TEM image showing the Fe [100] direction. Reprinted from (Wang et al. 2016).

Another strengthening mechanism largely responsible for the observed strain hardening in metal-ceramic nanolaminates is the effect of constraint imposed by stiff ceramic layers on soft metallic layers. Under an applied stress, metallic layers flow plastically however the ceramic layer limits this in order to maintain the interface intact. Hydrostatic stresses are developed and delay the onset of plasticity leading to strain hardening in nanolaminates. The extent of strain hardening depends on the type of interface as well as the layer thickness. A significant increase in strength was reported with decrease in layer thickness of Al/TiN nanolaminates as shown in Figure 4 (Wang & Misra 2014). This was primarily attributed to closely spaced dislocation arrays, which lead to compressive stresses in Al layer and tensile stresses in TiN layer. A Schmidt factor was introduced to calculate shear stress and it was reported that with decrease in layer thickness and thickness ratio plasticity is maximized. Similar effect of layer thickness was observed in Cu/TiN nanolaminates (Raghavan et al. 2014). The nature of interface also plays a significant role in determining the amount of strain hardening. It was reported that for a weak interface strain hardening is not possible in Al/SiC nanolaminates and the micropillar yields at the yield stress of Al (Lotfian et al. 2013).

Multilayer strengthening depends on the nature of interface not just for the purpose of constraint. Depending on the system, interface can act as sources, sinks or storage sites of dislocations (Zhang et al. 2012). In addition, they also help in toughening by crack blunting, crack deflection and ductile interlayer ligament bridging (Wiklund et al. 1997). However, crack blunting and bridging effect is observed mainly when passing through metallic layer. For ceramic-ceramic nanolayers the toughening mechanism

mainly relies on crack deflection, as shown in Figure 5 (Wiklund et al. 1997). Therefore, it is essential to design the nanolayers i.e. constituents and layer thickness while keeping in mind the benefit as well as limitation of individual components.

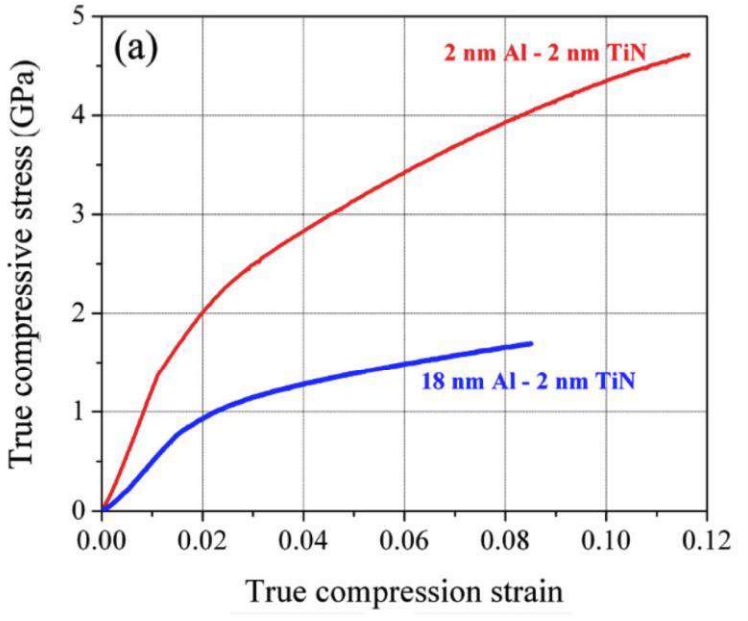

Figure 4: Stress-Strain curve for Al/TiN nanolaminates showing the effect of strain hardening with reduction in layer thickness. Reprinted from (Wang & Misra 2014).

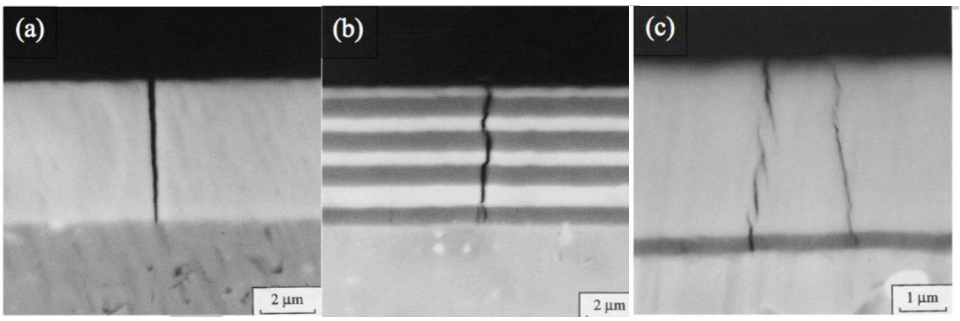

Figure 5: (a) crack deflection in a single layer of NbN film, (b) microscale NbN-TiN layers and (c) nanoscale NbN-TiN layers. Reprinted from (Wiklund et al. 1997).

2.3 Literature Review of Al/SiC Nanolaminates

2.3.1 Synthesis and Microstructural Characterization of Al/SiC Nanolaminates

Al/SiC nanaolaminates have desirable mechanical properties that can be tailored by changing the individual layer thicknesses and volume fractions of the individual components. These materials are synthesized through magnetron sputtering on Si (111) substrate. This is one of the most widely used PVD techniques for the synthesis of thin films and multilayers. The base pressure of the sputtering unit was maintained at 10^{-7} Torr and Ar working pressure of 3 mTorr was used. Al and SiC layers were sputtered at a DC and RF power of 95 W and 215 W respectively. Before starting the deposition, the targets were sputtered for 10 mins to remove any contamination that might have been present. For this step, a power of 40 W was used for Al target and 95 W for SiC target. In order to obtain a uniform layer thickness, the sample holder was continuously rotated. Al and SiC layers were deposited one after the other with the deposition rates being approximately 7.5 nm/min for Al and 3.9 nm/min for SiC. Three series of nanolaminates were synthesized as shown in Table 1. In series I and II, the layer thicknesses of SiC and Al were maintained constant at 50 nm respectively. In series III, the volume fraction of both components was maintained at 0.5 by depositing same thickness of Al and SiC layers. Hence by keeping one of the components constant for a series, the effect of change in layer thickness as well as volume fraction could be established individually. For the ease of discussion, the samples were named as Al<layer thickness in nm>SiC<layer thickness in nm>. For example, Al50SiC100 refers to a nanolaminate from series II where layer thickness of Al is 50 nm and that of SiC is 100 nm. As can be

seen from the table, the layer thickness of the components was varied between 10 nm and 100 nm. This huge range of variation allowed for a considerable change in volume fractions of the individual components. Therefore, the effect of layer thickness, volume fraction and constraint could be thoroughly studied.

The microstructural characterization of Al/SiC nanolaminates has been performed using SEM, FIB cross-sections and TEM imaging. Bright field TEM images of series I and series II samples have been shown in Figure 6. It can be noted that the measured layer thicknesses were slightly different from the desired thicknesses. Based on the measured values, the actual volume fraction of Al was calculated as shown in the table.

Series	Sample	Thickness (μm)	Number of bilayers	t_{Al} (nm)	t_{SiC} (nm)	VAl
S1	Al10SiC50	~15	250	10±1	46±3	0.17
	Al25SiC50	~13.3	175	21±1	44±2	0.33
	Al50SiC50	~15	150	52±2	44±2	0.50
	Al100SiC50	~15	100	90±8	48±3	0.67
S2	Al50SiC2	~13.5	260	50	2	0.96
	Al50SiC10	~15	250	50	10	0.83
	Al50SiC25	~13	175	50	25	0.67
	Al50SiC100	~15	100	50	100	0.33
S3	Al100SiC100	~17	85	100±6	148±5	0.50
	Al25SiC25	~14	280	25±4	25±7	0.50
	Al10SiC10	~12	600	8±1	11±2	0.50

Table 1: Layer thickness, number of bilayers and volume fraction of aluminum for Series I, II and III nanolaminates. Reprinted from (Yang et al. 2016).

SiC was amorphous in nature and Al was nanocrystalline with a strong (111) peak as reported by the X-ray diffraction data (Xin Deng et al. 2005). Therefore, with the

deposition of SiC layer, the growth of nanocrystalline Al was interrupted at each interface. This phenomenon is responsible for the columnar growth mechanism observed in Al/SiC nanaolaminates. It also plays a role in determining the nanograin size of aluminum, which plays a key role in its mechanical property, mainly the yield strength. It was noted that the vertical grain size scaled with the layer thickness and saw a continuous increase when the layer thickness increased from 10 nm to 100 nm (Yang et al. 2016). However, the lateral grain size was larger than the layer thickness when thickness was less than 25 nm and lesser than it when the layer thickness was more than 50 nm (Yang et al. 2016).

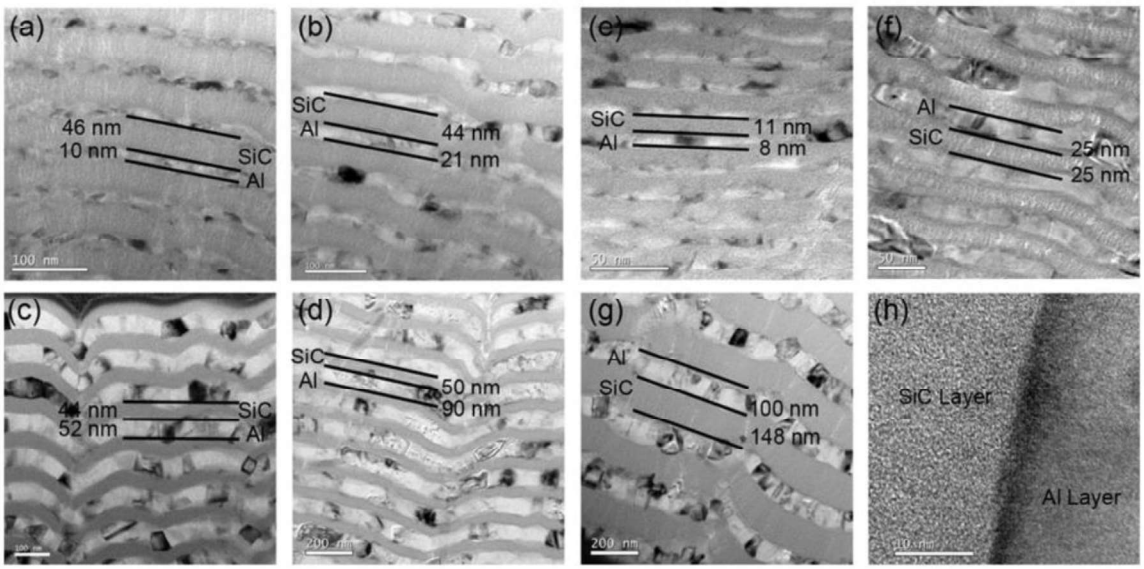

Figure 6: Bright field TEM images of series I, series II nanolaminates and interface. Reprinted from (Yang et al. 2016).

The effect of columnar growth mechanism is manifested in the form of waviness of the deposited layers also. Al nanograins have different heights and the deposited SiC

layer replicates the top surface of Al thus leading to surface roughness in the sample. When a number of these layers are deposited these differences get amplified leading to formation crests and troughs in the microstructure. Therefore, the regions present in the troughs are shadowed by the neighboring part of microstructure. These regions receive insufficient amount of flux of incoming atoms and lead to formation of pores in the microstructure. This phenomenon has been discussed in detail in the structure zone model for sputtering process (Thornton 1974).

Another important feature of a nanolayered structure is its interface. The areal fraction of interfaces increases with reduction of bilayer thickness, since the total thickness of nanolaminates is maintained between 15 μms to 20 μms. The interfaces between Al and SiC were devoid of intermetallics; no evidence of chemical reaction was found between the two layers (Yang et al. 2016). Even for high temperature mechanical tests, the interface remained intact and devoid of reaction products (Lotfian et al. 2013).

2.3.2 Mechanical Properties of Al/SiC Nanolaminates

A number of microscale testing techniques have been developed to characterize materials with limited volumes, as they cannot be tested through conventional methods. One of the most common techniques used for obtaining material hardness and modulus is nanoindentation (Pharr et al. 1992). Here, a Berkovich tip is used for obtaining site-specific properties from the load-displacement curve. Even though this technique is widely used for all class of materials, the generation of complex stress states results in difficulty of interpretation of results. On the other hand, micropillar compression is one

of the techniques commonly used to characterize material behavior under uniaxial stress (Uchic et al. 2009). Focused ion beam milling is used for fabricating a cylindrical pillar and an indenter with flat punch is used for compression. This technique has been used to study the operative damage mechanisms at room temperature as well as high temperatures (Lotfian et al. 2013; C. R. Mayer et al. 2016). Some methods have also been developed for tensile testing at these length scales such as bending cantilever beams and pulling dog-bone shaped samples (Yang et al. 2014; Kim et al. 2009). Additionally, for measurement of fracture toughness, researchers have come up with methods such as single notch cantilever beam, double notch cantilever beams, pillar splitting etc. (Liu et al. 2013; Sebastiani et al. 2014; Jaya et al. 2015; Matoy et al. 2009). Fatigue life and crack propagation studies have also been designed for miniature sized samples (Kwak et al. 2010; Hocheng et al. 2004; Physics et al. 1999; Kraft et al. 2001; Limodin et al. 2009; Cavaliere 2010). Fracture of microcantilever beams has been used to study the fatigue life of the samples. Here, drop in stiffness values is used to study the crack initiation and growth of the materials. Kraft et al. (Kraft et al. 2001) showed that failure was accompanied by formation of transgrannular extrusions and intergrannular cracks and a direct dependence on the film thickness was seen. Some of these experiments were performed for Al/SiC nanolaminates to understand their deformation behavior and have been discussed in detail below.

Nanoindentation tests have been performed to evaluate the mechanical properties of Al and SiC layers individually as well as for multilayered samples. It was reported that due to the substrate effect from Si, plateau in the modulus versus displacement graph was

not attained. The authors extracted the properties of the individual films by using a numerical model (Xin Deng et al. 2005). The modulus and hardness of Al and SiC films was less than their respective bulk values and it was reported that the synthesis induced defects are responsible for this decrease (X. Deng et al. 2005).

As shown in Figure 7, nanoindentation on the multilayer samples also showed the effect of Si substrate. The modulus values stabilized over the displacement range of 100–200 nm, which was taken to be the value for the entire composite. Further increase in indentation depth led to an increase in modulus due to considerable contribution from the Si substrate (Chawla et al. 2008). Finally, at very large depths around 1700 nm, discontinuity in the load-displacement curve was reported owing to the damage at the multilayer–Si substrate interface and within the substrate (Chawla et al. 2008).

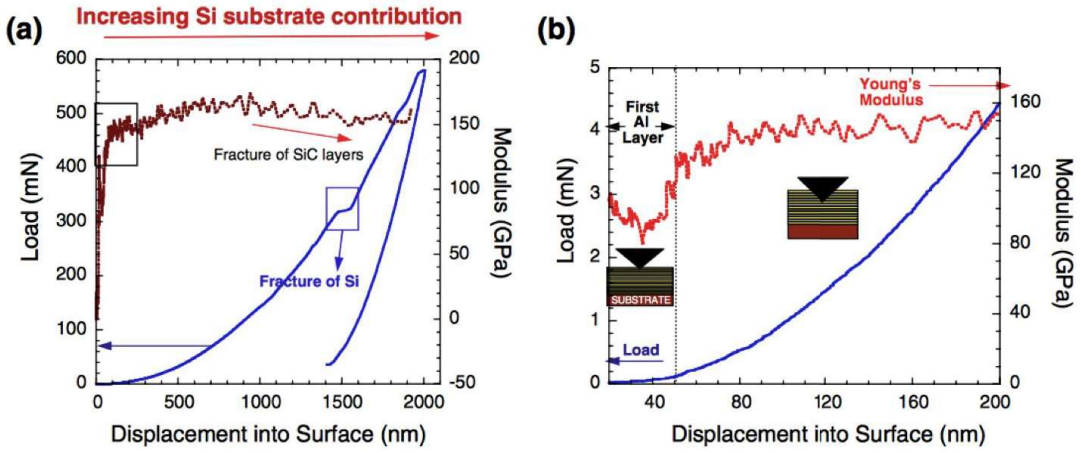

Figure 7 (a) Load versus displacement curve from nanoindentation of Al50SiC50 composite. (b) Magnified view of the boxed part, showing the effect of first Al layer (Chawla et al. 2008).

On comparing the properties of samples containing different volume fractions of individual components, a linear decrease in the hardness values was reported with increase in

volume fraction of Al at all temperatures as shown in Figure 8 (a) (Lotfian et al. 2014; Yang et al. 2016). This was due to a decrease in content of stiffer SiC as well as the diminished effect of constraint imposed by SiC layer. For the same volume fraction, hardness values didn't change on reducing the layer thickness. The increase in yield strength of Al layers was compensated by the decrease in flexural modulus of SiC layer (Lotfian et al. 2014). Thus, decreasing the layer thickness of Al/SiC nanolaminates is not an effective technique of improving the hardness of the samples. From the H/E evaluation, it was concluded that below V_{Al} of 0.5, elastic deformation of SiC is the controlling parameter of defromation and above V_{Al} of 0.5, plastic deformation of Al is the controlling factor, (Figure 8(b)) (Yang et al. 2016; Lotfian et al. 2014).

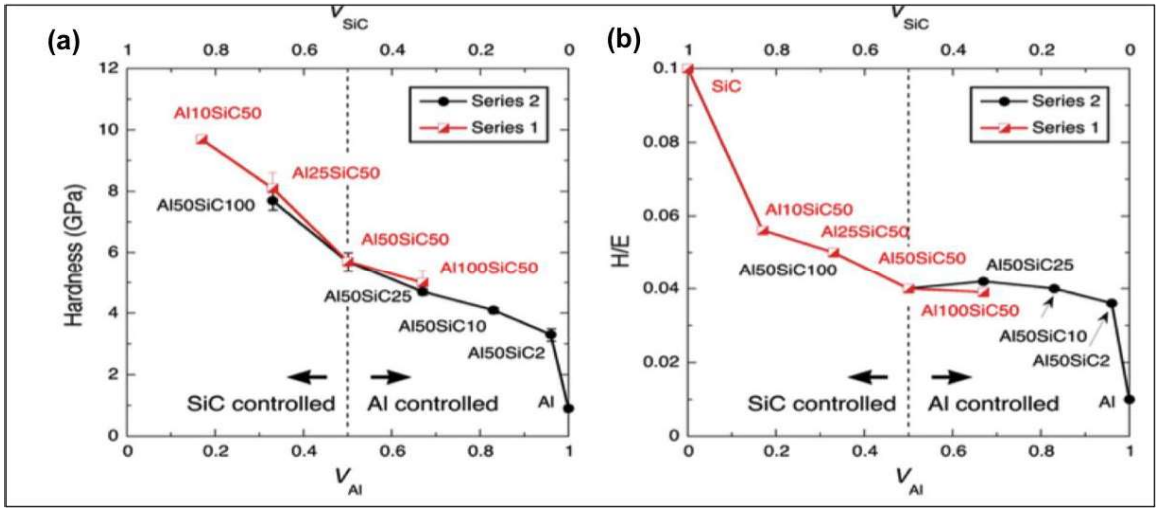

Figure 8: (a) Hardness of the nanolaminate samples with respect to the volume fraction of Al layer. (b) Hardness and H/E ratio of the samples is controlled by the elastic deformation of SiC below V_{Al} of 0.5 and plastic deformation of Al above V_{Al} of 0.5. Reprinted from (Lotfian et al. 2014).

Under indentation loading, deformation in the nanolaminate system occurs through cracking of SiC layers due to localized shear bands and the flow of Al layers. It was seen that the strength of the Al/SiC interface is higher than the Al layer as the voids were formed in the Al layer and not at the interface (Yang et al. 2016). Work has also been done to study the orientation dependence of nanoindentation by comparing the results of layers oriented at 0°, 45° and 90° to the applied load (C. Mayer et al. 2016). The Young's modulus and hardness were the highest for the samples having the layers parallel to the loading direction, followed by the perpendicular and inclined directions respectively. It was reported that in the parallel and inclined directions, the waviness of the layers led to a premature buckling and cracking of the SiC layers. This was also confirmed through finite element modeling of these layers. Moreover, the variation in these results was little less than what is expected from laminate theory; this was primarily due to the multi axial stress state from nanoindentation and the waviness in the layers (C. Mayer et al. 2016).

To evaluate the strength of nanolaminates under uniaxial compressive loading, micropillars from the nanolaminate materials were fabricated from both annular milling and lathe milling. The resultant from the two techniques was micropillars with and without taper respectively, Figure 9. Though the strength of these pillars was fairly similar, the tapered pillar had higher strain-to-failure due to strain hardening (Singh et al. 2010). Even though lathe milling yields taper-free micropillars, it should be noted that this technique is more susceptible to Ga^{+} ion damage due to unfavorable angles required.

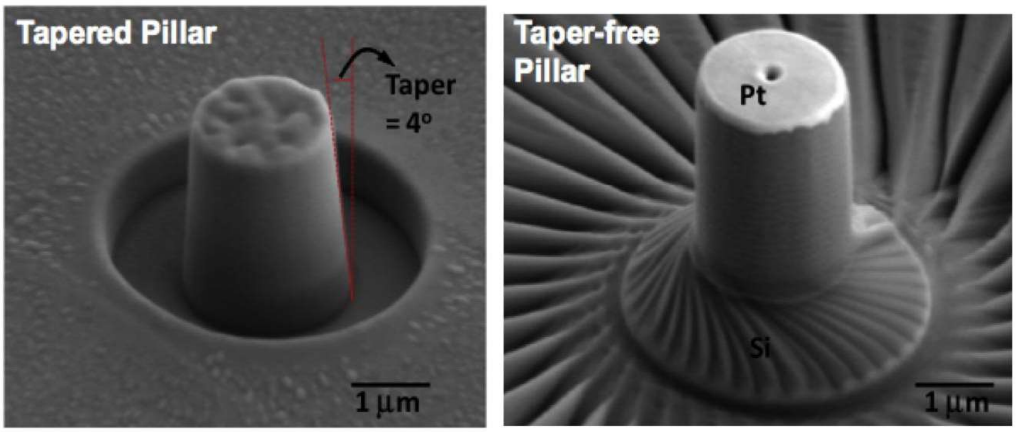

Figure 9: Micropillar fabricated using annular milling, having 4° of taper, and using lathe milling technique. Reprinted from (Singh et al. 2010).

The orientation studies showed that the micropillars having layers oriented in a parallel direction to the loading axis were the strongest followed by the ones oriented perpendicularly and at an 45° angle respectively, shown in Figure 10 (C. R. Mayer et al. 2016). The deformation in the micropillars with the parallel layers was concentrated at the top and was accompanied by buckling and cracking of SiC layers. This was assisted by the waviness present in the microstructure of these materials. Pillars with layers perpendicular to the loading direction had a mushroom type deformation morphology; the SiC layers cracked accompanied by the flow of Al layers. Pillars with layers at 45° orientation with the loading direction had the largest amount of strain-to-failure as the twisting of the deformed SiC layers provided for the damage to be accumulated before complete failure (C. R. Mayer et al. 2016).

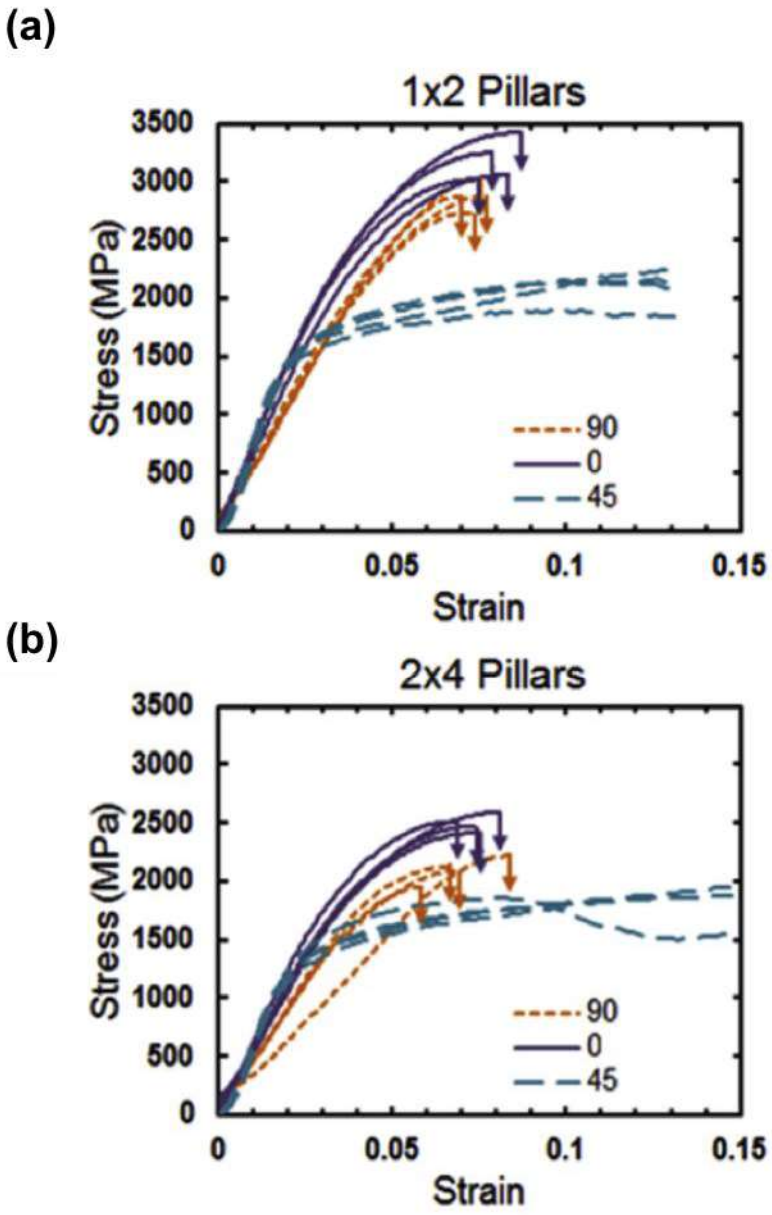

Figure 10: Stress versus Strain curve of (a) 1 x 2 μm and (b) 2 x 4 μm micropillars showing orientation and size effects. Reprinted from (C. R. Mayer et al. 2016).

Size effect was observed in the micropillars made from nanolaminates; however, this was attributed to the presence of initial defects in the micropillar (C. R. Mayer et al. 2016). As discussed above, pores are formed in the microstructure during synthesis due

to geometric shadowing. Weibull analysis was done on the pillars to confirm the role of these defects on the observed size effects. The increase in pillar strength could be compensated by the decrease in volume and hence other mechanisms such as Ga^+ ion beam induced damage was ruled out. Lotfian et al. (Lotfian et al. 2013) showed that the amorphous layer deposited on the sample due to milling from Ga^+ ion beam was just a few nanometers in thickness. This is very small to the overall size of the pillar and thus, expected to have negligible effect on mechanical properties irrespective of the size of the micropillar.

A lot of work has been done on studying the effect of Ga^+ ion induced damage on micropillar compression. One particular study (Bei, Shim, George, et al. 2007) showed that FIB milled pillars have lower yield stress for a Mo alloy in comparison to the pillars prepared via preferential etching of the alloy matrix (Figure 11). The etched pillars yielded close to the theoretical strength and showed no size effects, while FIB-milled pillars had significantly lower yield stresses, which decreased with increasing pillar size (Bei, Shim, George, et al. 2007). Several researchers have focused on studying the effect of FIB induced damage through Laue diffraction analysis prior to the compression of the micropillar (Maaß et al. 2009; Bhowmik et al. 2016; Zimmermann et al. 2010). Ga^+ ion induced damage is of great concern for Al/SiC nanolaminates as it leads to embrittlement in aluminum. This concern has been addressed in this work through quantitative comparison of strength of micropillars fabricated through Ga^+ ion and Ne^+ ion based FIB milling.

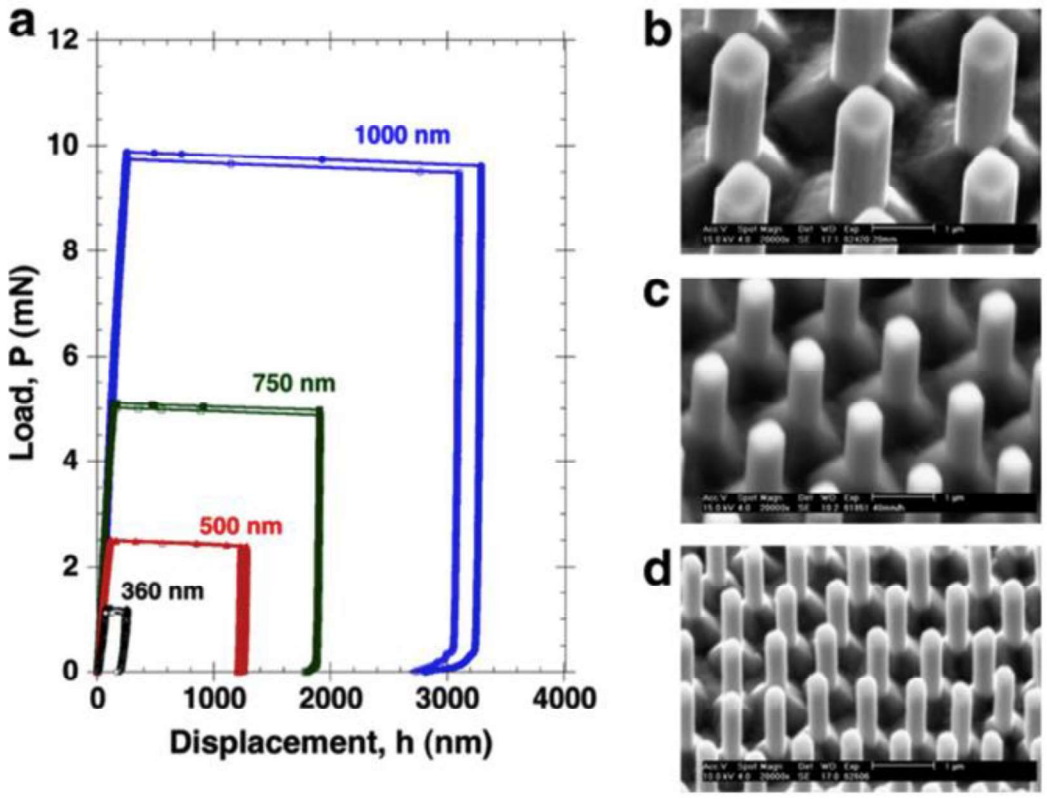

Figure 11: Micropillar compression tests of molybdenum alloy pillars (a) compressive load–displacement curves. SEM images of micropillars with edge dimensions of (b) 750 nm, (c) 500 nm and (d) 360 nm. Reprinted from (Bei, Shim, George, et al. 2007).

The deformation mechanisms operating during micropillar compression was investigated through *in situ* TEM studies as shown in Figure 12. The SiC layers deformed elastically, whereas Al layers deformed plastically under constraint. Grain rotation as well as change in shape of grains was observed. In the absence of any evidence of dislocation pile-up it was speculated that the strain is accommodated through dislocation nucleation and annihilation at the interface.

Further, the effect of layer thickness on rate of strain hardening and compressive

strength of pillars was evaluated. Unlike nanoindentation, a significant effect of layer thickness is observed in micropillar compression (Yang et al. 2018). Under nanoindentation loading, the material is fully constrained and therefore increase in Al yield strength with reduction in layer thickness does not improve the hardness significantly. However, in micropillar compression with the reduction in layer thickness, plastic deformation of Al layers is restricted by the constrained imposed by SiC layers. Therefore, for Al50SiC50 and Al100SiC100 the strain hardening and micropillar strength was low and dependent on Al yield strength. However for Al10SiC10 the increased constraint led to an increase in micropillar strength independent of Al yield strength, as shown in Figure 13.

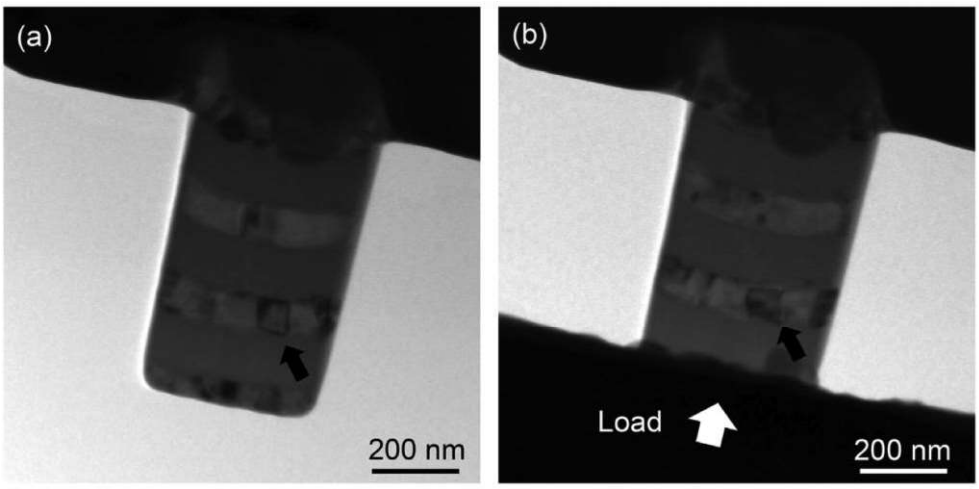

Figure 12: Bright field TEM images of the Al100SiC100 micropillar (a) before the test and (b) after compression of 100 nm. The arrows highlight grain orientation as being one of the deformation mechanisms. Reprinted from (Yang et al. 2018).

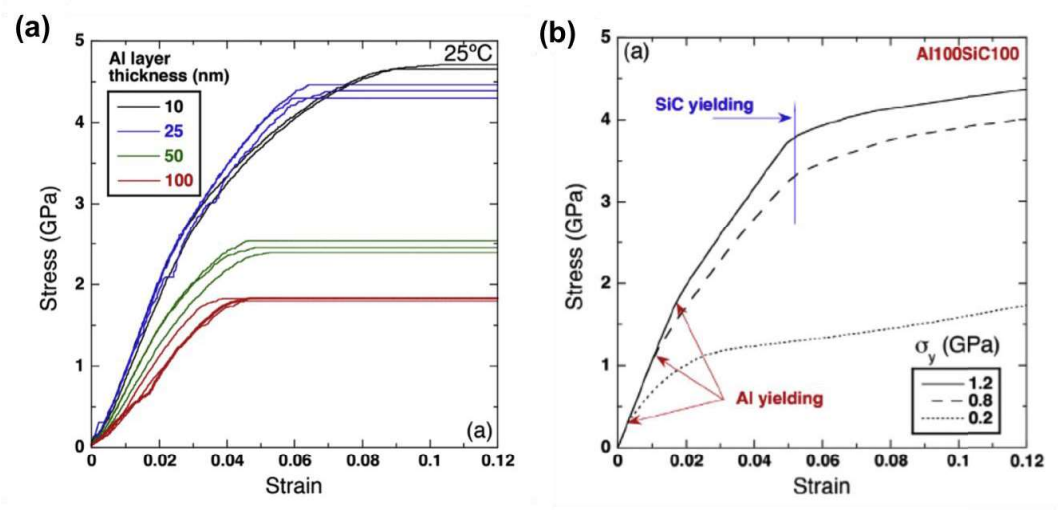

Figure 13: Stress-strain curves obtained by the numerical simulation of the micropillar compression test. (a) Al100SiC100 nanolaminate with different values of the Al yield stress. (b) Idem for the Al10SiC10 nanolaminate. Reprinted from (Yang et al. 2018).

As shown in Figure 14(a), the deformation behavior of these materials has been studied at a temperature of 100 °C. Extrusion of Al out of the pillars was observed at 100 °C, and was much higher than that observed at 23 °C. Moreover, there was a reduction in micropillar strength (Lotfian et al. 2013). It was hypothesized that the flow of the Al layers was facilitated by decrease in Al yield strength and interfacial diffusion, since no dislocations were observed in the Al layers (Lotfian et al. 2013). With a decrease in Al yield strength, the plastic flow of Al becomes relatively easy and therefore a pancake type deformation morphology is seen during high temperature micropillar compression, Figure 14(b).

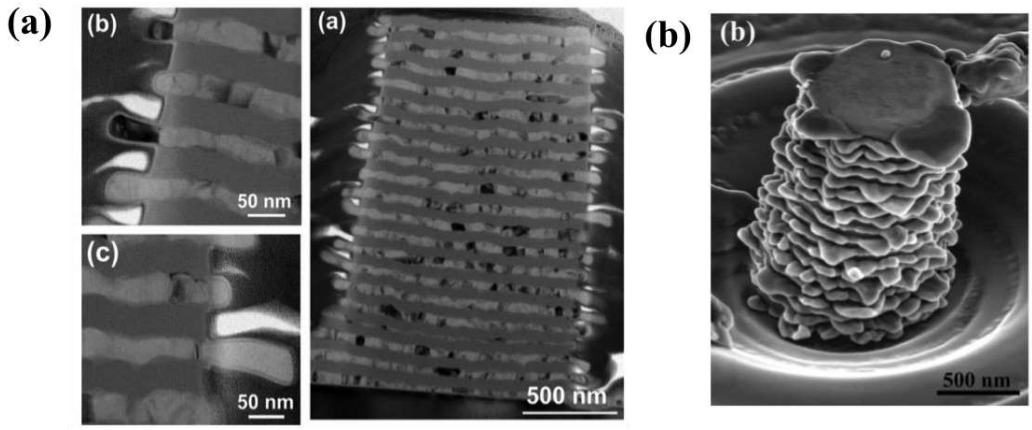

Figure 14 (a) TEM image showing the plastic deformation of Al layer under the constraints from SiC layer. (b) SEM image of the deformed micropillar upto a strain of 8%. Reprinted from (Lotfian et al. 2013).

Fracture toughness of Al/SiC nanolaminates have been evaluated through cantilever beam bending tests and micropillar splitting (Mayer 2016; Yang 2017) . The effect of layer thickness and orientation with respect to the loading direction was studied (Mayer 2016). Just like micropillar compression, significant effect of layer thickness is observed on fracture toughness of nanolaminates. With the increase in number of interfaces the fracture toughness increases because of crack arrest/deflection at the interfaces. This was supported by fracture surface where the cracks followed the columnar boundaries within the layer but followed a tortuous path overall. Interestingly, the tortuous crack path was not observed in Al10SiC10, which also reported lower fracture toughness than Al25SiC25. This trend established the interaction of crack path with the interfaces. For layer thickness above 25 nm, crack deflects at interfaces therefore with more number of interfaces higher energy is dissipated.

2.4. Co-sputtered materials from Magnetron Sputtering

In an attempt to synthesize novel materials with attractive properties, magnetron sputtering has been used for simultaneously sputtering two or more elements often resulting in amorphous microstructures. However, the presence of nanocrystalline aggregates in some of them is what makes them distinct, with novel microstructure. In one such case, the formation of nanocomposite aggregates was reported by Escudeiro et al. (Escudeiro et al. 2015). Characterization done through TEM, X-ray photoelectron spectroscopy (XPS) and X-ray diffraction (XRD) showed that ZrC nanoparticles were formed during synthesis. With the increase of Zr content the columnar boundaries of the coatings were suppressed. It was seen that the hardness was almost independent of Zr content. However, the Young's modulus decreased with the increase of Zr content. The increase in Zr content also led to decrease in residual stress. These mechanical properties were related to the chemical bonding as well as the microstructure of these materials.

Apreutesei et al. (Apreutesei et al. 2014) characterized the nanocrystalline aggregates through HRTEM imaging. As shown in Figure 15(a), HRTEM images were taken and the fast fourier transforms (FFTs) were used to detect the presence of order in amorphous sample. Moreover, a demixion phase was promoted during the nucleation/growth period. Nanoindentation was used to characterize the mechanical properties, and the highest hardness as well as modulus was reported for sample containing 85 at. % of Cu. Differential Scanning Calorimetry (DSC) measurements were done to characterize the thermal properties. A glass transition followed by a super-cooled liquid region and finally crystallization reactions at high temperature were observed from

DSC heating scan of the Zr–Cu thin films.

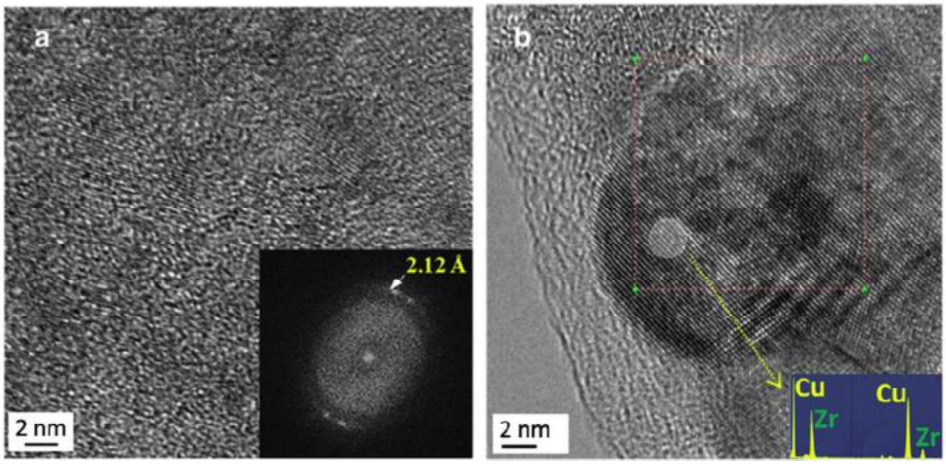

Figure 15: HRTEM plane view micrographs of Zr–Cu thin films. (a) 40.1 at.% Cu with an inserted Fourier transform diffractogram. (b) 59.1 at.% Cu with an inserted EDS spectrum. Reprinted from (Apreutesei et al. 2014).

Through the extensive microstructural characterization of Al/SiC nanolaminates it was established that the mechanical property is dependent on nanocrystalline Al layers, constraint imposed by SiC layers, waviness of layers as well as pores present in the microstructure. Interestingly their individual impact differs with the testing techniques. In nanoindentation when the entire volume is under constraint and the effect of layer thickness on acquired hardness is negligible. Micropillar compression studies showed a flaw dependent fracture mechanism where the shear bands were near the columnar boundary of microstructure. However, in both cases anisotropy with respect to loading direction was observed due to huge mismatch in the elasto-plastic properties of the constituents. To date, the tensile properties of Al/SiC nanolaminates have not been evaluated. Even though micropillar compression studies yield a stress-strain curve, it is

essential to evaluate the tensile strength of nanolaminates to obtain a complete understanding of the mechanical behavior. Similarly, the plastic deformation of Al layer has been studied under extremely constrained environment through nanaoindentation and micropillar compression but no information is available on the mechanical response of nanolaminate in cyclic loading. To that effect, the objectives of this thesis are:

1. Study the evolution of damage and its dependence on the microstructure by performing *in situ* experiments.
    a. *In situ* micropillar compression of Al/SiC nanolaminates for 3D characterization of pores and its effect on the operative damage mechanisms.
    b. *In situ* fatigue experiment to characterize the behavior of nanolayered structures under cyclic loading.
    c. *In situ* tensile testing through MEMS based devices. In tension, the material will be loaded directly in mode I and therefore the behavior is expected to be much more dependent on the flaws, exhibiting significant tension-compression asymmetry.

    Since, most of these samples were fabricated by FIB milling, it is also necessary to study the effect of using Ga^{+} ion based milling on Al/SiC nanolaminate system.
2. Developing new class of materials with superior mechanical properties: the aim is to use the present understanding of structure-property relationships of the nanolaminate materials to develop and characterize new class of materials; co-sputtered Al-SiC composites.

CHAPTER 3

IN SITU MICROPILLAR COMPRESSION OF AL/SIC NANOLAMINATES USING LABORATORY-BASED NANOSCALE X-RAY MICROSCOPE

3.1 Introduction

A complete understanding of the deformation mechanisms occurring in materials is necessary for establishing structure-property relationships as well as designing new generation of novel materials with superior properties. Hence, a lot of importance has been given to expanding characterization capabilities and capturing damage evolution in real time through *in situ* experiments using FIB/SEM (Frei & Grathwohl 1989; Gong & Wilkinson 2009; Moser et al. 2007; Vallabhaneni et al. 2017), TEM (Legros et al. 2008; Mayer et al. 2015) and X-ray tomography (Kaira et al. 2017; Singh et al. 2014; Hruby et al. 2014). Imaging in SEM is restricted to 2D visualization of the sample surface whereas imaging in TEM requires ultra thin, electron transparent samples. On the other hand, X-ray tomography is a technique that allows *in situ* experiments to be performed non-destructively and capture the complete microstructure in 3D. Recently, development of lab-based transmission X-ray microscopes has opened up several avenues for characterizing materials in the comfort of a laboratory (Withers 2007; Merkle & Gelb 2013; Patterson et al. 2016). These setups have been inspired from synchrotron sources and use X-ray optics such as Fresnel zone plates that can achieve a high spatial resolution

of up to 50 nm (Patterson et al. 2016; Withers 2007; Patterson et al. 2014; Taiwo et al. 2016). Achieving such high spatial resolution is crucial for understanding mechanical behavior at the fundamental level as damage originates at the nanoscale before it is accumulated and macroscopic defects are formed. In this regard, a number of attempts have been made to perform *in situ* or interrupted *in situ* nanoindentation, compression, tensile testing using these lab-scale setups (Patterson et al. 2016). However, more complex micromechanical tests such as micropillar compression, microcantilever beam bending tests etc. have yet not been attempted in such setups. This is due to the complex nature of experimental design and execution required for achieving a spatial resolution on the order of tens of nanometers while simultaneously loading the sample. Among these, micropillar compression is one of the best techniques to probe the micromechanical behavior of materials, as it does not involve interpretation of complex stress states from, for example, nanoindentation (Uchic et al. 2004). In this paper, for the very first time, an attempt has been made to perform *in situ* micropillar compression using a lab based X-ray microscope while achieving a spatial resolution of 50 nm.

A micropillar was fabricated on the Al/SiC based nanolaminate system. As discussed earlier, one of the limitations of magnetron sputtering process is the formation of pores in the microstructure. Al forms nanograins that nucleate and grow at different speeds and therefore leads to waviness in the microstructure. This further leads to formation of pores at the troughs of the microstructure as a result of insufficient flux of incoming atoms during sputtering due to geometric shadowing (C. R. Mayer et al. 2016; C. Mayer et al. 2016; Bales 1991). These pores lead to premature buckling of the material

under load, limiting its lifetime as well as toughness (C. R. Mayer et al. 2016). The presence of pores is a ubiquitous problem as magnetron sputtering is now widely used for fabrication of hard, wear-resistant coatings, decorative coatings, transparent conducting oxides, fuel cells etc. (Fortunato et al. 2008; Kelly & Arnell 2000; Ben Amor et al. 1998; Nédélec et al. 2012). Structure zone models were developed explaining the relation between the synthesis parameters such as temperature and pressure with the morphology and distribution of pores (Movchan & Demichishin 1969; Thornton 1974). Nonetheless, a complete visualization and quantification of such defects, which is necessary for a complete understanding of the deformation mechanism, has not yet been done for nanolaminate materials. In the present work, this was achieved through 3D X-ray microscopy on the fabricated micropillar, further the mechanical behavior was characterized through interrupted *in situ* micropillar compression.

However, this micropillar was fabricated from Ga^+ ion source based focused ion beam, which is known to alter the microstructure of materials by causing sample surface amorphization, disclocation loops, interstitial defects, gallium ion implantation etc. (El-Awady et al. 2009; Shim et al. 2009; Bei, Shim, Miller, et al. 2007). Moreover, Al is one of the metals that is known to be embrittled by liquid Ga (Massalski 1990). These defects are believed to play a role in the observed size effects from micropillar compression tests in many materials. The work of Bei et al. (Bei, Shim, George, et al. 2007) showed that FIB milled pillars have lower yield stress for a Mo alloy in comparison to the pillars prepared via preferential etching of the alloy matrix.

Therefore, it was necessary to quantify the effect of Ga^+ ion based micropillar

fabrication on its mechanical response. For this, additionally, a comparative experiment was conducted and micropillars using Ga^+ ion source as well as Ne^+ ion source were fabricated on the same Al/SiC nanolaminate sample. This was possible through alternate routes of FIBs that have been developed using the gas field ion source (GFIS) technology and have incorporated source materials such as neon, argon, and helium ions (Okawa et al. 2011; Suzuki et al. 2012; Böhringer et al. 1988; Elswick et al. 2013; Economou et al. 2012; Urban et al. 2012). In this paper, for the first time, the effect of using Ga^+ ion and Ne^+ ion sources has been compared by measuring the strength of micropillars fabricated from both ion beams.

3.2 Materials and Experimental Procedure

Al/SiC nanolaminates having an individual layer thickness of 100 nm was used for the interrupted *in situ* micropillar compression. A laboratory-based nanoscale XRM (ZEISS Xradia 810 Ultra, Carl Zeiss X-ray Microscopy Inc., CA) was used for collecting 3D data while compression was preformed using a commercial nano-mechanical testing stage (Carl Zeiss X-ray Microscopy Inc., CA). The X-ray microscope was used in its high-resolution mode of imaging wherein the field of view was 16 μm and a spatial resolution of 50 nm was achieved through the Fresnel zone plates, that produces a magnified image of the sample at the detector. The schematic of the setup has been shown in Figure 16. More details about the Xradia 810 Ultra can be found somewhere else (Cordes 2014; Epting et al. 2012; Patterson et al. 2016).

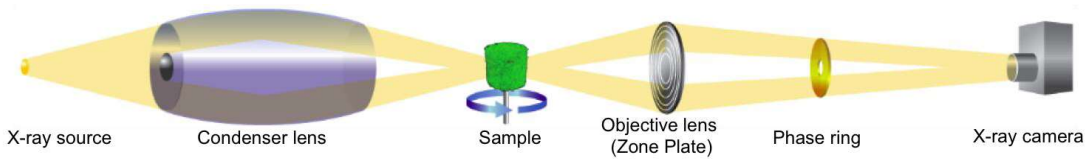

Figure 16: Schematic of the operation of Xradia 810. The beam passes through the following components: capillary condenser, the sample, a Fresnel Zone plate objective lens, a phase ring for Zernike phase contrast, and a lens-coupled CCD detector (Merkle & Gelb 2013).

One of the most challenging aspects of this experiment was placing the fabricated micropillar on the bottom anvil of the load stage, which also serves as the sample-mounting pin, as shown in Figure 17(a) and Figure 17(b).

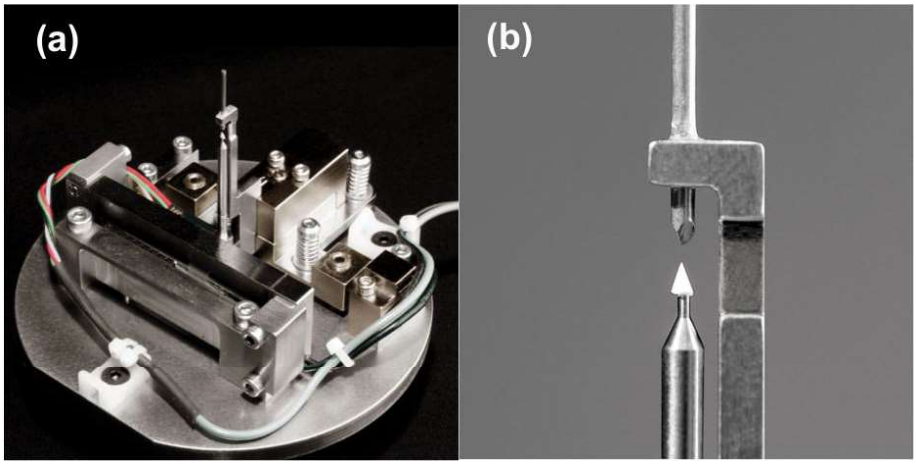

Figure 17: (a) Image of the Ultra Stage (Patterson et al. 2016). (b) magnified image of the anvils used for mounting the sample and loading (Patterson et al. 2016).

To achieve this, a sequence of operations was performed, as shown in Figure 18. Electron beam induced platinum was deposited on the top surface of the sample using a gas injection system for protecting the sample from any possible gallium induced

damage. Micropillar of size 5 x 10 μm was fabricated using a commercial FIB/SEM (Nova 200 NanoLab FEGSEM/FIB, FEI Co, Oregon), an accelerating voltage of 30 kV and beam currents of 16 nA, 1 nA and 120 pA were used. The fabrication was done at the edge of the sample for ease during lift-out, as shown in Figure 18(a). The micropillar was lifted out using an *in situ* nanomanipulator with the stage being at a tilt angle of 52° and then welded on to the sample mounting pin by the use of ion induced platinum deposition. This however, also led to some re-deposition on the pillar surface.

After the setup was ready, alignment was done using the adjustable top anvil of the stage. Tomographic scans were taken in the Zernike Phase Contrast mode at three different loads 0 mN, 12 mN and 35 mN. Each scan comprised of 2D projections taken at 0.25° angular increments from 0° to 180° with an exposure time of 2 secs per projection. The load stage consists of a closed loop position control which ensures that the load is constant as well as the sample and anvil are stable during the course of scan (Patterson et al. 2016). Projection data collected had a ~30 degree missing wedge due to sections of load stage which is not transparent to X-rays. A voxel resolution of 32 nm and a spatial resolution of 50 nm was achieved. Reconstruction of the three acquired datasets was done using a commercial image reconstruction software package (ZEISS XMReconstructor, Carl Zeiss X-ray Microscopy Inc., CA).

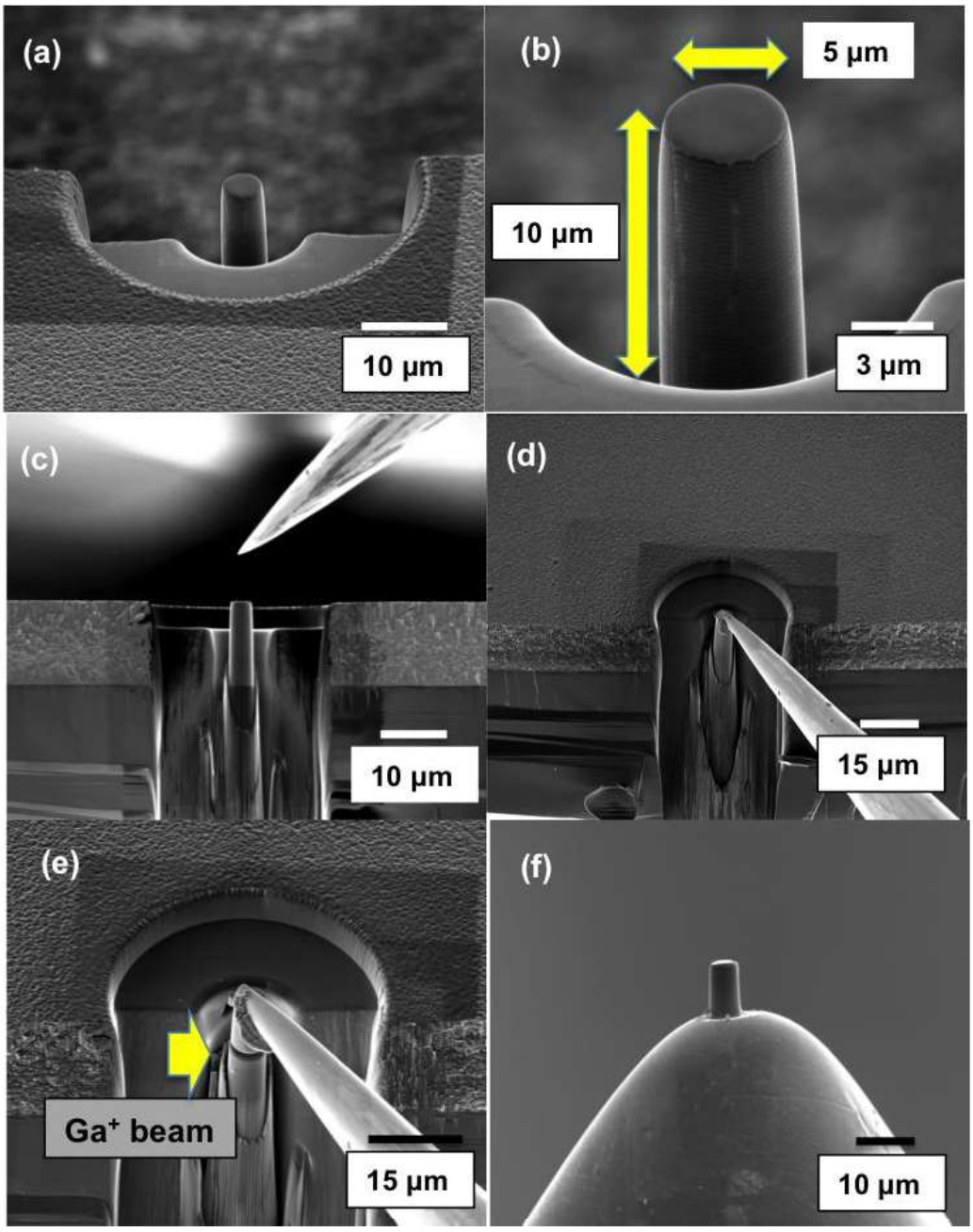

Figure 18: Sequence of steps for sample preparation and placement of micropillar using the omniprobe and ion induced platinum deposition.

For the second experiment, which entailed a comparison between the micropillars fabricated from Ga^+ and Ne^+ ion based beams; Al/SiC nanolaminates having an

individual layer thickness of 50 nm was used. A commercial FIB (Auriga, Carl Zeiss X-ray Microscopy Inc., CA) was used for fabricating pillars using a Ga^+ ion source and a GFIS-based FIB (Orion NanoFab, Carl Zeiss X-ray Microscopy Inc., CA) was used with its Ne^+ ion source. Five pillars were made from each FIB instrument using annular milling. The pillars were 1 x 3 μm in dimension with an approximate taper of 5° as shown in Figure 19.

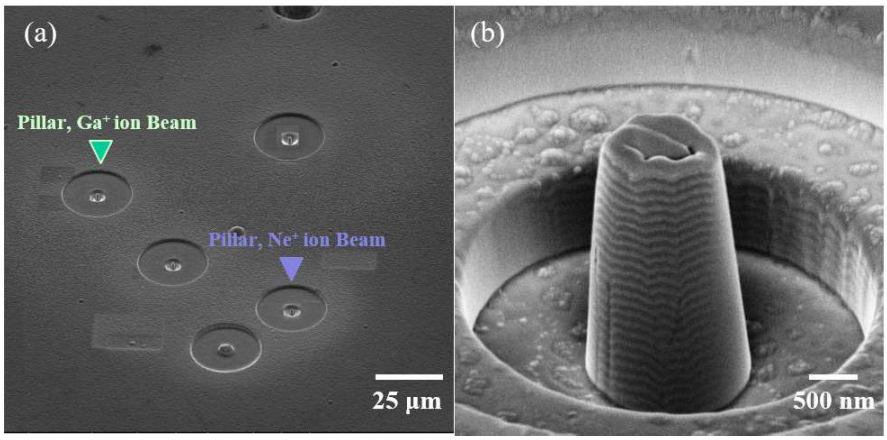

Figure 19: (a) Sample containing micropillars made from Ga^+ ion and Ne^+ ion sources. (b) Micropillar fabricated using Ga^+ ion source.

A 20 μm trench was provided around the pillar as clearance for the indenter flat punch. Since milling with Ne^+ ion beam is very time consuming, the pillars were initially coarse milled (using the Ga^+ ion source) to dimensions of 2 x 2 μm. The final shape was then achieved through milling by Ne^+ ion beam while removing 500 nm thick layer from outside to ensure the removal of any traces or effect of Ga^+ ion on the pillar that may have been present. This was a conservative value as Unocic et al. (Unocic et al. 2010) showed that removal of 350 nm thick layer is sufficient for eradication of penetrated Ga.

For pillars made using Ga^+ ions, 30 kV ion beam accelerating voltage and beam currents of 8 nA, 1 nA and 120 pA were used for reaching the depths of 1 μm, 2 μm and 3 μm, respectively. Final polishing was done using a beam current of 50 pA. In previous work, it has been shown that the stress-strain behavior of Al/SiC nanolaminate micropillar is dependent on the degree of taper (Singh et al. 2010). Therefore, these beam currents as well as milling times were chosen to ensure that the pillars fabricated from both ion beams had similar size and taper. Additionally, it is also known that a smaller pillar will have higher fraction of volume that is damaged by fabrication and thereby a more pronounced effect on mechanical properties. Therefore, micropillar size of 1 x 3 μm was ideal for conducting this experiment.

Samples were mounted on an Al stub using a thermoplastic adhesive for pillar compression. A commercial nanoindenter (MTS XP, Agilent Technologies, AZ) was used for conducting these tests. Micropillar compression was conducted using a diamond flat punch with a square cross-section of 10 x 10 μm. The experiments were performed at a displacement rate of 7 nm/s. Therefore, a constant strain rate of 2.5 x 10^{-3} s^{-1} was maintained for all the samples. Thermal drift rate for all the tests was held below 0.05 nm/s.

3.3 Results and Discussion

The pores present in the microstructure were captured and could be seen in the reconstructed dataset of the scan conducted prior to loading, as shown in Figure 20. These pores were formed during the synthesis of Al/SiC nanolaminates due to geometric

shadowing during sputtering, as discussed earlier.

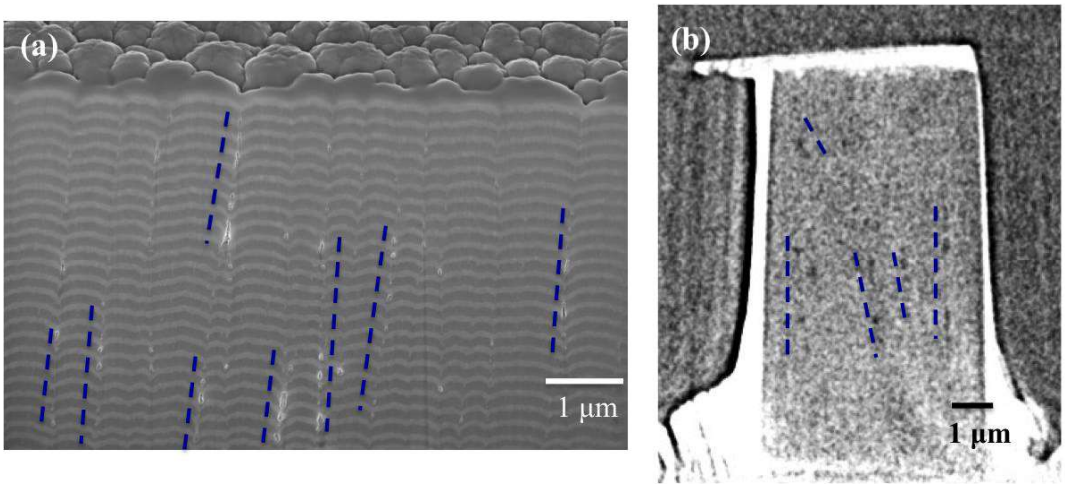

Figure 20: (a) FIB cross-section image showing pores in Al/SiC nanolaminate having layer thickness of 100 nm (b) a 2D slice from reconstructed tomography dataset of micropillar, similar pattern of pores was observed.

It is important to compare the image from 2D FIB cross-section with the tomographic scan. Through FIB cross-section a correlation between the waviness of layers and channel of pores can be seen. As shown through blue arrows, the pores are present along the columnar boundaries of layers. From the reconstructed tomographic scan, similar channel of pores can be seen but they cannot be related with layers, as the layers could not be resolved.

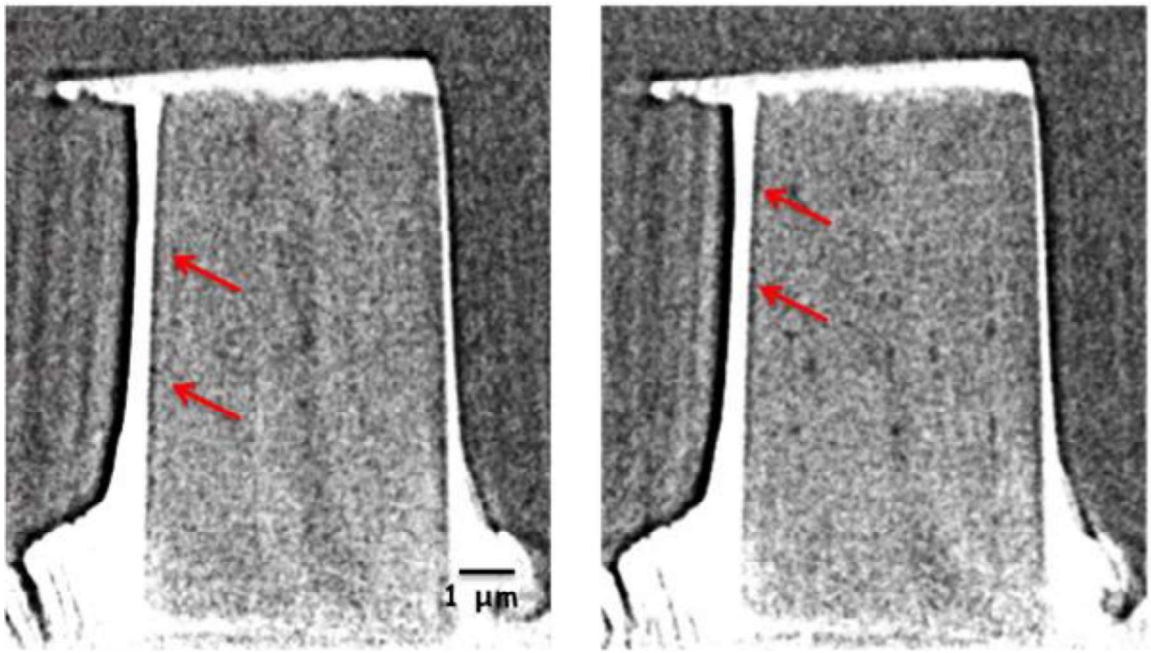

Figure 21: Two different 2D images obtained from the tomography dataset. It is difficult to segment the pores at the edges accurately due to the phase contrast at the sample - air boundary.

The pores at the boundary were not segmented as shown by the red arrows, Figure 22. At the boundary it was difficult to distinguish between the contrast difference that arose due to presence of pores with that of boundary and the air. Moreover, the volume of the pillar was sufficient to be representative of the bulk sample even after the region around the edges was removed. Owing to the presence of noise in the data, segmentation of the pores was done manually through thresholding in image analysis software (ImageJ, Bethesda, MD). Care was taken by moving back and forth through the 2D slices in the dataset to ensure that the segmented area is a pore. Pores grow/reduce in size in the 2D slices that encompass their volume. However, noise if present will not change shape, size and will abruptly vanish. A representative slice showing the segmented binary image

obtained from the 2D tomographic slice has been shown in Figure 22.

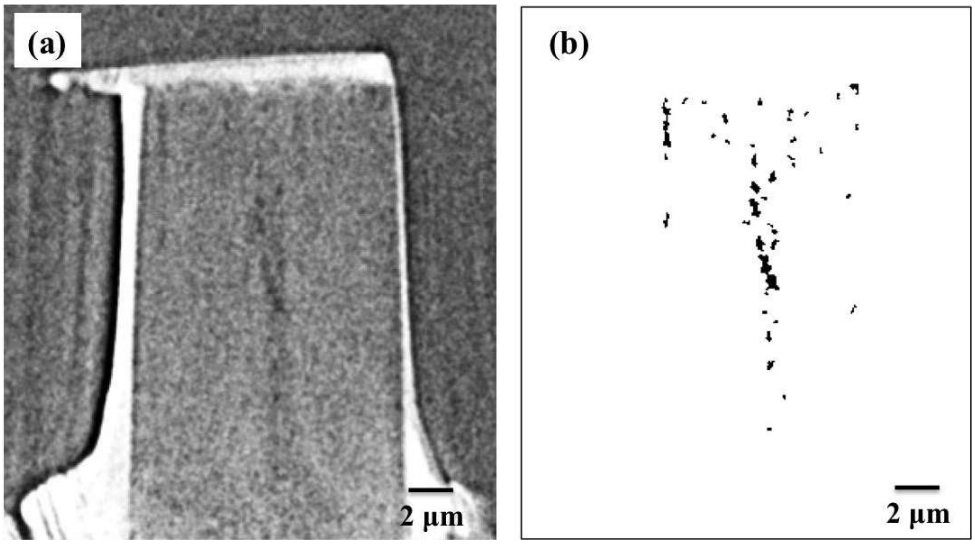

Figure 22: (a) 2D image obtained from the tomography dataset. (b) 2D slice of segmented image obtained using ImageJ software.

As shown in Figure 23, a total of 814 pores were segmented that occupied 0.40% of the total volume under consideration. Avizo® Fire (VSG, Burlington, MA) was used for 3D visualization and quantification of pores. The pores were categorized into small, medium and large size depending on their volume. The small pores had volume lesser than or equal to 0.0016 μm^3, medium pores had volume greater than 0.0016 μm^3 but lesser than or equal to 0.0032 μm^3 and large pores had volume greater than 0.0032 μm^3. The aspect ratio of these pores is seen to vary with volume, small pores had an aspect ratio of 0.50 ± 0.12, medium pores had an aspect ratio of 0.48 ± 0.10 and large pores had an aspect ratio of 0.38 ± 0.09.The larger pores were seen to be longer which is a characteristic of pores formed as a result of geometric shadowing during synthesis (Bales 1991).

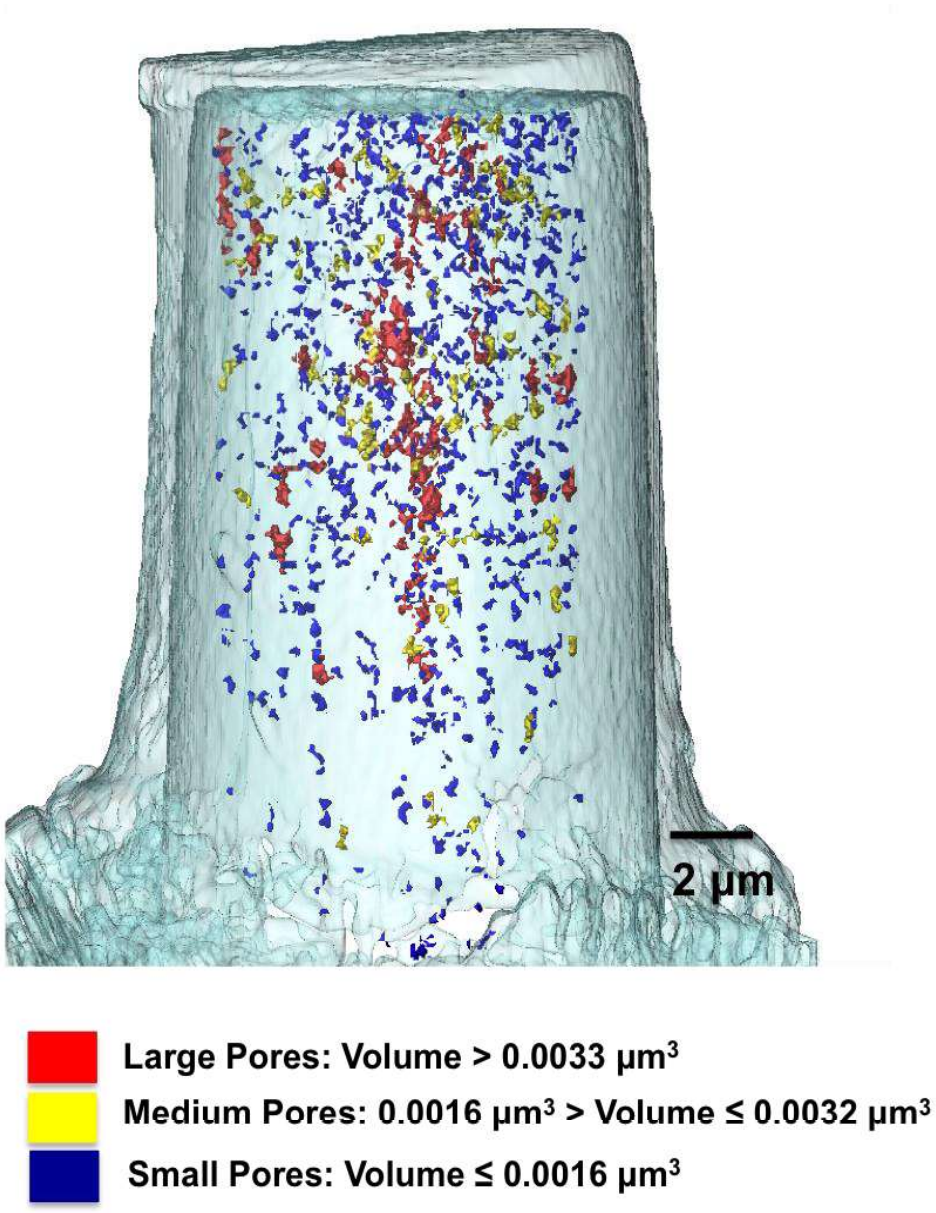

Figure 23: 3D rendering of the pores present in the micropillar generated using Avizo®.

Moreover, a decrease in the density of pores was seen as a function of pillar height, pores occupied 0.70% of the total volume of the pillar in the top half region and only 0.18% of the total volume of the pillar at the bottom region. This is also a characteristic of the shadowing effect during synthesis, where the waviness of the

microstructure gets more pronounced with the deposition of each layer therefore, pores are more likely to be formed in regions away from the substrate than closer to the substrate.

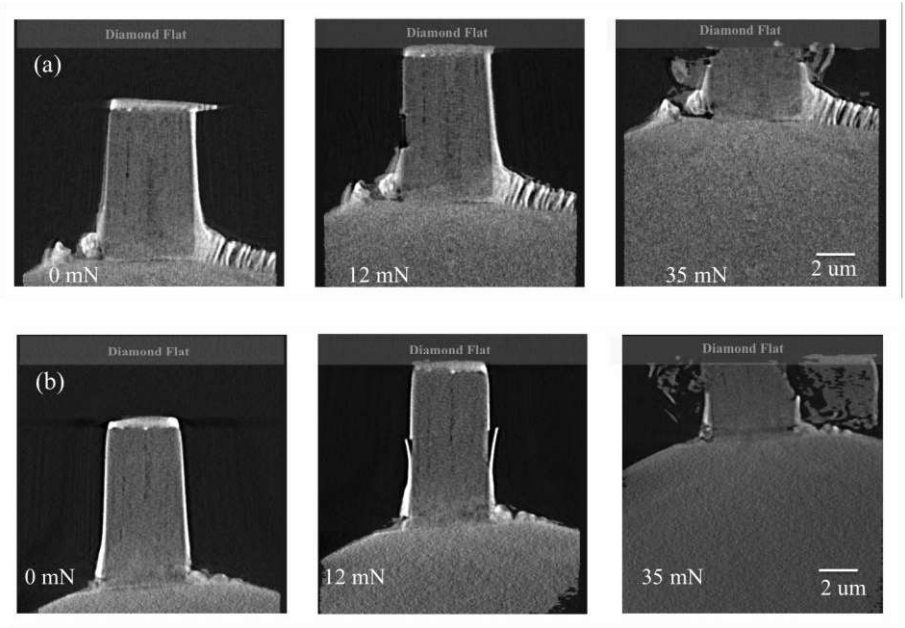

Figure 24: Deformation of pillar captured *in situ* in (a) XZ direction (b) YZ direction

2D slices from the interrupted loading during micropillar compression have been shown in Figure 24. XZ and YZ view of the middle section of the micropillar has been shown. Through these images, it was clear that visible deformation in the micropillar could be observed at a load of 12 mN. The buckling of redopisted layer was observed in the YZ view and evidence of formation of shear bands was also present. However, these images alone did not provide sufficient information about sites of crack initiation and its correlation with the microstructure.

A lot of information was gathered about the deformation mechanism through 3D

reconstruction of the boundary of micropillar and its correlation with the 2D slices from the tomography dataset. Through earlier work, which relied only on post-deformation analysis, it was deduced that these pillars deformed through cracking of SiC layers and plastic flow of Aluminum leading to a mushroom type deformation morphology (C. R. Mayer et al. 2016; Singh et al. 2010; Lotfian et al. 2013). However, through this study, the damage initiation in the micropillar was correlated with the presence of specific microstructural features. Pores were seen forming channels, running through the edge of micropillar to the center (Figure 25(a)). The presence of pores, in that direction, as marked in the figure, facilitated shearing along this plane under a load of 12 mN. This was evident from the formation of shear band seen from the 3D rendering of the boundary of the micropillar, indicating shearing as being another operational damage mechanism (Figure 25(b)). As shown in this figure, this also led to delamination, the re-deposited layer at the pillar boundary is seen to be peeled off at the intersection of the shear band with the surface. This 3D shearing observation is in line with previous studies where shear and kink bands were formed along the troughs of the wavy microstructure and not along the stronger Al/SiC interface (C. R. Mayer et al. 2016). Ultimately, shearing led to the fracture of micropillar, at a load of 35 mN, as shown in Figure 25(c).

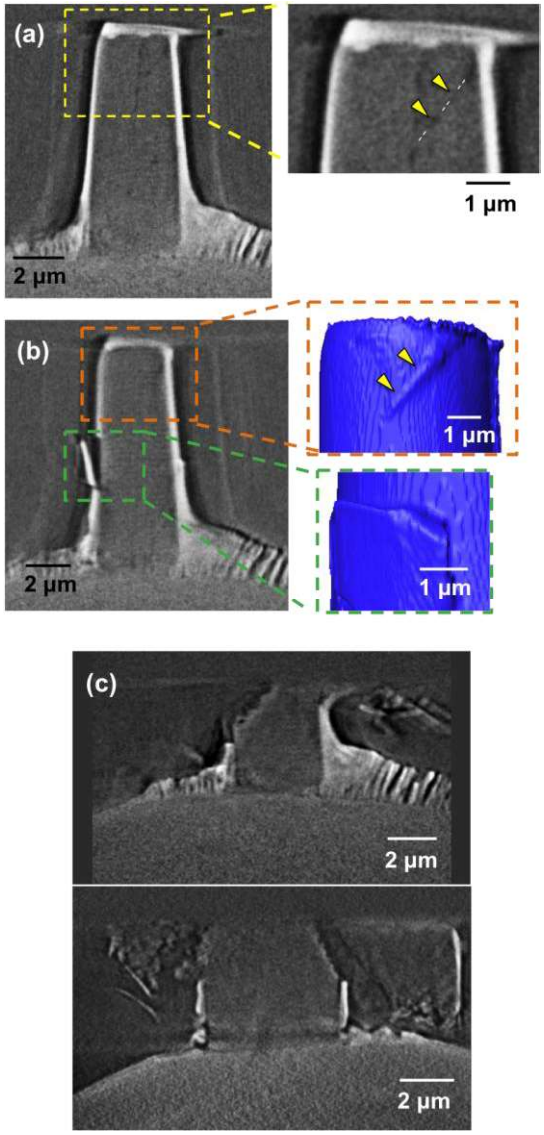

Figure 25: 2D slice of the reconstructed dataset acquired at (a) zero load in XZ plane, pores form a channel from the edge to the center of micropillar. (b) 2D slice at a load of 12 mN in XZ plane, shearing occurs along the plane and leads to delamination at the surface as seen from the 3D reconstruction of the boundary at the regions of interest (c) at a load of 35 mN in XZ plane (top) and YZ plane (bottom) leading to complete fracture of the micropillar.

From the stress-strain curve it is clear that the micropillar failed in a brittle manner (Figure 26). Nanolaminate metal-ceramic systems are expected to exhibit some degree of toughness due to crack blunting in the ductile metallic layers and crack deflection at the interfaces. In the fabricated micropillar, the Al layers were ~100 nm thick and it had ~100 interfaces, however, there were no signs of plasticity. This was due to the presence of pores in the microstructure, which formed channels that acted as sites of damage initiation and propagation, leading to limited plasticity. Therefore, the information acquired at the beginning of test, the size and distribution of pores, was used to understand the evolution of damage in the Al/SiC nanolaminate micropillar.

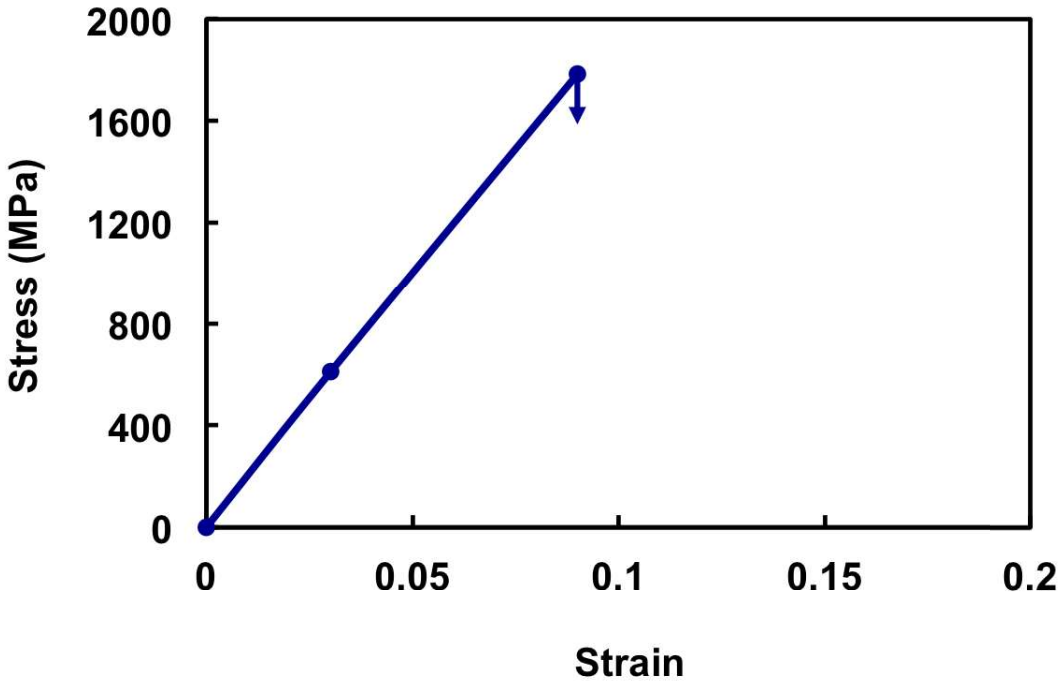

Figure 26: Representative stress-strain curve from interrupted *in situ* micropillar compression. The micropillar fractured without any signs of plastic behavior.

The engineering stress-strain curves from the compression of micropillars fabricated using Ga^+ and Ne^+ ion sources are shown in Figure 27. It can be seen that the initial behavior was much more compliant than that expected from purely elastic loading. This arises from slight misalignments between the micropillar surface and the flat punch leading to local plastic yielding at the top surface of the micropillar until full contact is established. The arrows on the curves indicate the strain-to-failure for each pillar. From the figure, it is clear that the fracture strength of each pillar is independent of the ion source used for pillar fabrication. The average fracture strength of pillars fabricated using the Ne^+ ion beam is 3018 ± 199 MPa, whereas for those using the Ga^+ ion beam is 3074 ± 121 MPa, having a difference of 5MPa, which is in the range of error. The strain-to-failure of all the pillars is also fairly similar and lies in the region of 5.2% to 6.4%.

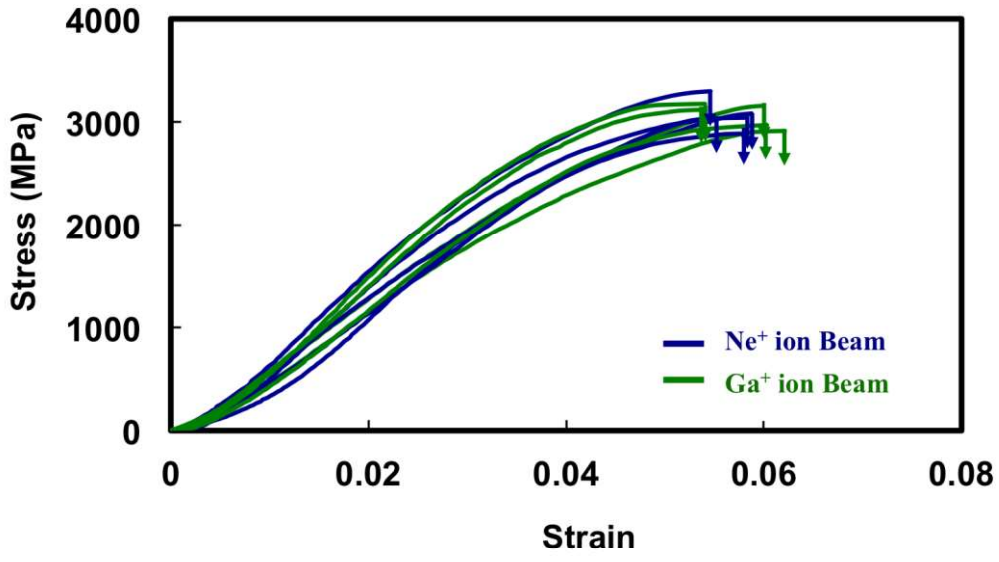

Figure 27: Engineering stress - strain curves from micropillar compression. Micropillars

made from Ga^+ and Ne^+ ions had the same strength and strain-to-failure.

From Figure 28, it can be seen that the pillars deformed having a mushroom type deformation morphology. This is due to the large strength difference and increasing incompatibility as a function of stress between the individual Al and SiC layers. At the top of the micropillar, cracking of SiC layers and plastic flow of Al layers within the crack was observed. This observed cracking of SiC layers indicates a direct dependence of failure on the initial distribution of flaws in the micropillar (C. R. Mayer et al. 2016). Since the micropillars were made in close proximity on the same sample and had the same size, they are expected to have a similar distribution of flaws and in this respect, similar stress-strain behavior.

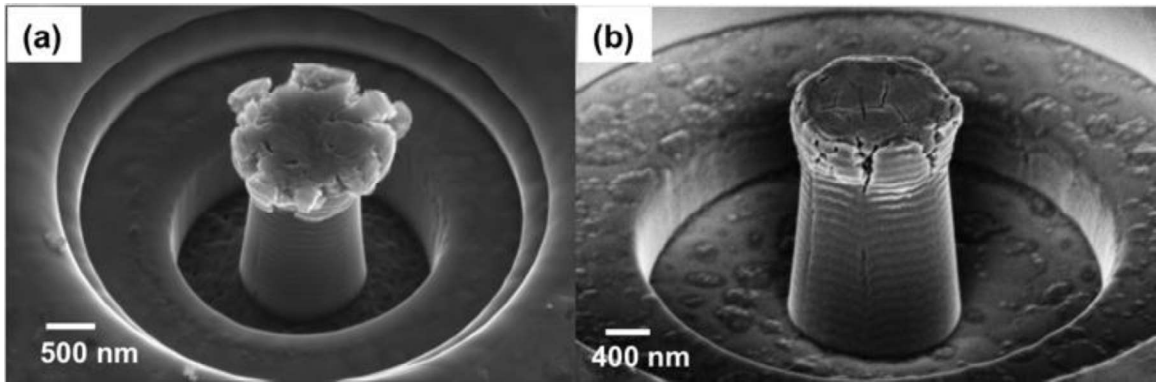

Figure 28: SEM image of micropillars after deformation. Micropillar made from (a) Ne^+ ion beam and (b) Ga^+ ion beam. Micropillars have a mushroom type morphology indicating the same operative deformation mechanism in both cases.

Differences arising from other possibilities can also be eliminated, it has been previously shown that the irradiation of the Al/SiC nanolaminates with Ga^+ ions does not

produce any dislocation loops (Lotfian et al. 2013). Moreover, the embrittlement of the Al phase due to diffusion of Ga^+ ions can be ruled out as the micropillars made from the Ga^+ ion beam showed the same plasticity to the ones fabricated from the Ne^+ ion beam. This was also supported by the deformation behavior of these nanolaminates that showed no evidence of the brittle intergranular fracture, confirming no signs of embrittlement. The possibility of embrittlement has also been rejected in a previous work on the micropillar compression behavior of Al/SiC nanolaminates (C. R. Mayer et al. 2016). This can be attributed to the microstructure of the nanolaminates, wherein the nanocrystalline Al grains have a width of approximately 60 nm, equivalent to the layer thickness and thus, there are limited boundaries exposed during milling.

Another factor that can play a role in altering the stress-strain behavior is sample surface amorphization. However, TEM studies on nanolaminates have shown that the layer deposited on the micropillar surface due to amorphization from Ga^+ ions is as thin as 5 nm on Al layer and 3 nm on SiC layer (Mayer et al. 2015). This is negligible compared to the size of pillar diameter and therefore is not expected to alter the flow stress of pillars fabricated from Ga^+ ion.

It is also essential to discuss the validity of these results for different sizes of micropillars. A smaller pillar is expected to have a more pronounced effect of Ga^+ ion induced damage on mechanical properties. Therefore, micropillar size of 1 x 3 μm was ideal for conducting this experiment as any changes, if present, would be the most for this case.

On comparing the results, these values of fracture strength and strain-to-failure

are different from the 5 x 10 μm micropillar. The decrease in strength arises from the change in individual layer thickness as well as change in size of the micropillar. The pillars are expected to show size effects arising due to change in the initial distribution of flaws with the change in the size of micropillars. Therefore, the increase in pillar strength observed with reduction of pillar size is due to lower probability of strength limiting flaw in small pillars (C. R. Mayer et al. 2016). Thus, in case of Al/SiC nanolaminates, the effect of Ga^+ ion induced damage on the microstructure can be ignored while interpreting the results from micropillar compression as well as other microscale testing samples.

3.4 Summary

Pores are formed in the Al/SiC nanolaminates during the synthesis process and play a very important role in determining the mechanical behavior. 3D X-ray microscopy was used to characterize the pores and obtain a complete understanding of their size and distribution. The damage evolution was captured through the interrupted *in situ* compression testing and was successfully correlated with the microstructure. Shearing was identified as another operational damage mechanism in addition to SiC layer cracking and plastic flow of Al. The effect of Ga^+ ion beam milling on the micropillar fabrication process was also evaluated. It was seen that the mechanical properties of the pillars made from Ga^+ ion beam were very similar to the ones fabricated using the Ne^+ ion source. It can also be concluded that sputtering of the nanolaminate sample surface with Ga^+ ions did not lead to any significant microstructural damage capable of bringing about a change in its mechanical properties.

CHAPTER 4

TENSILE BEHAVIOR OF AL/SIC NANOLAMINATES

4.1 Introduction

The mechanical properties of Al/SiC nanolaminates have been well established through nanoindentation and micropillar compression studies (Yang et al. 2018; Mayer et al. 2015; Lotfian et al. 2014; Singh et al. 2010; Lotfian et al. 2013; C. R. Mayer et al. 2016). They are reported to have a modulus of ~ 100 GPa and hardness ranging from 4-10 GPa (Yang et al. 2016; C. Mayer et al. 2016). The hardness of these nanolaminates increased with a decrease in Al volume fraction, as SiC is stiffer than metallic Al (Yang et al. 2016). A similar increase was observed with a reduction in Al layer thickness as the Al grain size decreases and hence the yield strength increases (Yang et al. 2016). Moreover, it was demonstrated that the strain hardening of metal-ceramic nanolaminates was due to a buildup of hydrostatic stresses from the elastic constraint imposed by the ceramic layers on to the plastic flow of metallic layers (Lotfian et al. 2013). This phenomenon was contrary to the increase being expected due to the multiplication of dislocations in the metallic layers. Further, the interface of Al/SiC nanolaminates is reportedly strong since voids are formed in the Al layer during nanoindentation and not at the interface (Yang et al. 2016). Even for the high temperature micropillar compression studies, the interface remained intact and devoid of reaction products (Lotfian et al. 2013; Yang et al. 2018). Another characteristic feature that governs the mechanical behavior of these nanolaminates are the pores present in their microstructure. Pores are formed due to columnar growth during deposition of these layers (C. R. Mayer et al. 2016). Shear bands

are formed along the columnar boundaries during micropillar compression leading to its premature failure (C. R. Mayer et al. 2016). These defects are also responsible for the observed size effects during micropillar compression, where the increase in strength of 1 x 2 μm pillars in comparison to 2 x 4 μm pillars could be completely accounted by a decrease in the volume term through Weibull statistics (C. R. Mayer et al. 2016). These studies indicate a flaw dependent fracture in Al/SiC nanolaminates, and such flaws are expected to give rise to significant tension-compression asymmetry in mechanical behavior. Therefore, it is essential to investigate the tensile properties of Al/SiC nanolaminates to obtain a complete understanding of their deformation behavior. Moreover, even though, micropillar compression provides an actual stress-strain curve, the compressive stresses can prevent crack propagation especially in brittle materials.

To the best of author's knowledge tensile behavior of metal/ceramic nanolaminates has not yet been studied through microtensile testing techniques and limited work has been done on metal/metal and metal/metallic glass nanolaminates (Hemker & Sharpe 2007; Anderson et al. 1999; Nieh & Wadsworth 2008; Nizolek et al. 2016; Kim et al. 2011). Moreover, none of the studies present an exhaustive report describing the effects of layer thickness and microstructural defects on tensile properties of nanolaminates, which play a key role in determining their deformation behavior. In this work, *in situ* microtensile tests are performed through micro-electro-mechanical systems (MEMS). As discussed above, pores are present in the nanolaminates owing to geometric shadowing from the wavy microstructure. The columnar growth of nanocrystalline Al leads to grains having different dimensions and with the deposition of

each layer, these differences get amplified and lead to the formation of crests and troughs in the microstructure. Therefore, for a given sample, the microstructure varies as a function of distance from the substrate. The layers close to the substrate are not wavy and are devoid of pores, and hence are expected to have a very different response to the applied load. To study this behavior, nanolaminate samples having total thickness of just 1 μm were deposited on the Si substrate. Two sets of samples, having individual layer thickness Al 25 nm/SiC 25 nm containing 20 bilayers and Al 100 nm/SiC 100 nm containing 5 bilayers were used. This is another avenue that has not been explored for nanolaminates and most of the studies have concentrated on mechanical properties of FIB milled structures, which are typically away from the Si substrate.

4.2. Materials and Experimental Procedure

4.2.1 Synthesis of Nanolaminates

Al–SiC nanolaminates for fabricating dog-bone samples were synthesized using magnetron sputtering on a Si (100) substrate. The targets used were pure Al (99.99%) and SiC (99.5%) (Kurt J. Lesker, Clarion, PA). Deposition was carried out at target power of 95 W and 215 W for Al and SiC respectively to achieve a deposition rate of 7.5 nm/min. The Al and SiC targets were used alternatively until the total multilayer thickness was approximately 1 μm. The nominal volume fraction was ~ 0.5 and samples having individual layer thicknesses of 25 and 100 nm were synthesized.

4.2.2 MEMS based tensile tests

The dog-bone shaped freestanding films for tensile testing were co-fabricated with the MEMS stage. Photoresist was spin coated on the front and back of the sample. Patterning was performed on the photoresist using photolithography. The nanolaminate sample was patterned through wet etching. Subsequently, the photoresist was removed from the front of the sample and the Si substrate was etched from the back to obtain a freestanding nanolaminate film. The dog-bone samples were ~ 1 x 75 x 300 μm in dimension. The sequence of steps has been shown schematically in *Figure 29*.

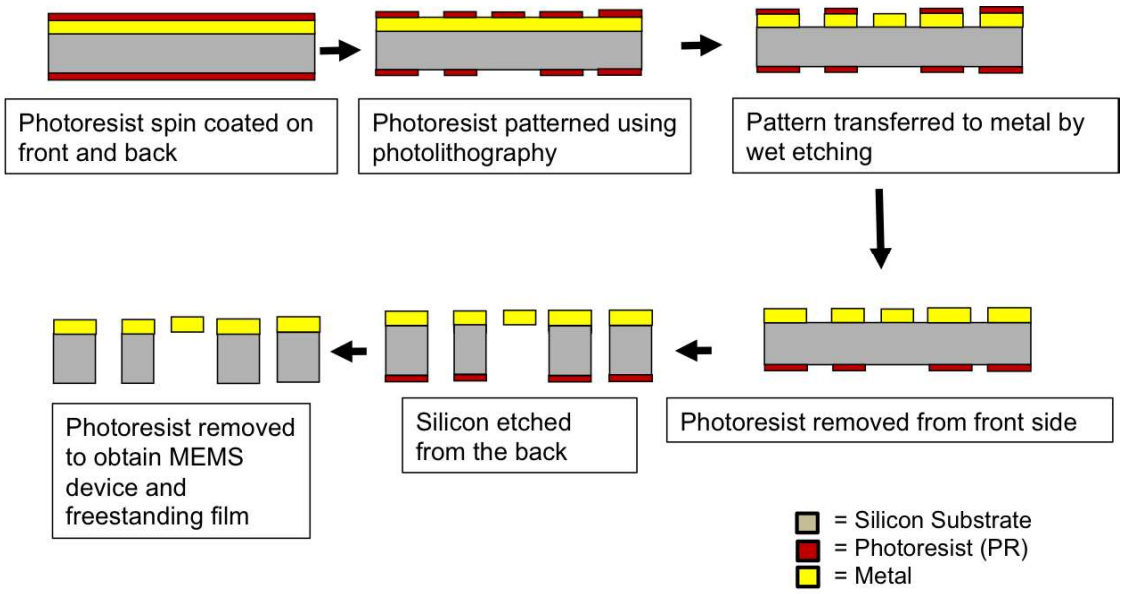

Figure 29: Schematic illustrating the steps for fabrication of MEMS devices.

For tensile testing, the stage was pulled from one end by a piezoelectric actuator (Physik Instrumente), keeping the other end fixed, to apply deformation on the sample. The U-beams and alignment beams ensured the application of uniaxial stress on the freestanding nanolaminate film. Schematic of MEMS device containing the dog-bone nanolaminate

sample is provided in Figure 30(a). The total force (F_{tot}) on the device was measured by a load cell. Force on the sample is dependent on the force on the alignment beams (F_A) and U-beams (F_U), as shown in Figure 30(b). Therefore, their combined stiffness was obtained through another experiment and multiplied with the total deflection, "x", to calculate $F_A + F_U$. This value was subtracted from the total force on the sample to calculate F_s. The strain in the sample was calculated by measuring the relative displacement of gauges G1 and G2 using the cross-correlation technique through a custom MATLAB™ script.

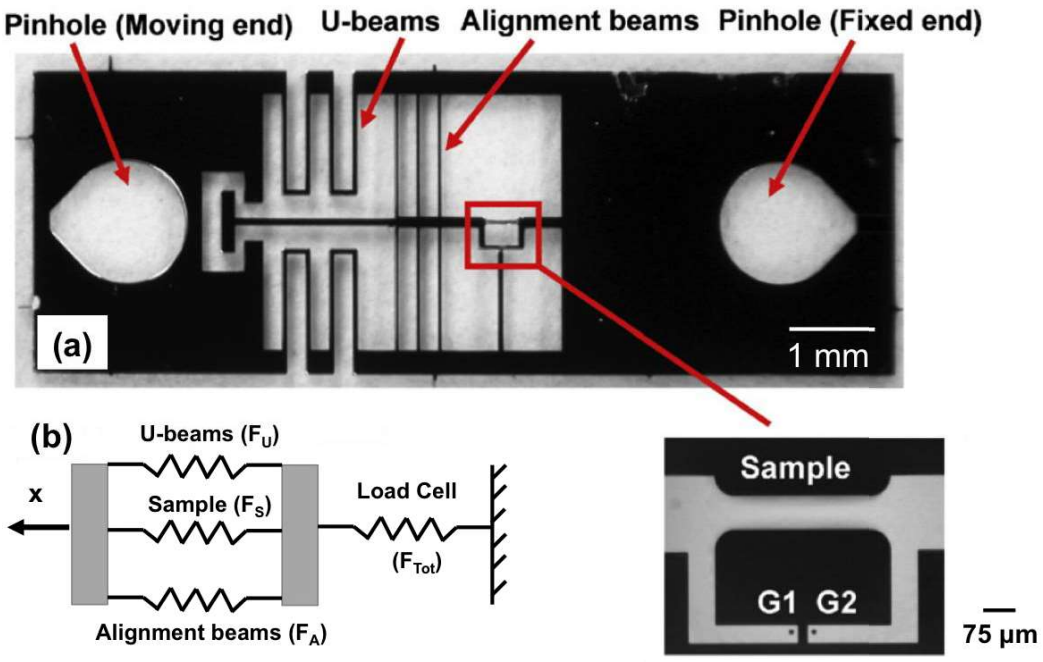

Figure 30: Schematic showing the (a) co-fabricated dog-bone sample with MEMS stage, (b) loading configuration between the sample, U-beams and alignment beams.

4.2.3 Nanoindentaion

Young's modulus and hardness of Al/SiC nanolaminate samples hve been studied in great detail (Lotfian et al. 2014; C. Mayer et al. 2016; Yang et al. 2016; Yang et al. 2018). However, these samples, depending on their individual layer thicknesses, contained more than 100 bilayers and hence a wavy microstructure. In the present scenario, micromechanical properties of the nanolaminate samples having a total thickness of 1 μm were analyzed by nanoindentation tests using a commercial nanoindenter (MTS XP, Agilent Technologies, AZ). This was essential to validate the hypothesis that the microstructure in a typical nanolaminate sample varies with distance from the substrate and therefore is expected to have a difference in mechanical properties. Samples were mounted on an Al stub using a crystal bond and indentation was carried out on 20 different locations in the sample. The measurements were performed using a continuous stiffness measurement technique (CSM) by superimposing a small harmonic load (Li & Bhushan 2002a). Before indenting the specimens, the calibration of nanoindenter was done by measuring the Young's modulus and hardness of a standard silica sample.

4.3. Results and Discussion

The microstructure of Al100SiC100 nanolaminate sample having a total thickness of ~ 15 μm has been shown in Figure 31. The presence of columnar boundaries with channel of pores can be observed in the microstructure. These pores are expected to play a role in the deformation behavior during tensile testing as discussed ahead.

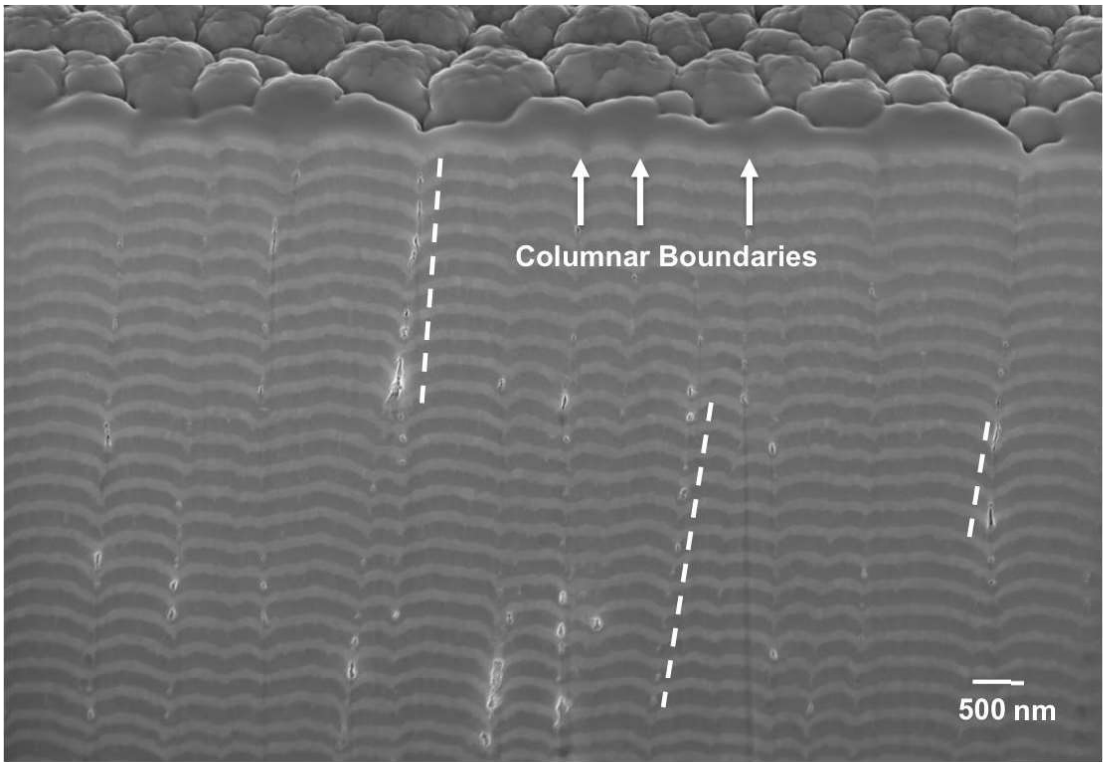

Figure 31: FIB cross-section of Al100/SiC100 nanolaminate showing the presence of columnar boundaries and pores in the microstructure.

Images acquired during the test have been shown in Figure 32 for Al25SiC25 sample. The top surface of the sample along with gauges G1 and G2 have been captured. The fracture surfaces are not mating as the release in elastic energy from the first fracture leads to a subsequent fracture instantly. The failure was sudden and could not be captured during the test. The top surface of the sample does not show any signs of deformation until the complete failure. With an increase in load, the sample is strained and this can be observed from the increase in gap between G1 and G2, which was used to calculate the strain on the sample.

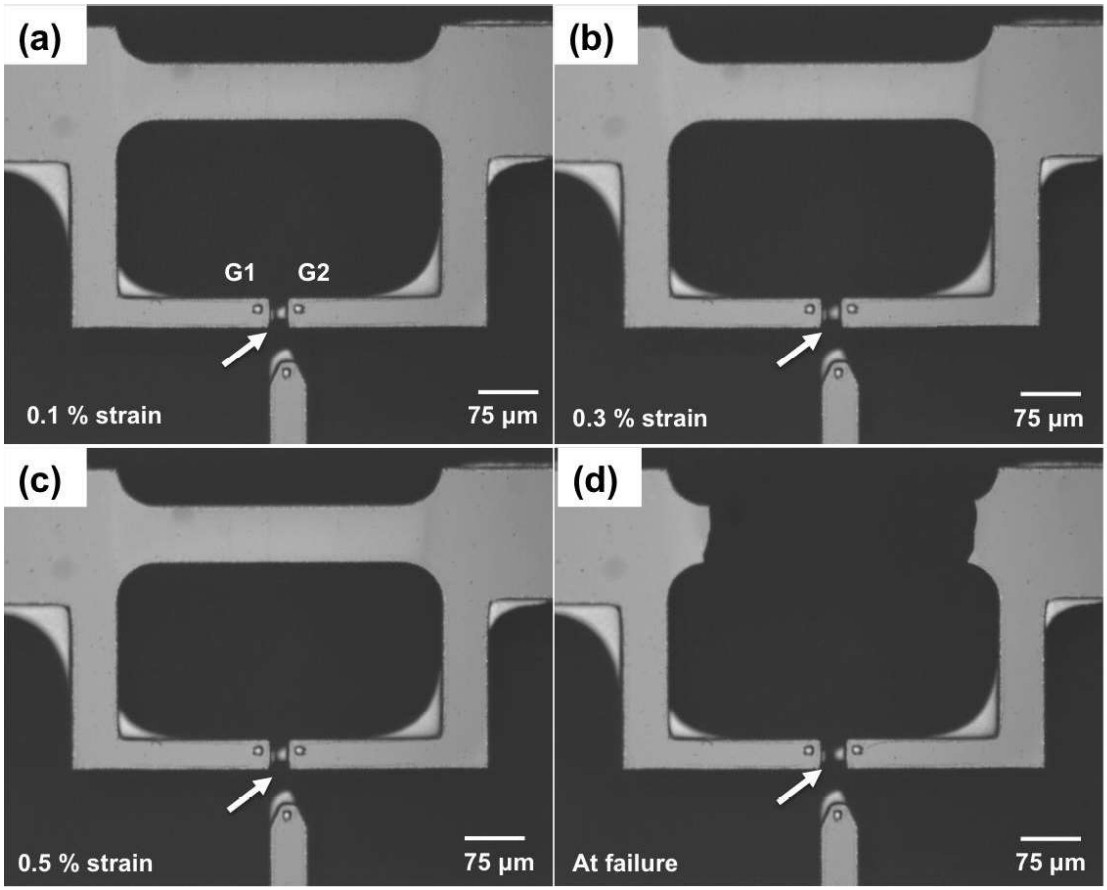

Figure 32: Images acquired during the quasistatic loading of Al25SiC25 sample. The top surface of the sample does not indicate any damage until failure. The relative positions of G1 and G2 were used to calculate the strain.

The stress-strain curves for the MEMS based tensile tests of Al100SiC100 and Al25SiC25 are shown in Figure 33. The samples were loaded only in the direction parallel to the layers (0°).

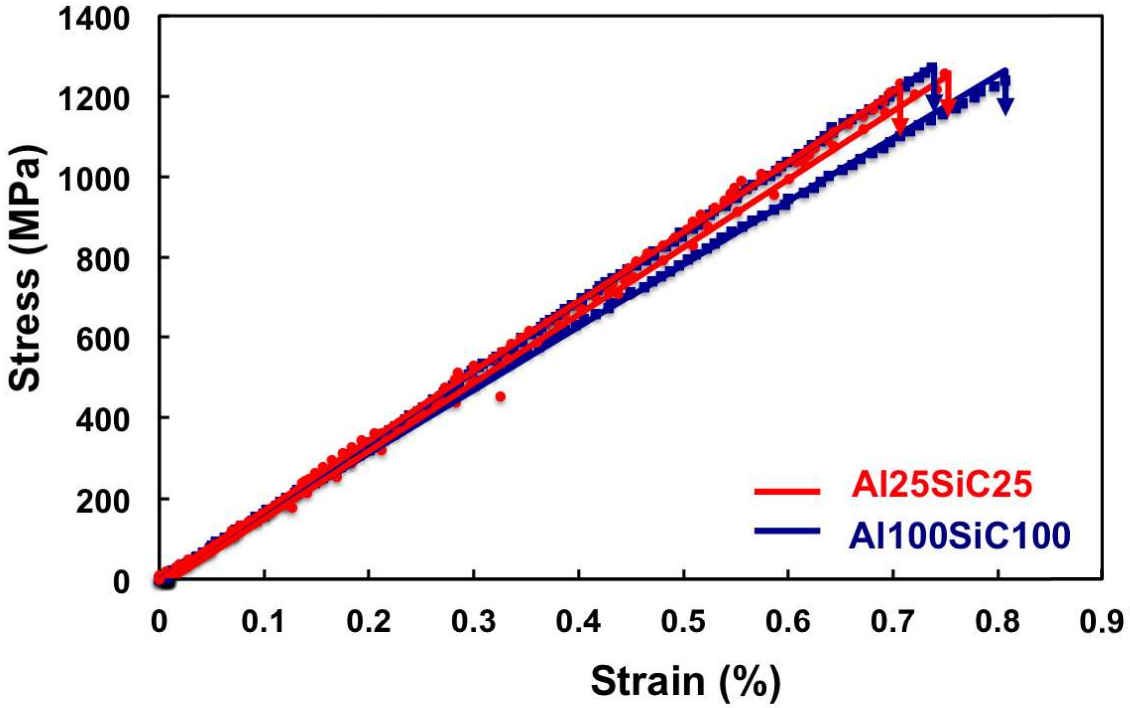

Figure 33: Stress-Strain curves of Al/SiC nanolaminates tested at 0°. Tensile strength is not affected by layer thickness.

The Young's modulus of the samples did not change with layer thickness, as the volume fraction of the constituents was maintained constant at 0.5. An experimentally achieved modulus value of 173 ± 4 GPa was compared with the calculated modulus from the rule of mixtures under an isostrain condition according to the following equation:

$$E_C = E_{Al}V_{Al} + E_{SiC}V_{SiC} \quad (2)$$

Individual modulus values of SiC, 300 GPa and Al, 70 GPa were used and the resultant modulus of the composite under an isostrain condition was calculated as 185 GPa, which is very close to the experimentally obtained value.

The tensile strength of the MEMS samples was not affected by the layer

thickness. Loaded in an isostrain condition most of the load bearing is done by SiC layers and thus they determine the deformation behavior. It has been previously reported that the modulus and hardness of the SiC monolayers did not change with layer thickness indicating the defect distribution to be independent of it (Xin Deng et al. 2005). Moreover, in nanoindentation studies of Al/SiC multilayers hardness of the nanolaminates having constant SiC layer thickness increased nonlinearly as the Al volume fraction decreased (Yang et al. 2016). On the other hand, nanolaminates with constant Al thickness and varying SiC thickness showed a linear increase of hardness as the Al volume fraction decreased (Yang et al. 2016). This also indicates that the strength of the Al layers depends on the layer thickness, because of its nanocrystalline microstructure, while the strength of the amorphous SiC layers is independent of size. Therefore, the tensile strength of Al/SiC nanolaminates under an isostrain condition was not affected by layer thickness.

The fracture surface of the samples is shown in Figure 34. From the figure, it is evident that the surface is very planar and any evidence supporting crack deflection at the interface could not be found. Therefore, it is understandable that the tensile strength or strain to failure did not change for Al25SiC25 and Al100SiC100 despite having a huge difference in the number of interfaces.

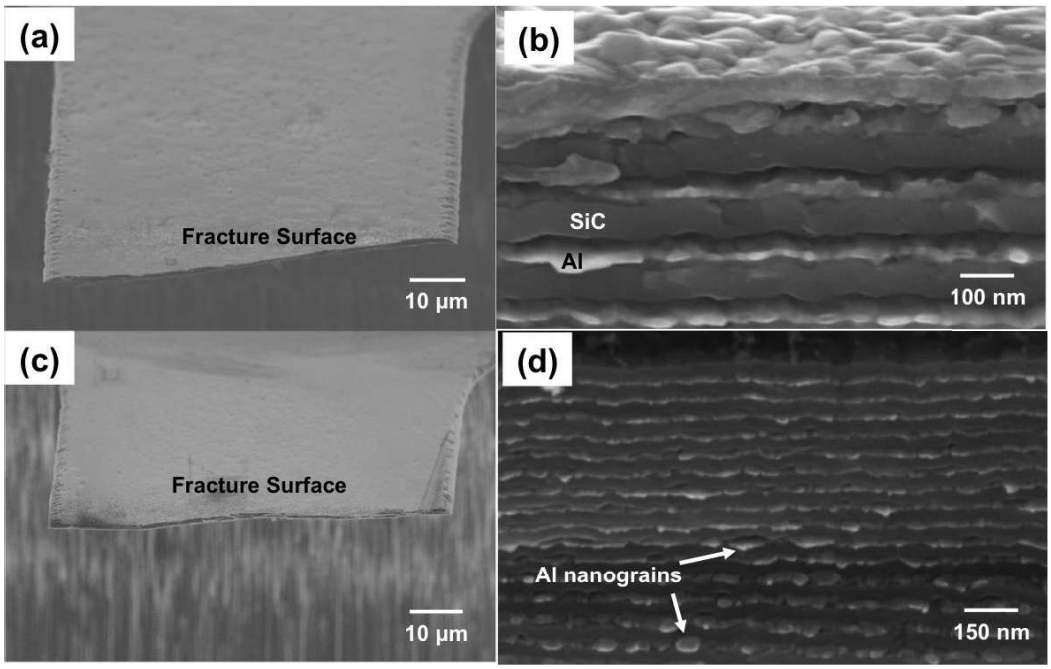

Figure 34: Fracture surface of Al100SiC100 (a,b) and Al25SiC25 (c,d). From the high magnification image of fracture surface no evidence of crack deflection was observed.

These results were compared with work done in collaboration on FIB milled dog-bone specimens. The engineering stress-displacement curves of the Al/SiC FIB milled dog-bone samples performed at 90° and 0° orientations with respect to the layers are plotted in Figure 35(a) and Figure 35(b), respectively (Yang 2017). These results are reported here for the purpose of comparative analysis. The arrow on each curve indicates the sudden failure of the sample. Some of the tests at 90º were either interrupted at several steps, like Al50SiC50, or unloaded, as for Al100SiC100, to acquire high resolution SEM images. The tests carried out at 0º were performed without interruption up to final failure.

The microtensile specimens displayed a brittle response in both loading

directions. Attempts to measure the strain just before fracture by DIC yielded strain levels below the resolution of the SEM images. However, based on the shape of the curves, the microtensile tests carried out at 90º show a non-linear behavior, while the tests carried out at 0º are linear until failure. Therefore, some limited Al plasticity cannot be ruled out at 90º, although the overall behavior is still very brittle. The difference between the 0º and 90º orientations is not surprising, considering that the layers deform under isostrain conditions in the former, and therefore, the SiC sustained most of the load. On the other hand, isostress conditions prevailed in the latter and the stress levels on the Al layers were much higher. Intriguingly, the tensile strength of the 90º and 0º microtensile specimens was independent of layer thickness. In all cases, the nanolaminates at 90° failed at ~1.22 GPa, while the tensile strength was significantly lower, ~0.62 GPa, at 0º loading. From the post-deformation image, it became clear that the nanolmainates are failing at the interface for 90º loading and at columnar boundaries for 0º loading. Therefore the behavior was independent of layer thickness.

The tensile properties are very different from the compressive behavior reported previously (C. R. Mayer et al. 2016). Not only are the failure strengths much lower under tension, but also the behavior is also very brittle, and independent of the layer thickness. These results point towards two very important characteristics of Al/SiC nanolaminates; first is the asymmetry in tension-compression behavior and second is the difference in tensile behavior of FIB milled dog-bone and MEMS based dog-bone samples.

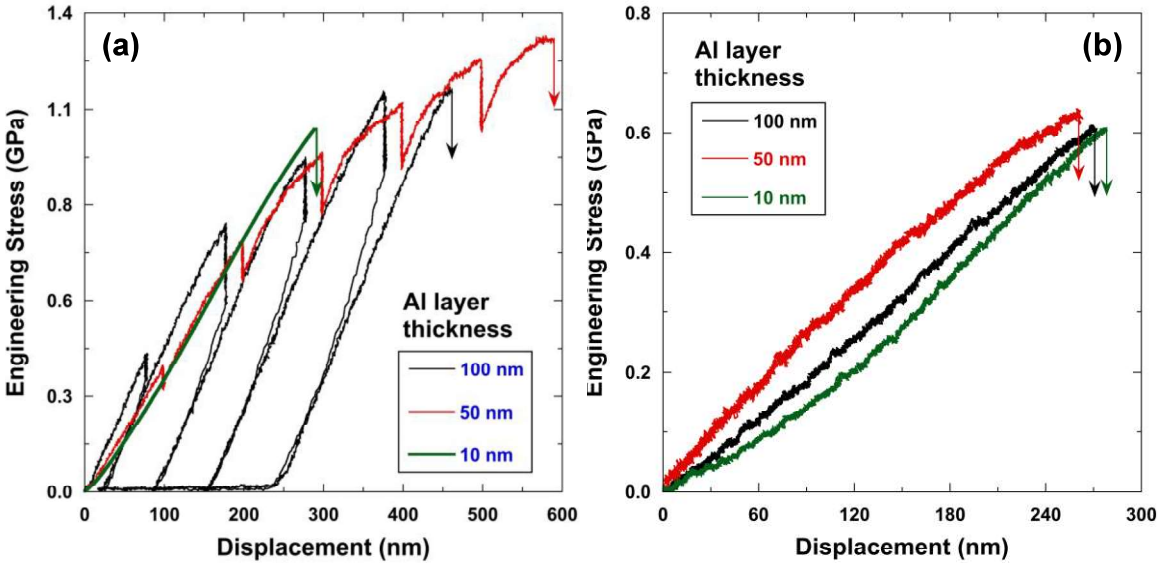

Figure 35: Microtensile stress-displacement curves of Al/SiC nanolaminates tested at (a) 90° and (b) 0° (Yang 2017).

For the analysis of former, these results were compared with the micropillar compression of 2 x 4 μm and 2 x 6 μm micropillars having a volume of 12.6 μm^3 and 19 μm^3 respectively (C. R. Mayer et al. 2016). Despite having a higher volume, the strength of these micropillars was higher (~ 2.2 GPa) than the FIB milled dog-bone samples. During tensile loading, stresses are applied in Mode I on the pores while compressive stresses load the pores indirectly, either through circumferential tensile stress, or in Mode II through a resolved shear stress, which leads to a delay in onset of fracture. Therefore, Al/SiC nanolaminates display a brittle behavior and have much lower strength when loaded in tension. Effect of layer thickness was also studied on the compression behavior of micropillars having layers perpendicular to the loading direction (Yang et al. 2018). With a decrease in layer thickness a significant increase in compressive strength was reported, contrary to the tensile strength studies (Yang et al. 2018). This highlights the

extent of asymmetry in the tension-compression behavior of these materials. Multiple reasons contribute towards this phenomenon; in both cases the layers are in an isostress condition but in compression the plastic flow of Al layers is restricted by the stiffer SiC layers. Due to the presence of a strong interface, hydrostatic stresses are developed and lead to strain hardening (C. R. Mayer et al. 2016; Yang et al. 2018). The deformation is therefore dependent on the imposed constraint which increases with a decrease in layer thickness thereby increasing the compressive strength of micropillars (Yang et al. 2018). On the other hand, in tension, the dog-bone samples failed at the interface. Thus, the failure depends on the interfacial strength and is independent of layer thickness.

Another interesting observation from these results was the fact that the tensile strength of MEMS devices was twice as high as that of FIB milled samples. This becomes more interesting given that the volume of the MEMS samples was much higher than that of the FIB milled dog-bones. This difference in strength is mainly because FIB milling was done at the top region of the sample, where maximum layer waviness and defects were present as shown in Figure 31. Porosity at the columnar boundaries combined with the small radius of curvature acts as sites of stress concentration and leads to weak regions in the microstructure. However, MEMS samples were made by etching out the Si substrate, and had no visible defects. Thus, for the same composition and layer thickness of nanolaminates, the properties varied drastically and have dependence on pores as well as the wavy nature of layers.

To ascertain that the increase in tensile strength was due to the absence of layer waviness and pores and not a byproduct of change in the testing method i.e. between FIB

milled dog-bone and MEMS devices, nanoindentation was performed to evaluate the modulus and hardness of the synthesized samples. Representative modulus and hardness versus displacement curves have been shown for Al25SiC25 in Figure 36 and Figure 37 respectively.

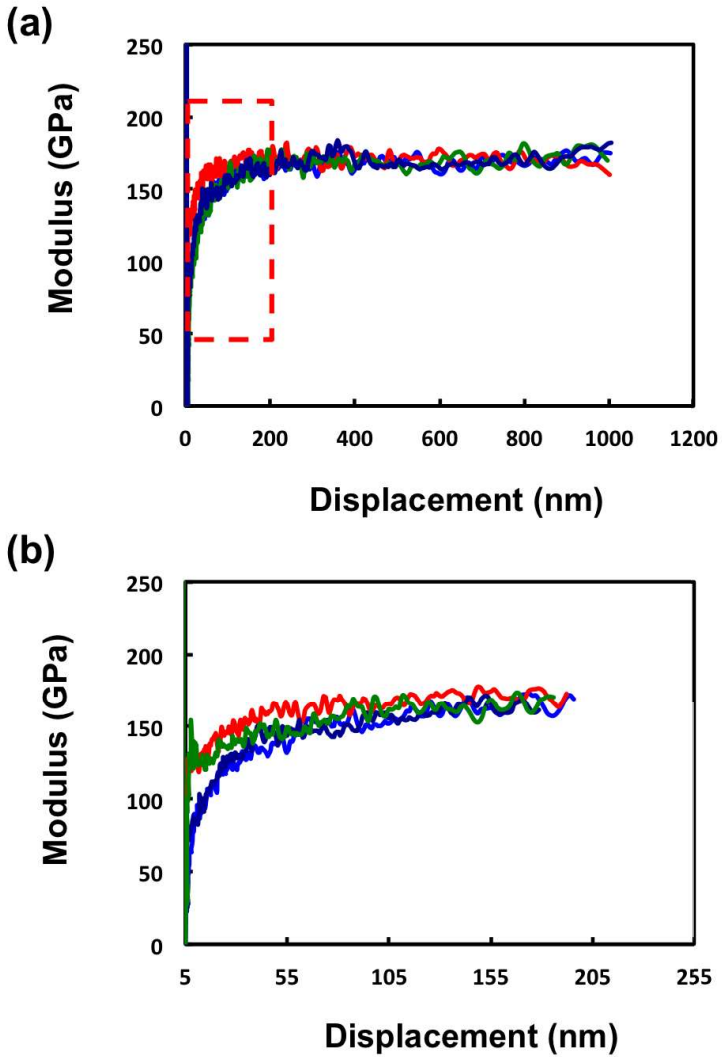

Figure 36: Representative modulus versus displacement curves for (a) Al25SiC25, the magnified version of the curve is shown in (b). Values below displacement of 125 nm were used for calculation.

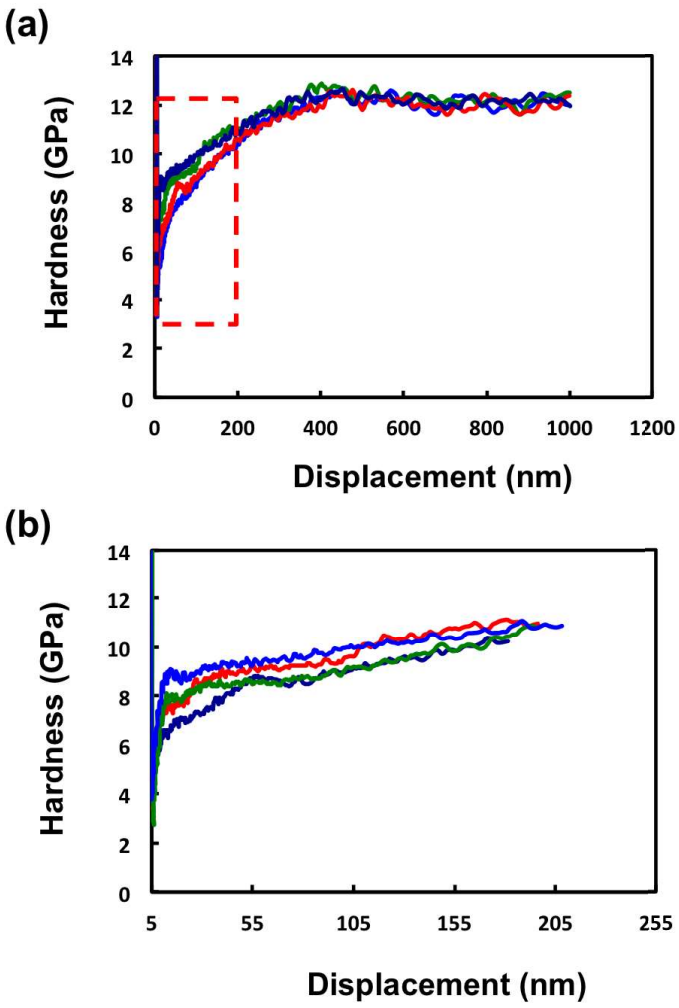

Figure 37: Representative hardness versus displacement curves for (a) Al25SiC25, the magnified version of the curve is shown in (b). Values below displacement of 125 nm were used for calculation.

Since the total thickness of the film was 1 μm displacement values less than 125 nm were used for calculating the modulus values. The magnified image of the curve has also been shown in the figures.

Traditional nanolaminates have modulus values of ~ 111 GPa and nanolaminates

with total thickness of 1 μm have modulus values of ~ 150 GPa as shown in *Table 2* (C. Mayer et al. 2016). A 35 % increase was seen in the modulus value, which can be attributed to the absence of deposition-induced defects in the microstructure. A similar increase in the hardness value was also observed. It should be noted that with a decrease in layer thickness and increase in hardness value is seen. This is because of increase in yield strength of Al grains, which have grain size comparable to layer thickness.

Sample	Young's Modulus (GPa)	Hardness (GPa)
Al25SiC25	153 ± 7.5	8.6 ± 0.4
Al50SiC50	140 ± 6	7.5 ± 0.5
Al100SiC100	141 ± 8	5.8 ± 0.4

Table 2: Young's modulus and Hardness of Al/SiC nanolaminates having a total thickness of 1 μm. The modulus and hardness is greater than traditional nanolaminates owing to the absence of pores and wavy microstructure.

4.4 Summary

Microtensile tests were performed on the dog-bone samples from MEMS devices of Al/SiC nanolaminates having different layer thicknesses. Tensile strength of MEMS device based dog-bone samples was independent of layer thickness. However, these samples were twice as strong and had higher volume as compared to the FIB milled dog-bone samples. The higher strength despite a higher volume was due to the absence of pores and layer waviness in these samples. This was confirmed by nanoindentation

results, where it was observed that the Young's modulus of samples having total thickness of 1 μm was 35 % higher than that of traditional nanolaminate having total thickness of ~ 20 μm. Al/SiC nanolaminates have a significant tension-compression asymmetry in their mechanical behavior. This is due to the flaw dependent deformation behavior of these nanolaminates. In tension, the flaws are loaded directly in mode I whereas in compression they are either loaded in mode I indirectly or mode II, thereby delaying fracture and yielding higher strengths.

CHAPTER 5

DEFORMATION BEHAVIOR OF Al/SIC NANOLAMINATES UNDER *IN SITU* CYCLIC LOADING

5.1 Introduction

It is necessary to investigate the fatigue behavior of materials as they often lead to catastrophic failures. As discussed above, the sample volume of nanolaminates poses restriction on the testing techniques that can be used for characterizing their mechanical behavior. Experiments like compression, indentation and challenges associated with them have been well studied and established. However, lesser amount of work has been done on studying the fatigue properties at microscale. Majority of the work that has been done utilizes the following techniques: continuous stiffness measurement associated with indentation loading (Kraft et al. 2001; Cavaliere 2010; Li & Bhushan 2002b), cyclic loading on microcantilever beams fabricated through photolithography or FIB milling(Kwak et al. 2010; Maekawa et al. 1999; Lavenstein et al. 2018) and uniaxial compressive or tensile cyclic loading (Schamel et al. 2016; Szczepanski et al. 2013). CSM method uses small harmonic load frequencies, which is superimposed on the indentation load, this technique is limited to the film-substrate sample set. On the other hand FIB milled dog-bone geometries require complex milling steps for both the sample and the grip, making it a very time consuming process. Therefore, fatigue tests on microcantilever beams have been relatively more popular.

The fatigue properties of Al-SiC composites have been widely studied. The combination of aluminum metal with ceramic SiC promises a composite with superior strength and ductility. Addition of stiffer SiC into Al matrix has known to cause its strengthening through both direct and indirect methods (Chawla et al. 1998; Chawla et al. 2000). The effect of particle size, volume fraction and microstructure of matrix has been evaluated systematically. An increase in SiC volume fraction and/or a decrease in SiC particle size increased the fatigue life of the MMCs (Chawla et al. 1998). The increased volume fraction helped in load transfer to stiff SiC particles thus reducing the overall strain on MMCs and with a reduction in inter-particle spacing hindrance in dislocation motion was achieved. Further, the effect of R-ratios and crack growth morphology have been studied in 3D through X-ray tomography (Williams et al. 2010; Hruby et al. 2014). It was reported that with an increase in R-ratio the crack path is less tortuous and crack proceeds through breaking SiC particles. This behavior changes with a reduction in R-ratio and crack follows a tortuous path and grows around the SiC particles (Hruby et al. 2014). Therefore, significant improvements in fatigue behavior have been reported through combination of Al and SiC. However, to the best of author's knowledge the fatigue behavior of Al/SiC nanolaminates has not been studied till now owing to the complex nature of experimental design required. In this work, *in situ* fatigue tests have been conducted for Al100/SiC100 nanolaminate through cyclic bending of FIB-milled microcantilevers. Fatigue life was evaluated as a function of change in loading amplitudes and maximum loads. 4 different values of maximum loads were imposed on the beam while keeping the R-ratio constant at 0.2.

5.2 Materials and Experimental Procedure

Microcantilever beams were fabricated using a commercial FIB/SEM (Auriga, Carl Zeiss X-ray Microscopy Inc., CA) with an ion beam accelerating voltage of 30 kV. Nanolaminate wafer having a dimension of approximately 3 x 4 mm was mounted on a stainless steel stub using a crystal bond. The microcantilever beams were fabricated at the edge of the wafer and the length of the beam was milled parallel to the sample edge to achieve simultaneous loading and capturing of the deformation. First a beam current of 16 nA was used to mill a trench 20 x 20 x 30 μm. Milling was performed parallel to the sample surface and cross-section. For this, a pre-tilt holder was used having a 45º angle so that an 180º rotation would render either the sample surface or the cross-section perpendicular to the ion beam. After this step, a milling current of 4 nA was used to create a cuboidal bar 8 x 8 x 20 μm. Final dimension of 5 x 5 x 17 μm was achieved by subsequent polishing steps carried out at 1 nA and 50 pA respectively. 6 microcantilever beams were fabricated using the same milling steps to avoid any effect of the fabrication process on the S-N curve trend.

In situ fatigue tests were conducted using a commercial nanoindenter FT-NMT03 (FemtoTools AG, ZH, Switzerland) inside the FIB/SEM (Figure 38). The stainless steel stub with the nanolaminate wafer containing microcantilever beams was mounted on the sample holder of the nanoindenter. Further, the nanoindenter was mounted on the stage of FIB/SEM and tilted to a 15º angle. This setup allows for simultaneous loading and imaging of the sample surface as explained in Figure 39. Microforce sensing probe, FT-

S20'000 having a maximum force of 20 mN and a load resolution 0.5 μN was used for loading. The tungsten probe tip had a tip radius of 2 μm which was convenient for loading beams having a width of 5 μm. For loading, the indenter tip was carefully positioned 14.25 μms away from the fixed edge of the sample. Care was taken to ensure that the center of the tip matches with the center of the width of the beam. These steps are important to avoid the fluctuation in applied stress that can be caused by the change in the position of the tip relative to the sample edge. Fatigue tests were conducted in a load-controlled mode. Four different maximum loads were applied to the sample to obtain the S-N curve. R-ratio of 0.2 and frequency of 40 Hz was maintained for all the tests.

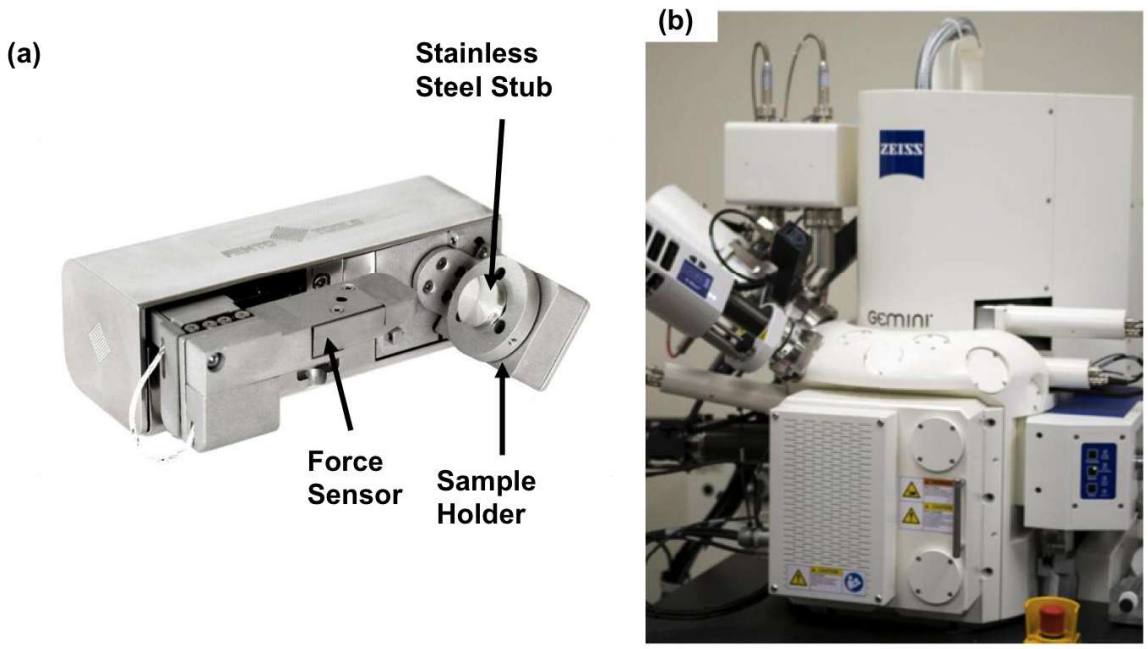

Figure 38: (a) FT - NMT03 *in situ* indenter, the sample holder holds the stainless steel stub which contains nanolaminate sample with the microcantilever beams (b) Zeiss Auriga FIB/SEM where the nanoindeter is placed for simultaneous imaging and loading.

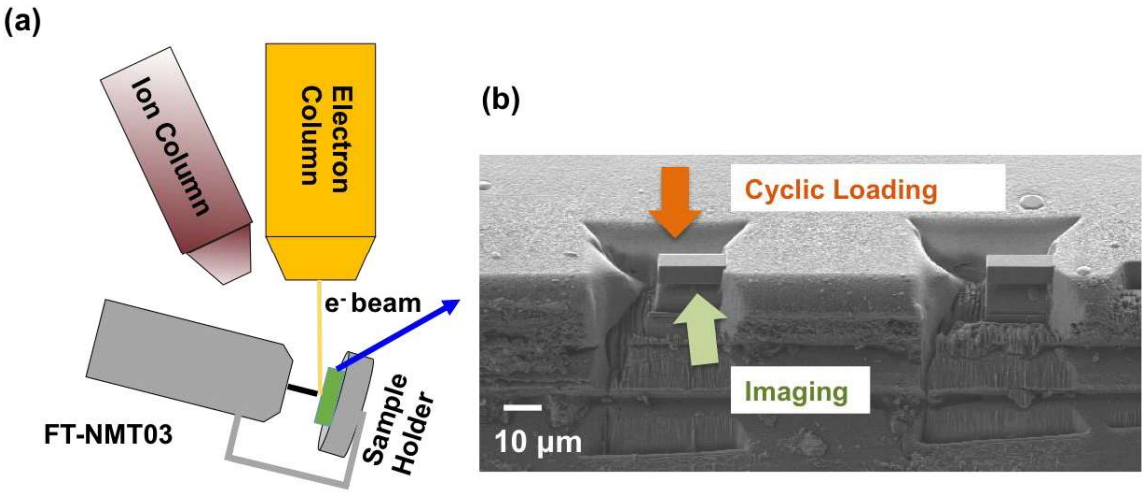

Figure 39: (a) schematic explaining the set up for *in situ* fatigue loading (b) Al/SiC nanolaminate sample containing microcantilever beams at the sample edge for the experiment.

The applied force is directly measured by the nanorobotic system, displayed in GUI and is recorded at a frequency of 3 kHz. However, the actual displacement of the sample needs to be calculated manually. As shown in Figure 40, when a force is applied, not just the sample but the entire system deforms. The sample holder, stub and microforce sensor are expected to have some displacement. The output displacement value is thus the total displacement and not just of the sample alone. The displacement of the sample is calculated as explained through the equations below. The force is same on the sample and measurement system (which collectively represents the stub, sensor etc). To find the displacement of the measure system under a given load, it is important to obtain its stiffness. This was done through nanoindentation on the stainless steel stub, beside the nanolaminate wafer. Once the stiffness of the measurement system is obtained, its displacement, d_m can be calculated for a given force. Therefore, the displacement of

the sample can be calculated by subtracting d_m from the total displacement (d_T) which is obtained through the software.

$$F_T = F_S = F_M \tag{3}$$

$$d_T = d_S + d_M \tag{4}$$

$$F_M = k_M . d_M \tag{5}$$

$$d_T = d_S - d_M \tag{6}$$

$$d_S = d_T - \frac{F_m}{k_m} \tag{7}$$

F_T, F_S and F_M are the total force, force on the sample and force on the measurement system respectively. d_T, d_S and d_M are the total displacement, displacement on the sample and displacement on the measurement system respectively. k_M is the stiffness of the measurement system which in this case was calculated to be 7476 N/m.

The test was interrupted after regular intervals of time to acquire a high resolution SEM image. This step was conducted to capture visible damage on sample surface and to correct for drift during post-processing of the data.

5.3 Results and Discussion

The loading conditions used for the fatigue test has been shown in Table 3. Stress and Strain on the sample was calculated through beam bending equations. The scaling coefficients of the equations have been obtained through FEM modeling (Mayer 2016).

$$\sigma = 3.25PL/BW^2 \tag{8}$$

$$\varepsilon = 0.63DW/L^2 \tag{9}$$

Here P is the load; D is the displacement; B,W and L are the breadth, width and length of the microcantilever beam respectively.

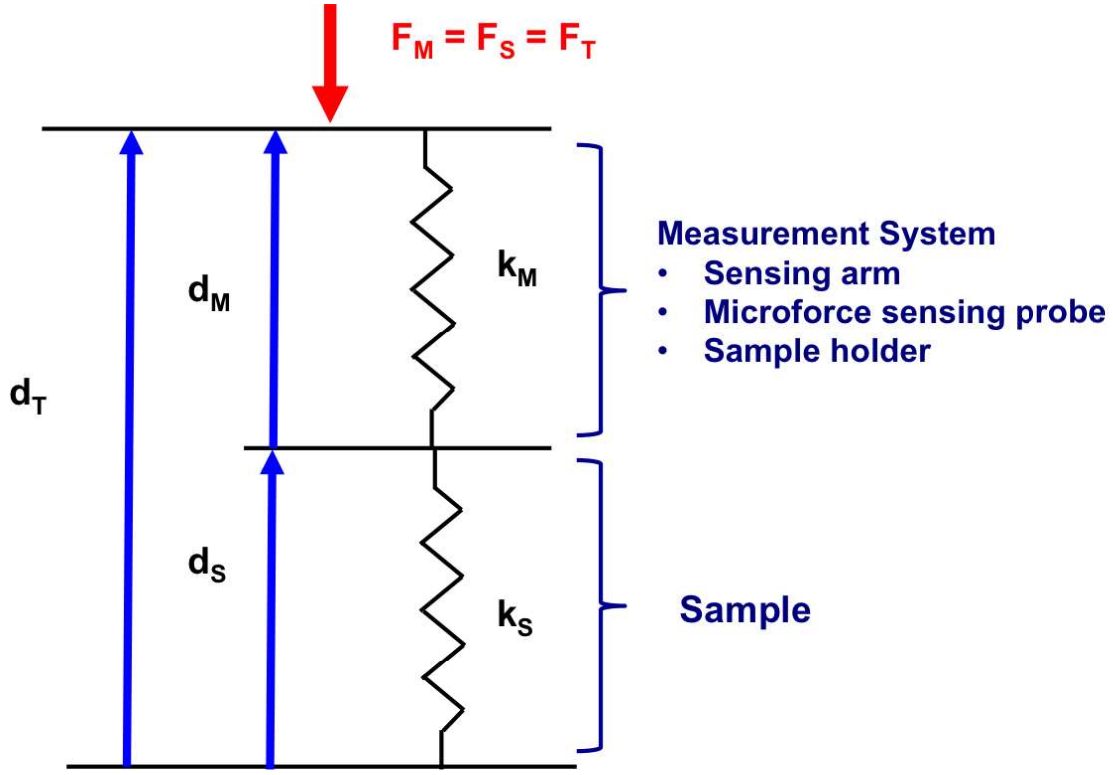

Figure 40: Schematic showing the relation between the total displacement, displacement of sample and measurement system.

Test	Max Load (μN)	Min Load (μN)	Amplitude (μN)	Max Stress (MPa)	Number of cycles
1	2400	480	1920	888	7,893
2	2200	440	1760	813	11,200
3	2150	430	1720	795	112,008
4	2125	425	1700	786.2	1 million (without failure)

Table 3: Loading conditions for the fatigue tests conducted on Al/SiC nanolaminate. Frequency of 40 Hz and R-ratio 0f 0.2 was maintained for all the tests.

The experimentally obtained S-N curve has been shown in Figure 41. With a decrease in maximum stress σ_{max} an increase in number of cycles to failure was observed. For bulk materials, a fatigue run-out is established at a stress at which the specimen sustains 10^7 cycles without failure (Dieter et al. 1988) . In this case, it was practically difficult to complete these many cycles, keeping in mind that the tests were being conducted inside the FIB/SEM. As can be seen from the S-N curve the microcantilever beam did not fail till 10^6 cycles at a maximum stress of 786 MPa. This was established as the fatigue run-out point for Al/SiC nanolaminate sample. A considerable increase is observed from the reported value of fatigue run-out of 110 MPa for bulk SiC (Ritchie et al. n.d.). This can be attributed to the addition of Al, layered morphology as well as reduction in sample volume, which leads to strengthening based on Griffith's theory (Dieter et al. 1988). The S-N curve for bulk Al continuously slopes down without providing a distinct fatigue run-out point and the stress value that is sustained for 10^8 cycles is established as the fatigue strength of Al (Dieter et al. 1988). Therefore, a considerable difference in behavior is observed for Al/SiC nanolaminates, which has a

well established fatigue run-out point.

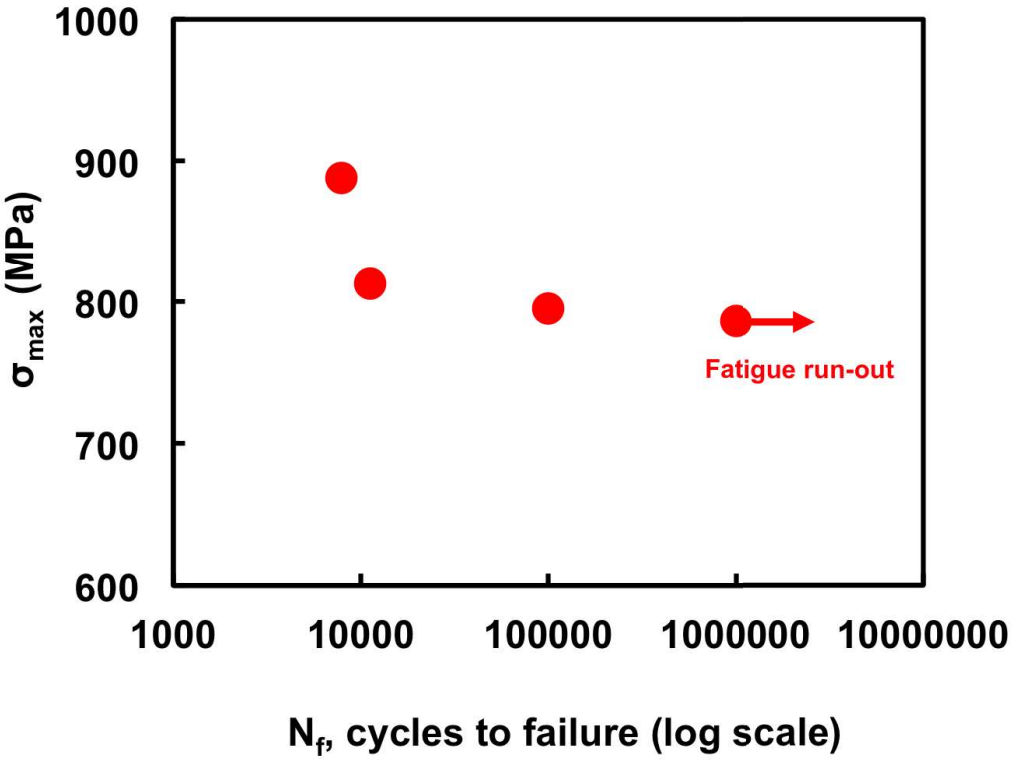

Figure 41: S-N curve for load controlled fatigue test of Al/SiC nanolaminate having layer thickness of 100 nm. The fatigue run-out was established at 10^6 cycles.

Loading was performed at a frequency of 40 Hz and the displacement was obtained for each point using the set of equations described above. A typical load versus time and displacement versus time graph for the first test has been shown in Figure 42. Periodic cycles having a time period of 0.025 secs can be observed which is in accordance with the input value of frequency.

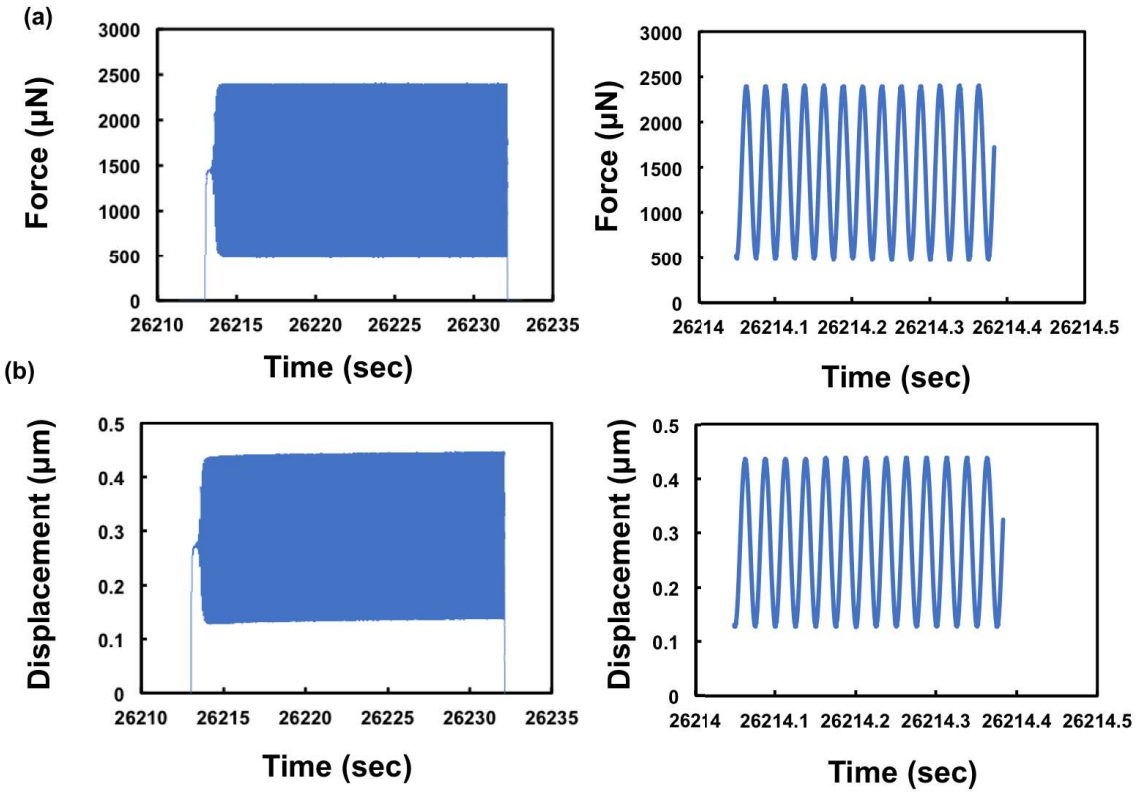

Figure 42: (a) Load versus time and (b) displacement versus time for fatigue test having a maximum stress of 888 MPa. The cycle time of 0.025 secs is in accordance with the input frequency of 40 Hz.

The phase angle (Φ) between the load and the displacement was negligible and hence no phase shift is seen between the oscillating load and displacement curves. The dynamic stiffness at each point is calculated by the following equation.

$$S = \left(F_{max} / d_{max}\right)\cos\Phi \tag{10}$$

Since this is a cosine function, with phase angle being close to zero its effect on dynamic stiffness is negligible. Stiffness of a material is representative of its response to loading in the elastic regime and provides information on the condition of sample being tested. A

decrease in stiffness value indicates damage and therefore a decrease in load bearing capacity of the sample. On the other hand, an increase in stiffness value can help understanding mechanisms like cyclic hardening which is common for metals under cyclic loading (Dieter et al. 1988). Therefore, monitoring the stiffness value throughout a fatigue test is very useful and provides insight about cyclic hardening, softening, crack initiation and growth.

The test was interrupted after certain time intervals to acquire high-resolution SEM images as shown in Figure 43. For the majority of loading cycles, there were no indications of crack initiation or any surface damage on the beam. These images were also used for correcting the effect of drift on stiffness values. Additional information was gathered from the videos acquired during the cyclic fatigue. Presence of crack was observed merely ~ 0.30 seconds before the complete failure and this was captured in the acquired video (Figure 44). Crack growth can be observed for loading condition having a maximum stress of 813 MPa as shown by the yellow arrows. This was particularly interesting because the frame rate for the video was 0.10 seconds. Since each load cycle takes 0.025 seconds, this indicates that after the crack appeared on the beam surface it sustained at least four cycles before complete failure.

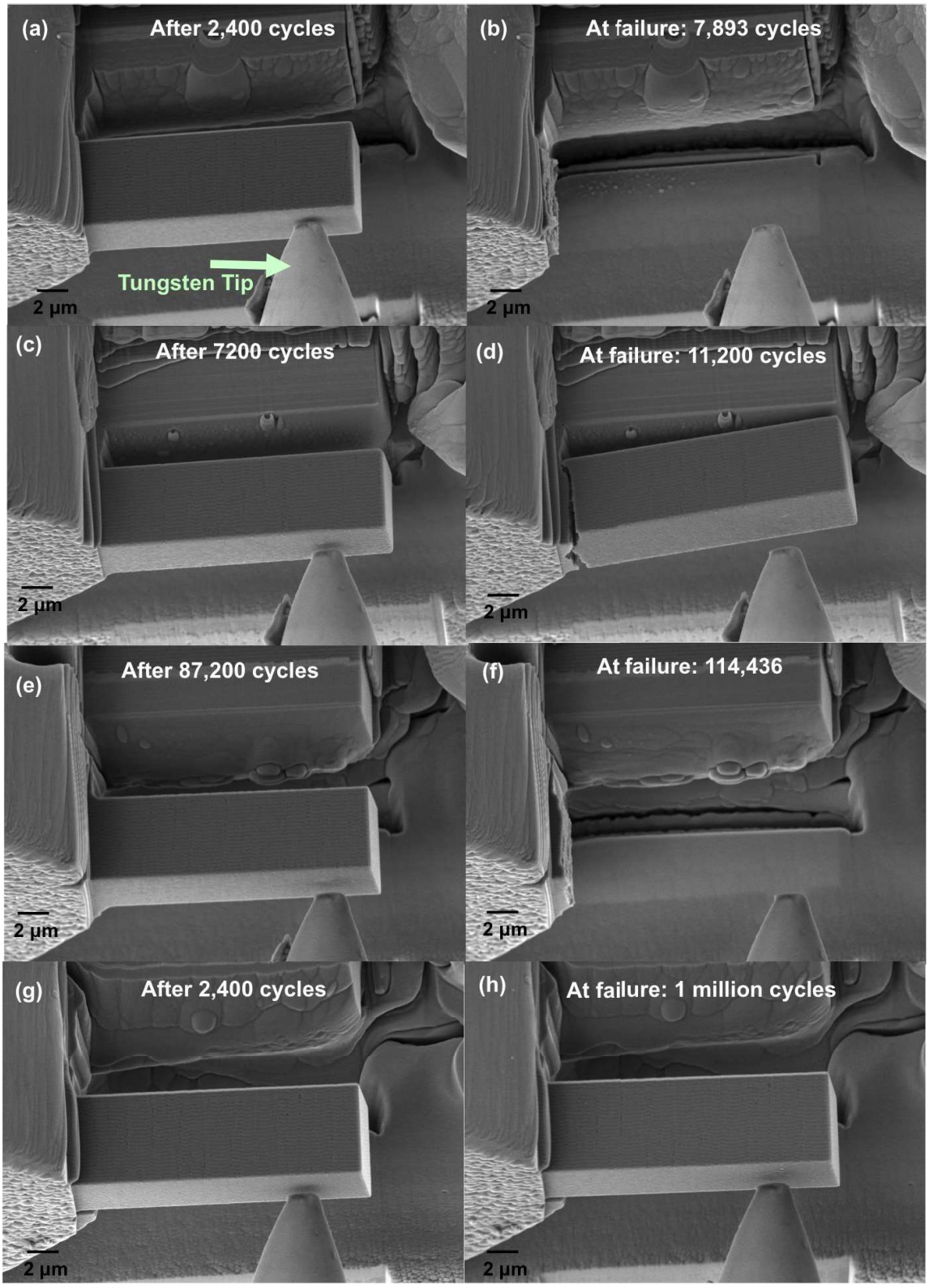
(a)
After 2,400 cycles
Tungsten Tip
2 µm
(b)
At failure: 7,893 cycles
2 µm
(c)
After 7200 cycles
2 µm
(d)
At failure: 11,200 cycles
2 µm
(e)
After 87,200 cycles
2 µm
(f)
At failure: 114,436
2 µm
(g)
After 2,400 cycles
2 µm
(h)
At failure: 1 million cycles
2 µm

Figure 43: SEM images for cyclic fatigue at a maximum stress of (a,b) 888 MPa, (c,d) 813 MPa (e,f) 795 MPa and (g,h) 786 MPa. In the first three cases the failure was instantaneous and for the last case the beam did not fail or show any signs of damage till 1 million cycles.

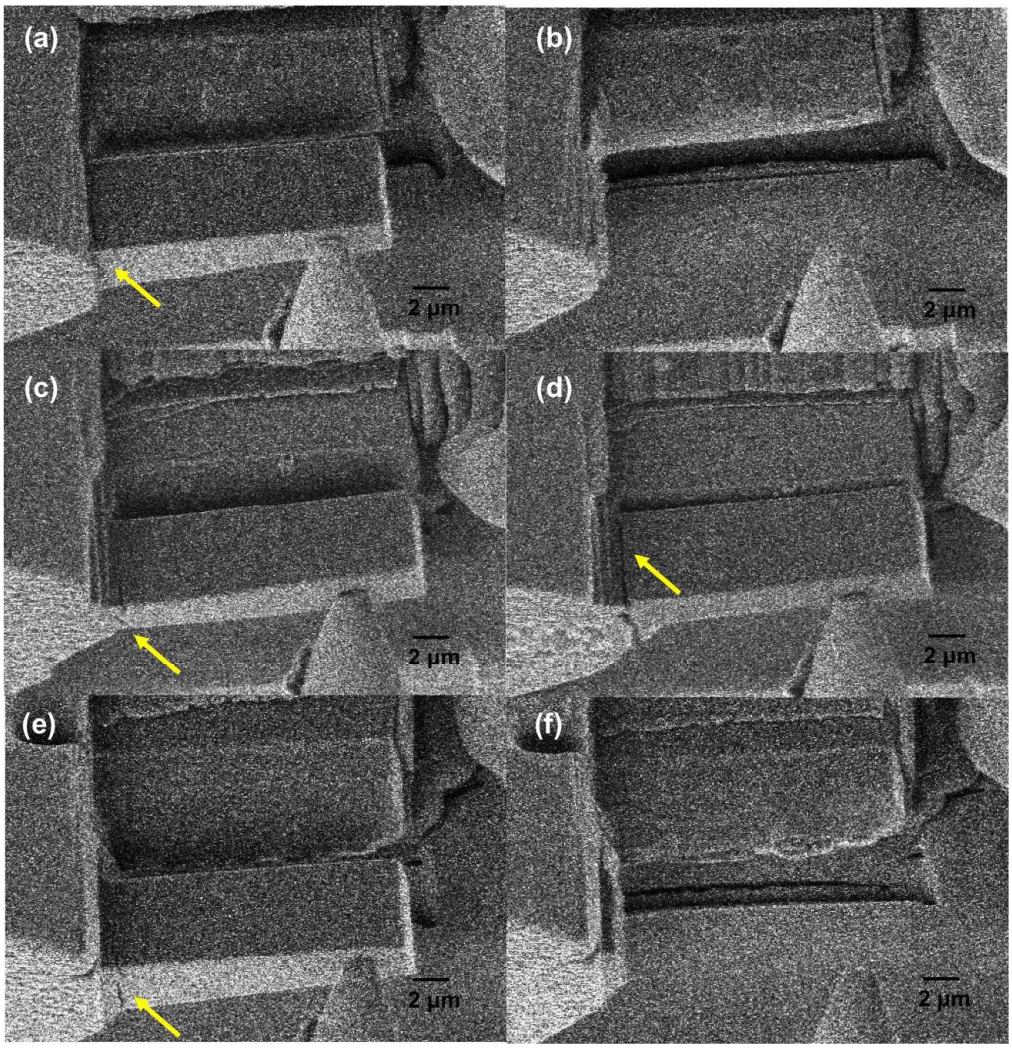

Figure 44: Snapshots from the video during the test at a maximum stress of (a,b) 888 MPa, (c,d) 813 MPa (e,f) 795 MPa. The yellow arrows point towards the cracks that appeared on the beam surface.

As mentioned earlier, the beams failed catastrophically and this behavior was consistent for all the loading conditions i.e. high stress amplitude where the beam failed within 7,893 cycles as well as low stress amplitude where the beam failed after 114,436 cycles. This is indicative of the brittle nature of Al/SiC nanolaminates independent of the applied stress.

Additional information about the deformation was gathered from the evaluation of stiffness, load versus displacement and maximum/minimum strain plots. From the stiffness plot, it should be noted that irrespective of the stress value, the nature of curve remains unchanged (Figure 45). The stiffness does not change through majority of cycles and a dramatic drop in the values is observed in the last segment, as pointed by black arrows. Therefore, the beam did not undergo hardening or softening during cyclic fatigue.

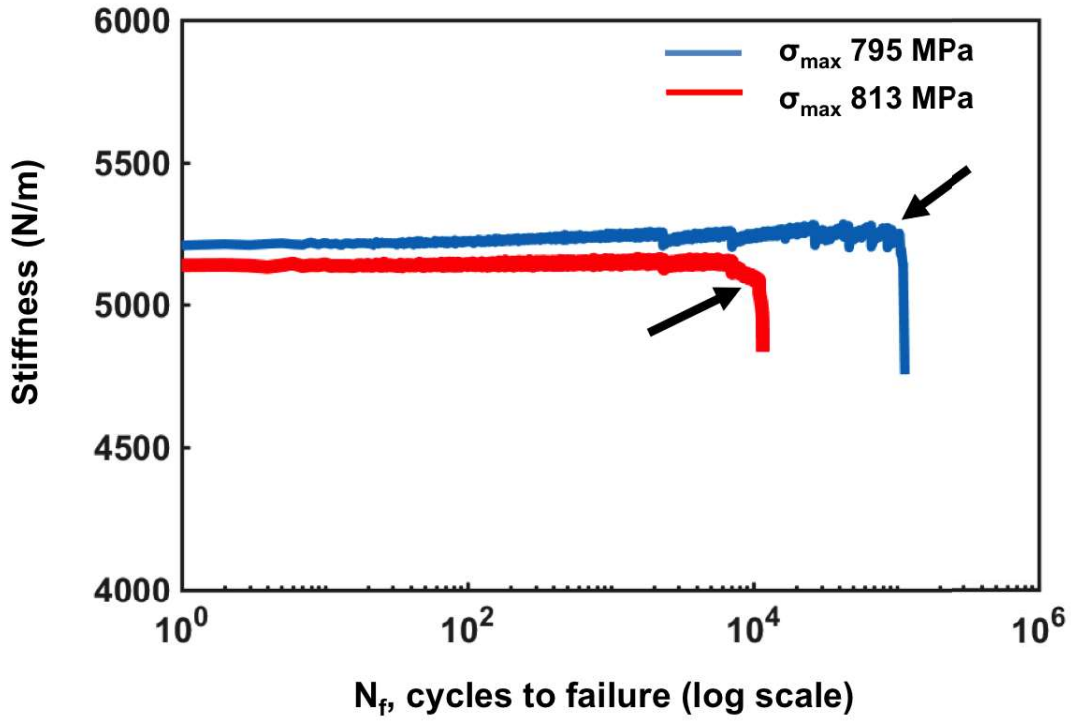

Figure 45: Stiffness versus number of cycles for fatigue tests performed at maximum stress of 813 MPa and 795 MPa respectively. A steep drop in stiffness can be observed.

The steep drop in stiffness is indicative of microcrack initiation and propagation in the beams leading to its weakening. When a crack initiates it leads to a decrease in the load bearing cross-section area of the beam until it fails under the given cyclic load. With a decrease in capability of bearing the load, the same load will lead to higher displacements in the beam when continued cycling in the load-controlled mode. This was verified through the trend of maximum and minimum strain on the beam. These values also remain constant like the stiffness. However, with a decrease in stiffness values an increase in displacement and thereby an increase in minimum and maximum strain can be observed until failure (Figure 46).

Further, the load-displacement and stress-strain curves were plotted for the beam and a small hysteresis loop can be observed for each cycle (Figure 47). A very small area under the curve is indicative of the energy spent through cycling. For case of bulk metals, it is easy to distinguish between the elastic and plastic strain from the linear and non-linear parts of the stress-strain curve. However, in the present case the displacement values are in the order of nanometers and the plastic strain is negligible. Moreover, the increase in strain for the same values of load can be clearly noted from the stress-strain cycles. Again, for the large part of the test, the stress-strain behavior remains unchanged. However, with the start of damage in the beam an increase in the strain values for the same stress values can be observed.

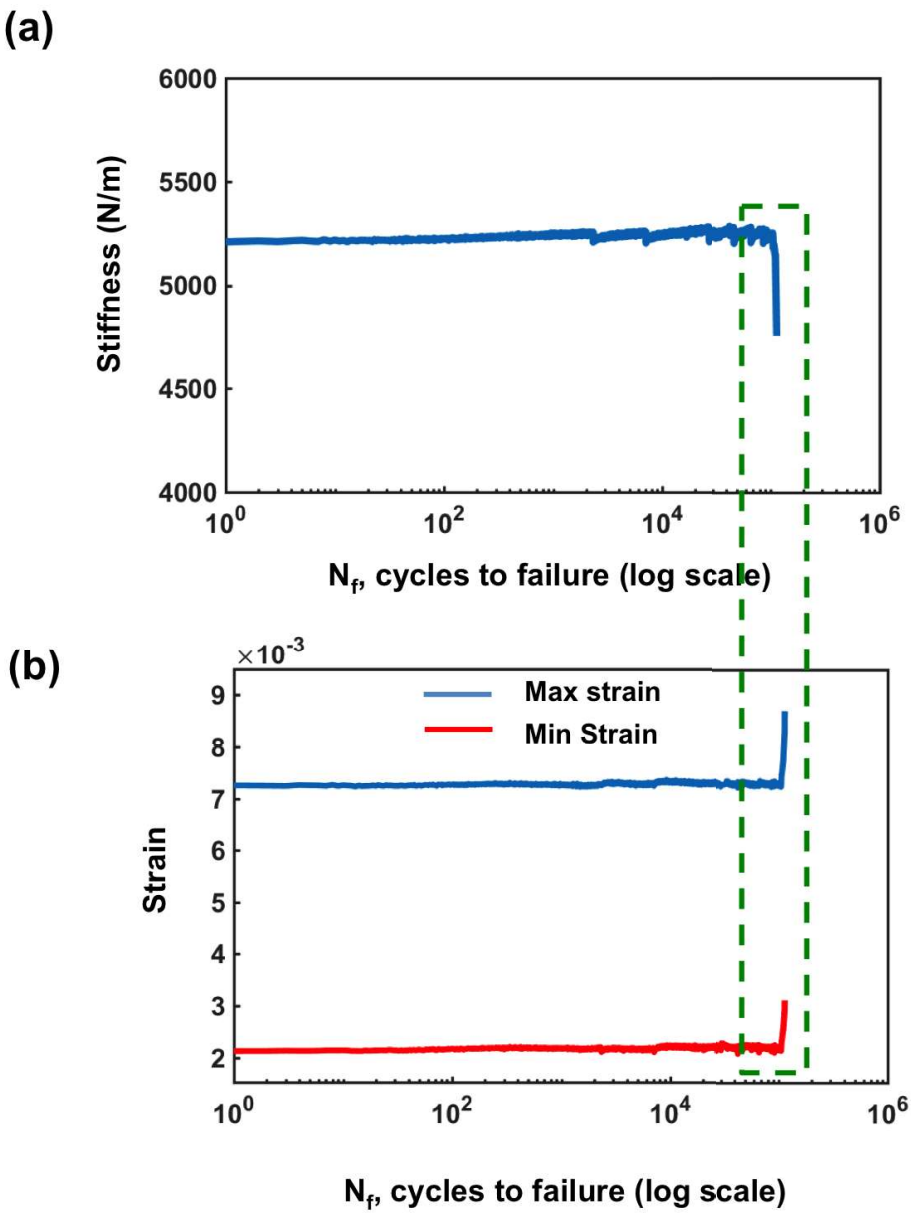

Figure 46: (a) Stiffness versus number of cycles (b) maximum and minimum strain versus number of cycles for fatigue test conducted at a maximum stress value of 786 MPa. With a decrease in stiffness an increase in the strain can be observed as the beam undergoes higher displacement for the same load.

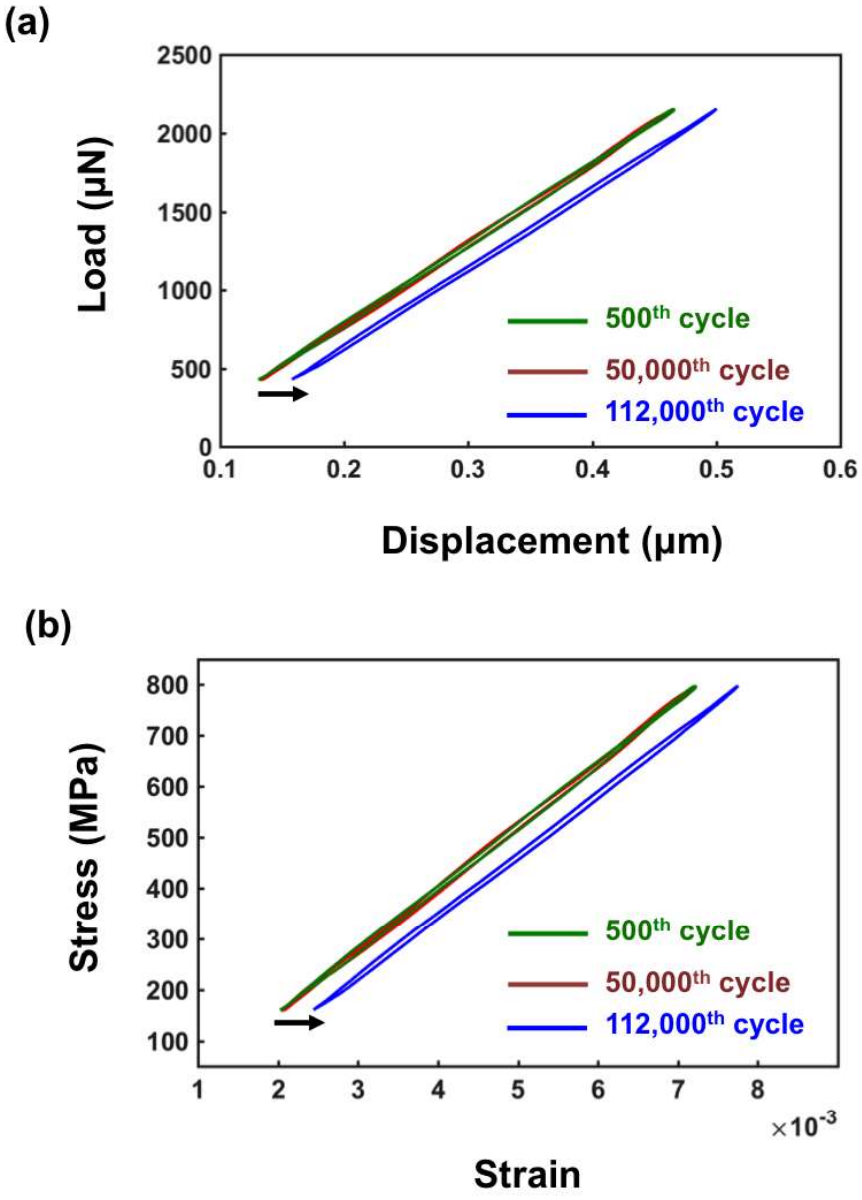

Figure 47: (a) load-displacement and (b) stress-strain curves for fatigue test conducted at a maximum stress value of 786 MPa. An increase in displacement for the same loading conditions can be observed before failure.

The fracture surfaces for test 1 and test 3 have been shown in Figure 48. The observation common to both the fracture surface is it being uneven at the top and flat at the bottom. The uneven top surface is indicative of a tortuous crack path. Therefore, a little bit of plasticity cannot be ruled out during fatigue failure of Al/SiC nanolaminates. Crack deflection at the interface and presence of a number of stress-concentration sites can play a contribution in fracture surface being non-planar. It is also interesting to note that this uneven surface is not present near column of pores. These columnar boundaries apart from housing pores also have small radius of curvatures, therefore they are the weak links in the microstructure. They assist in instantaneous propagation of cracks and have been shown through red arrows in the image. Once the crack has covered the major part of the beam cross-section, the load bearing capacity of the beam drastically reduces leading to a relatively planar surface at the bottom of the beam.

Another interesting observation is the formation of vertical lines giving a grain like appearance to amorphous SiC layers. They can be correlated to the river markings observed in brittle fracture surface for bulk materials (Hull 1996). In the case of nanolaminates, the interface and Al layers interrupt the SiC layers. The river markings don’t get a chance to grow continuously therefore, this pattern is less obvious as compared to bulk materials. However, in a single SiC layer several instances of cracks branching out were observed as pointed by the arrows.

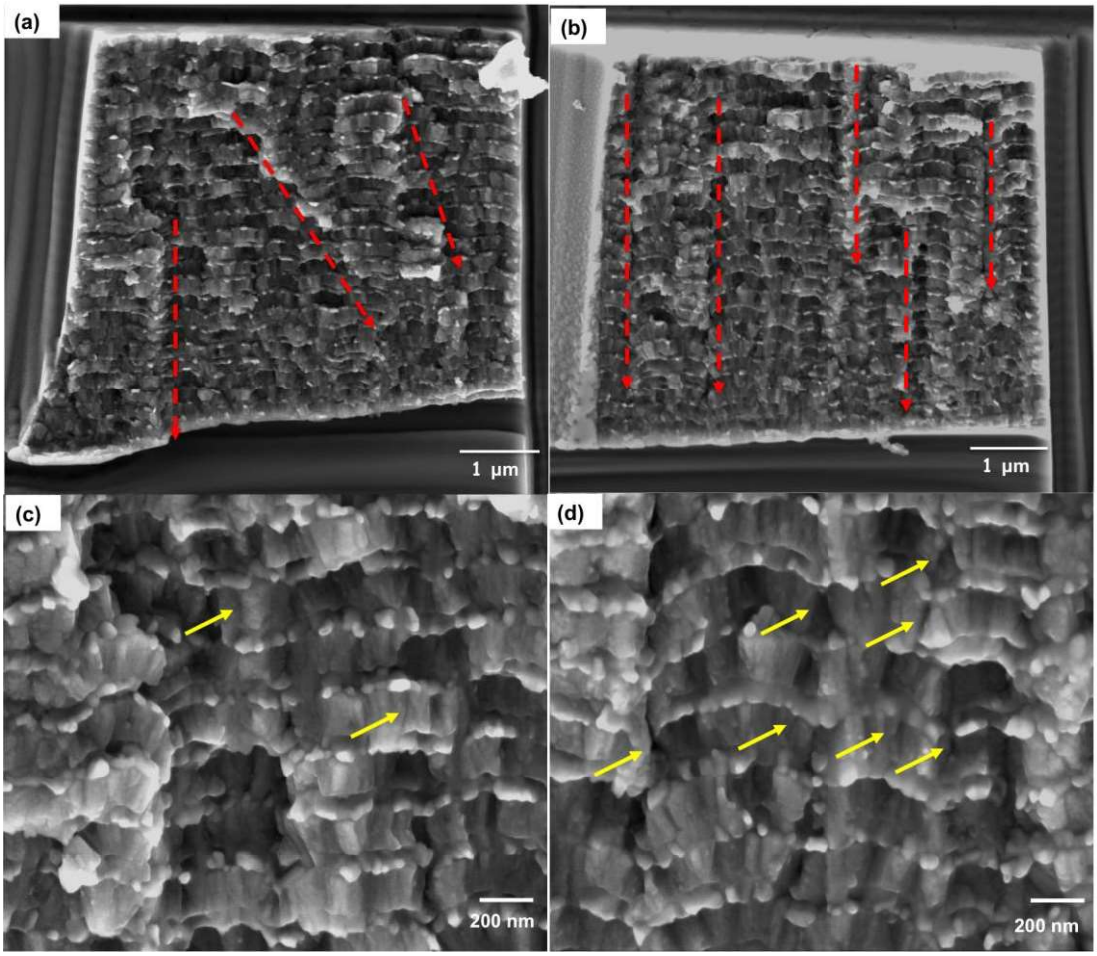

Figure 48: Fracture surface of beam subjected to a maximum stress of (a,c) 888 MPa and (b,d) 795 MPa. Yellow arrows point towards river marks on SiC surface, characteristic of a brittle failure.

In ductile and brittle materials, crack growth is assisted by intrinsic mechanisms and delayed by extrinsic mechanisms (Ritchie 1999). Intrinsic mechanisms lead to nucleation of micro voids or cracks and are based on specific properties of materials (Ritchie 1999). On the other hand extrinsic mechanisms refer to wedging or bridging of crack surface, inelastic zone surrounding the crack etc. which leads to toughening of the material (Ritchie 1999). Since these mechanisms operate after the initiation of crack they

have a dependence on the length and morphology of crack itself. However, in brittle materials the toughening process relies heavily on extrinsic mechanisms, which make an attempt to locally reduce stress intensity near the tip. In Al/SiC nanolaminates columnar boundaries act as regions of localized stress-concentration whereas interface assists in crack deflection as observed from the fracture surface. However, the effect of these localized regions of stress-concentration together with the channel of pores is much more than crack deflection at interface leading to an overall brittle response in nanolaminates.

5.4 Summary

In situ fatigue tests were performed on FIB milled microcantilever beams of Al/SiC nanolaminates. The experimentally obtained fatigue life curve had a clear fatigue run-out point at 786 MPa, higher than that of bulk SiC at 110 MPa. Moreover, the nature of the curve was different from bulk Al, which has a sloping curve without a marked run-out point. Despite the presence of 25 bilayers and interfaces the overall fracture was brittle. A steep drop in stiffness was observed towards the very end of fatigue life. This is indicative of microcrack and microvoid growth. Finally, the beam fractured and had a tortuous crack path ultimately leading to its failure. It was interesting to see the channel of pores on the fracture surface that assisted in crack propagation. Crack deflection at the interface was also observed. One of the most interesting features was presence of river marks on the surface of SiC. They were interrupted by Al layer and hence were not as obvious as for the case of bulk materials.

CHAPTER 6

MICROSTRUCTURE AND MECHANICAL PROPERTIES OF CO-SPUTTERED AL-SIC COMPOSITES

6.1 Introduction

Metal-ceramic nanolaminates have been at the center of a lot of work as they offer a combination of high ductility of metallic layers with the strength and stiffness of ceramic layers (Mayer et al. 2015; C. Mayer et al. 2016; Lotfian et al. 2014; Bhattacharyya et al. 2011; Chou et al. 1992; McAdams et al. 1992). These nanolaminates have very high Young's modulus and hardness due to a combined effect of nanocrystalline metallic layers, stiff ceramic layers, strong interface and imposed constraint (C. Mayer et al. 2016; Lotfian et al. 2012; Yang et al. 2016). However, several studies have reported negligible or no change in their mechanical properties with change in volume fraction or layer thickness. The flow strength of Al/Si_3N_4 nanolaminates was controlled primarily by the metallic layers and had values similar to metal-metal nanolaminates (Wang et al. 2015). The hardness of Cu/TiN nanolaminates increased by less than 1 GPa, even after the bilayer thickness was reduced from 200 nm to 4 nm (Pathak et al. 2015). Similarly, the hardness of Al/SiC nanolaminates remained unaffected by layer thickness for a constant volume fraction of aluminum (Lotfian et al. 2014).

Moreover, when micropillar compression studies were performed on Cu/TiN, Al/SiC and Al/Al_3Sc systems, failure occurred at limited plastic strains of ~10% (Bhattacharyya et al. 2011; C. R. Mayer et al. 2016; Han et al. 2009). Deformation occurs

through constrained plastic flow of metallic layer, accompanied by elastic deformation of ceramic layer. The constraint imposed by stiff ceramic layers leads to strain hardening in these micropillars (Lotfian et al. 2013). However, it also limits their ductility by increasing tensile stresses on ceramic layers (Wang & Misra 2014). Plastic co-deformation of layers is achieved only at extremely small ceramic layer thickness ~ 5 nm, as was seen for Al/TiN (Mook et al. 2013; Li et al. 2015). Metal/ceramic nanolaminates also have low fracture toughness. Fe/VC multilayers had a fracture toughness ~2 MPa√m even at 0.8 volume fraction of Fe (Wang et al. 2016). Al/SiC nanolaminates also reported similar low fracture toughness at 100 nm layer thickness, indicating limited resistance to crack propagation in these multilayered systems (Mayer 2016). Therefore, it can be argued that there is still a lot of scope towards full utilization of metal-ceramic combination in the multilayered form.

Additional challenges associated with this system include its columnar growth mechanism. This leads to a wavy microstructure resulting in formation of columnar boundaries and pores. They form the weak points in the microstructure and act as sites of crack initiation and propagation, thus, further limiting the plasticity of nanolaminates (C. R. Mayer et al. 2016). In addition, due to a large mismatch in their stiffness, metal-ceramic nanolaminates also exhibit significant anisotropy in their mechanical properties (C. R. Mayer et al. 2016; C. Mayer et al. 2016). When micropillar compression was performed parallel to the layers of Al/SiC nanolaminates, SiC layers buckled and kink bands were formed leading to failure of miropillar (C. R. Mayer et al. 2016). Similar behavior was seen for nanoindentation loading parallel to the layers and buckling of SiC

layers was reported to occur prematurely due to wavy microstructure (C. Mayer et al. 2016).

Over the last decade, a lot of work has been done towards understanding the structure-property relationships of nanolaminates. In metal-ceramic nanolaminates, it is still a challenge to find the right balance between strength and ductility, mainly because the constituents have extremely different elastic moduli. This work is a step forward towards addressing this limitation and attempts at creating a new generation of nanocomposite materials through development of co-sputtered Al-SiC films. Here, Al and SiC are deposited in one layer and the microstructure can be tailored at scales near to those of individual atoms or molecules. These co-sputtered monolayers can be used with metal or ceramic layers to form multilayered composites or graded microstructures containing different atomic ratios of aluminum and silicon carbide in different layers.

To date, co-sputtered monolayers have been used for developing thin films for various applications. They cover a broad spectrum of constituents from metallic glasses to diamond like carbon (DLC) coatings (Escudeiro et al. 2015; Apreutesei et al. 2014; Pei et al. 2005). For thin film metallic glasses, numerous Zr-based, Zr-Cu-based and Pd-based alloys have been developed (Schuster et al. 2008; Chou et al. 2010; Ye et al. 2012; Chou et al. 2011). Bulk metallic glasses reported high hardness, wear resistance and elastic modulus. However, in most cases, they lack in tensile ductility due to limited provision for strain hardening (Greer 2009). On the other hand, diamond like carbon coatings have high compressive stresses which act as a barrier for good adhesion with the substrate and are responsible for their brittle behavior (Pei et al. 2005). A number of

metal-ceramic co-sputtered layers have also been developed but most of these studies have been motivated towards developing super-hard or super-tough thin films (Musil et al. 2002; Ulrich et al. 1997; Procházka et al. 2004; Veprek et al. 2000; Zhang et al. 2005). A majority of this work has concentrated on achieving extremely high hardness while retaining the toughness through addition of ductile phase (Musil et al. 2001; Mišina et al. 1998), nanograin structure design (Veprek et al. 2000; Procházka et al. 2004), phase transformation induced toughening (Ji et al. 2001) etc. To the best of the author's knowledge, co-sputtered Al-SiC monolayers have not yet been developed.

In this work, for the first time Al and SiC co-sputtered layers have been created and studied. Four different compositions ranging from 17 at. % of Al to 58 at. % of Al were designed. The samples exhibited a wide range of hardness and modulus values from 6 GPa to 18 GPa and 140 GPa to 220 GPa respectively depending on their respective composition. Extensive microstructural characterization was done through Energy Dispersive X-ray Spectroscopy (EDS), Selected Area Diffraction Pattern (SADP), HRTEM imaging and XPS to understand the microstructural changes at the atomic level. Mechanical property of the co-sputtered samples was correlated with change in composition as well as atomic packing density of the microstructure.

6.2 Materials and Experimental Procedure

The Al–SiC co-sputtered samples were fabricated using magnetron sputtering on a Si (100) substrate. The targets used were pure Al (99.99%) and SiC (99.5%) (Kurt J. Lesker, Clarion, PA). An Ar working pressure of 3 mTorr was maintained during the deposition process. Four different target power combinations were used to obtain different atomic

ratios between Al and Si. With the change in target power, a change in the deposition rate was achieved, and as a result, a controlled change in the atomic ratios between Al and SiC.

The thickness of the sample was measured through focused ion beam (FIB) cross-sections (Figure 49). A trench was milled using a milling current of 1 nA followed by final polishing at 120 pA. All the samples were approximately 1 μm thick and had a smooth cross-section indicating a homogenous microstructure throughout the thickness.

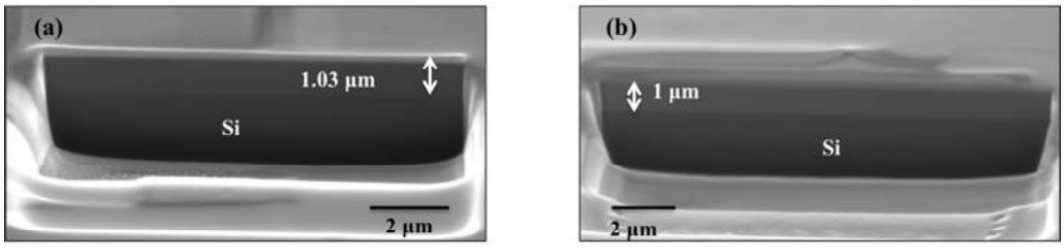

Figure 49: FIB cross-section showing the thickness of co-sputtered layer deposited on the Si substrate for samples having different atomic ratios between Al and SiC.

Samples for characterization by TEM were prepared using a FIB lift-out procedure as explained elsewhere (Lekstrom et al. 2008). An aberration-corrected FEI 80-300 Titan^{TM} operated at 300 kV was used for investigating the microstructure at atomic level. SADP, EDS and HRTEM imaging were performed to investigate into the morphology, elemental composition, and structural changes in the co-sputtered films. SADP of the films was used to obtain coherent diffraction intensities (CDIs) for comparing the sample microstructure with that of Al, Si and SiC.

To investigate the chemical bonding configurations between Al, Si, and C, XPS

was performed using a commercial equipment (VG ESCA-LAB 220i-XL, USA). Monochromated Al-Kα (1486.5 eV) X-ray radiation was used for the measurements. Survey spectra as well as individual high-resolution spectra for Al 2p and Si 2p peaks were recorded to get insight into the bonding between the constituents. Peak fittings were done using CasaXPS software and the background contribution was estimated by the Shirley method (Shirley 1972).

Micromechanical properties of the co-sputtered samples were measured by nanoindentation using a commercial nanoindenter (Nanoindenter XP-II, Agilent, USA). Samples were mounted on an Al stub using a crystal bond and indentation was carried out on at least 20 different locations in the sample. The modulus and hardness measurements were done with respect to indentation depth using the continuous stiffness measurement (CSM) technique by superimposing a harmonic load of small amplitude (Li & Bhushan 2002a). Before indenting the specimens, the calibration was done by measuring Young's modulus and hardness of a standard silica sample.

6.3 Results and Discussion

Four samples were synthesized with increasing SiC content through magnetron sputtering by changing the relative power of Al and SiC targets. The resultant microstructure was studied through HRTEM imaging and elemental composition of the samples was obtained through EDS. The microstructure of all the samples was amorphous as indicated by blurred concentric rings in their SADPs. Therefore, to gain insight about the short-range order of atoms in the microstructure, the CDIs were compared with the diffraction data of Al, Si and SiC. Finally, the binding energies obtained from XPS helped in

quantification of the SiC content present in the samples. The increase in modulus and hardness values from nanoindentation was correlated with their compositional and microstructural changes.

6.3.1 Microstructural Characterization of Co-sputtered samples

Elemental compositions obtained from the EDS spectra of four samples are shown in Table 4 and the corresponding HRTEM images have been shown in Figure 50. The atomic concentration of Al decreased from 58 at. % for Sample1 to 17 at. % for Sample4. This is due to a decrease in deposition rate associated with the decrease in target power from 100 watts to 33 watts. Similarly, an increase in the atomic concentration of Si is due to an increase in target power from 165 watts to 325 watts. It can be noted from the table that even though a SiC target was used for deposition, 1:1 ratio is not achieved between atomic percentage of Si and C in the microstructure. Al, Si and C have different yield, bond dissociation energy and cohesive energy, and therefore they have different sputtering rates (Maissel et al. 1970; C. & Kittel 2004; Lide 2008). Therefore, apart from SiC, Si and C are also expected to be present in elemental form in the microstructure.

These co-sputtered samples had an amorphous microstructure as shown by their acquired SADPs in Figure 51. In previous work done on sputtered Al/SiC nanolaminates, Al is reported to form a nanocrystalline structure with a strong (111) peak (Xin Deng et al. 2005). However, in the co-sputtered condition, even the sample containing 58 at. % of Al is amorphous.

Sample	Al Target Power (watts)	SiC Target Power (watts)	Al at. %	Si at. %	C at. %
Sample1	100	165	58 ± 3	19 ± 2	23 ± 3
Sample2	100	325	37 ± 2	26 ± 3	37 ± 2
Sample3	50	325	30 ± 4	31 ± 3	39 ± 3
Sample4	33	325	17 ± 3	38 ± 4	45 ± 3

Table 4: Deposition parameters and atomic compositions of Al-SiC co-sputtered samples obtained from the EDS spectra.

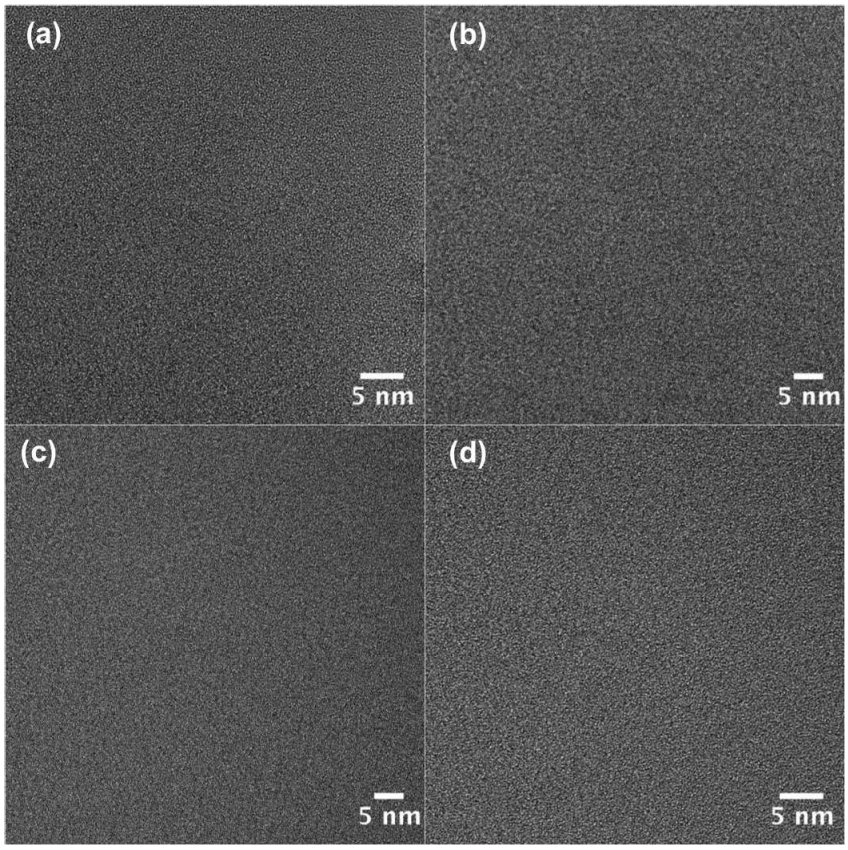

Figure 50: HRTEM image of (a) Sample1, (b) Sample2, (c) Sample3 and (d) Sample4. Random arrangement of atoms confirms the presence of amorphous microstructure.

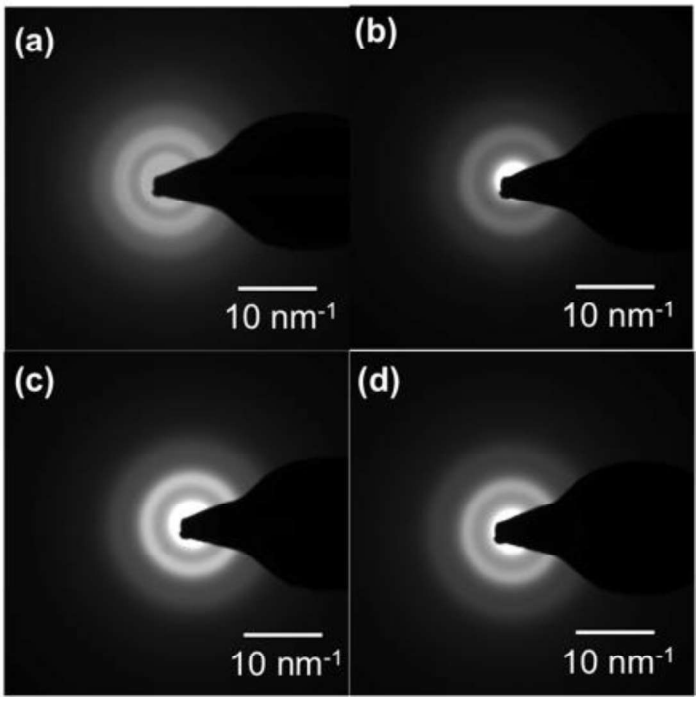

Figure 51: SADP of (a) Sample1, (b) Sample2, (c) Sample3 and (d) Sample4. Microstructure was amorphous as shown by the blurred concentric rings.

To get more information about the order of atoms in the microstructure, the diffraction patterns were converted into one-dimensional CDIs. This was done through rotational integration of pixel values. The initial values are not taken into account due to hindrance from the beam-stopper, which varied for different samples. These acquired CDIs are shown in the Figure 52 and have been compared to diffraction intensities of Al, Si and SiC, generated from the atomic structure using international center for diffraction data, PDF4 card number (Al:00-004-0787, Si: 00-026-1481 and SiC: 00-022-1273). Two broad peaks were seen for Sample1, first peak can be associated with the peak positions of Al and second peak with that of Si (as marked by dashed blue lines). It can be, therefore, concluded that elemental Al and Si constitute majority of the microstructure.

For Sample2, a shift in the position of first peak can be observed. This is indicative of change in the microstructure and since the shifted peak better fitted with SiC, an increase in SiC content is expected for this sample. Moreover, the second peak for this sample does not match with the elemental Si peak position suggesting a decrease in its at. % in the microstructure. Therefore, with an increase in the Si atomic percentage from 19 % in the first sample to 26 % in the second sample, peak shifts indicated an increase in SiC content. These differences are a combined effect of an increase in atomic percentage of Si, decrease in aluminum content and an increase in SiC target power from 165 watts to 325 watts. Changes in target power alters the kinetic energy of ejected atoms and hence, plays an important role in governing the resultant composition and bond formation in the deposited layer (Wasa et al. 1976).

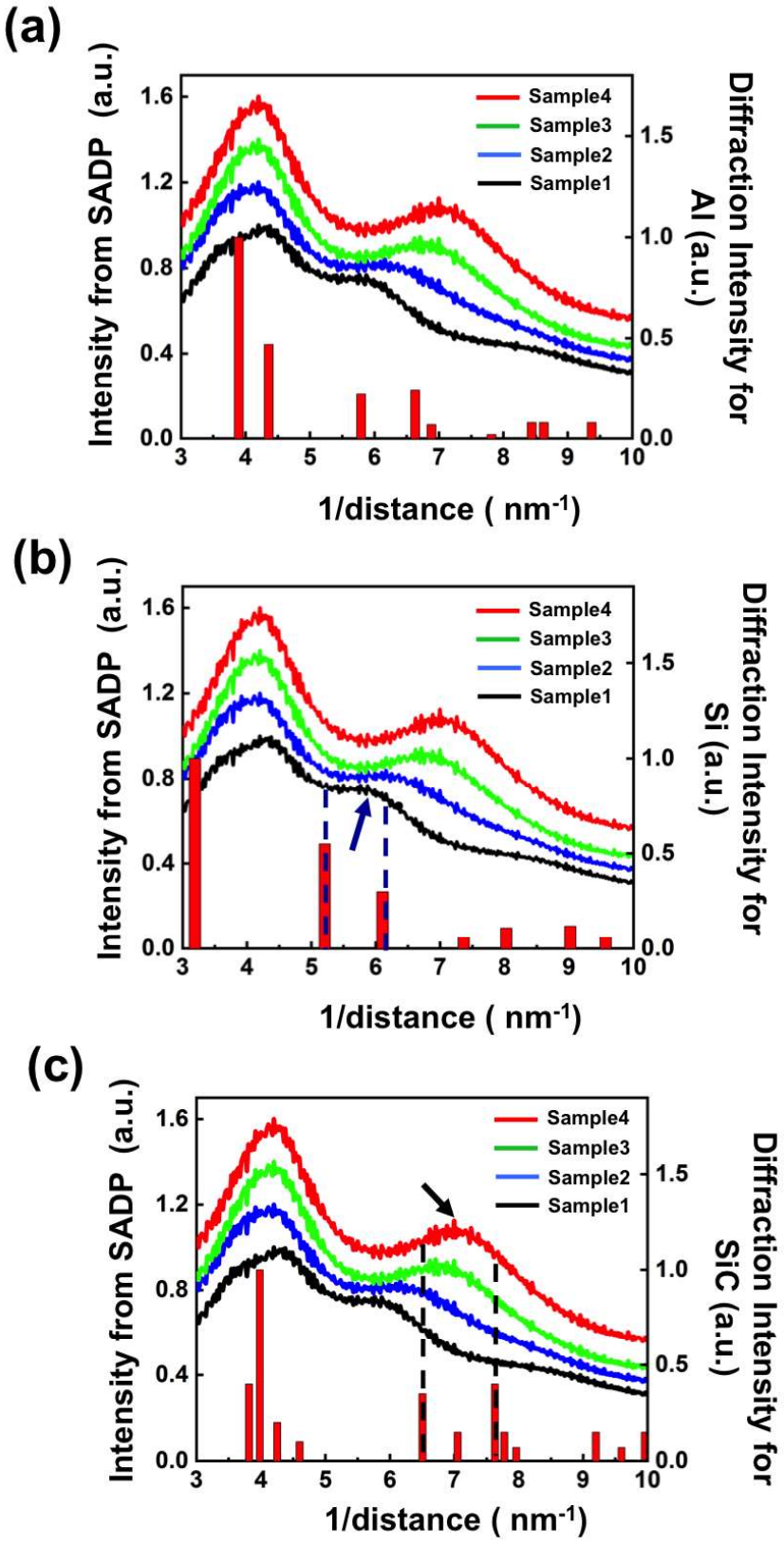
(a)
Intensity from SADP (a.u.)
Diffraction Intensity for Al (a.u.)
Sample4
Sample3
Sample2
Sample1
1/distance (nm-1)
(b)
Intensity from SADP (a.u.)
Diffraction Intensity for Si (a.u.)
Sample4
Sample3
Sample2
Sample1
1/distance (nm-1)
(c)
Intensity from SADP (a.u.)
Diffraction Intensity for SiC (a.u.)
Sample4
Sample3
Sample2
Sample1
1/distance (nm-1)

Figure 52: CDIs of co-sputtered samples with the electron diffraction intensities of (a) Al, (b) Si and (c) SiC. The peak shifts suggest an increase in SiC content.

For Sample3 and Sample4, further shifts in the second peak position were observed. The shifted peaks better fitted with SiC peak positions, clearly indicating an increase in its content in the microstructure. In summary, the CDI of first sample matches with elemental Si; however, with an increase in Si atomic percentage, better fit is seen between the acquired CDI and SiC indicating its increase in the microstructure. It should be noted that though this technique is a good qualitative method to get an understanding of the short-range order of atoms in an amorphous microstructure, it is not solely enough to ascertain the composition of the samples.

In order to further elucidate into the microstructure of co-sputtered films, a deeper analysis was conducted of the acquired HRTEM images. In Figure 50, HRTEM micrographs of films with different Al contents are shown. The films have an overall amorphous microstructure as was expected from the SADPs. However, for the Sample1, nanocrystalline aggregates, 2 nm to 4 nm in width could be observed dispersed in the amorphous matrix, Figure 53. The nanocrystalline aggregates have been encircled and a magnified image of the corresponding regions have been shown. The crystalline nature of these nanodomains was confirmed through bright spots that appeared in their respective Fast Fourier Transform (FFTs), as shown in the figure. The lattice spacing (d) values were calculated from FFTs of a number of acquired images. Two sets of spacing values were obtained d_1 = 0.233 nm ± 0.003 nm and d_2 = 0.203 ± 0.0005 nm. These values correspond to the family of {111} and {200} planes of Al respectively. Moreover, in

some cases, the FFTs revealed the presence of two sets of planes, the calculated angle between planes having spacing of 0.233 nm was 70.4°, which matches with the theoretical angle between {111} planes. The second calculated angle, 55°, was between planes having calculated spacing of 0.233 nm and 0.203 nm which matched with the theoretical angle between family of {111} and {200} planes. One such example can be observed in the last nanodomain of Figure 53, encircled in green color.

There are other compounds of Al, Si and C, which have lattice spacing similar to the calculated values such as Al_9Si, Si_5C_3 etc. However, none of these compounds report both the calculated spacing. Only aluminum meets all the requirements of experimentally obtained lattice spacing and angles between the planes. Therefore, it can be concluded that the nanodomains are constituted of elemental aluminum. A clear difference in the microstructure can be seen with the decrease in atomic percentage of Al. Nanodomains were not present in Sample2, Sample3 and Sample4. This strongly supports the above conclusion that nanodomains are comprised of elemental aluminum and hence, with the reduction in its content, they are no longer visible. From the point of view of mechanical behavior, the width of these aggregates as well as the distance between them plays an important role. The distance between the aggregates also known as the matrix width separation (s), is calculated by the nearest distance between the edges of two spheres along a face diagonal. This value will be discussed in greater detail in a later section.

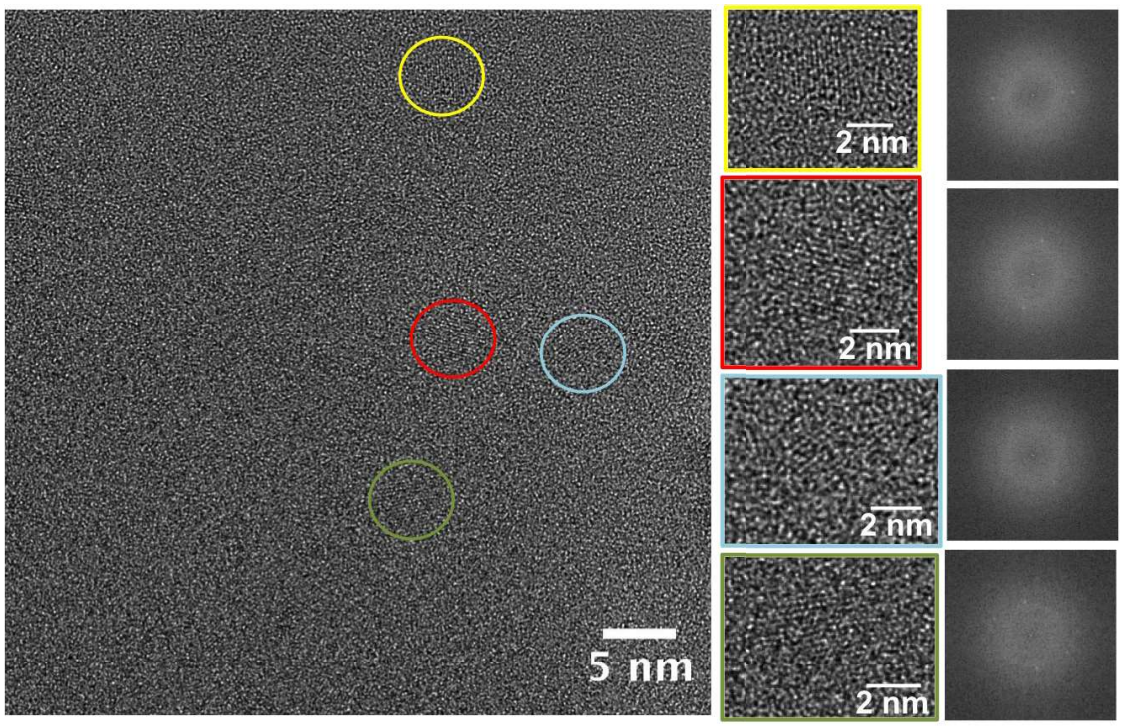

Figure 53: HRTEM image of Sample1. Encircled regions contain nanocrystalline aggregates of Al. The corresponding magnified images highlighting these nanodomains have been shown. Bright spots can be seen in FFTs, which confirm the presence of lattice planes for these nanocrystalline aggregates.

A MATLAB code was written for detecting these nanodomains. The image was divided into square grids of 3 nm x 3 nm and FFTs were obtained for each of these grids individually. Finally, only these regions of the image were selected where a detectable pattern was present as shown by yellow arrows in Figure 54.

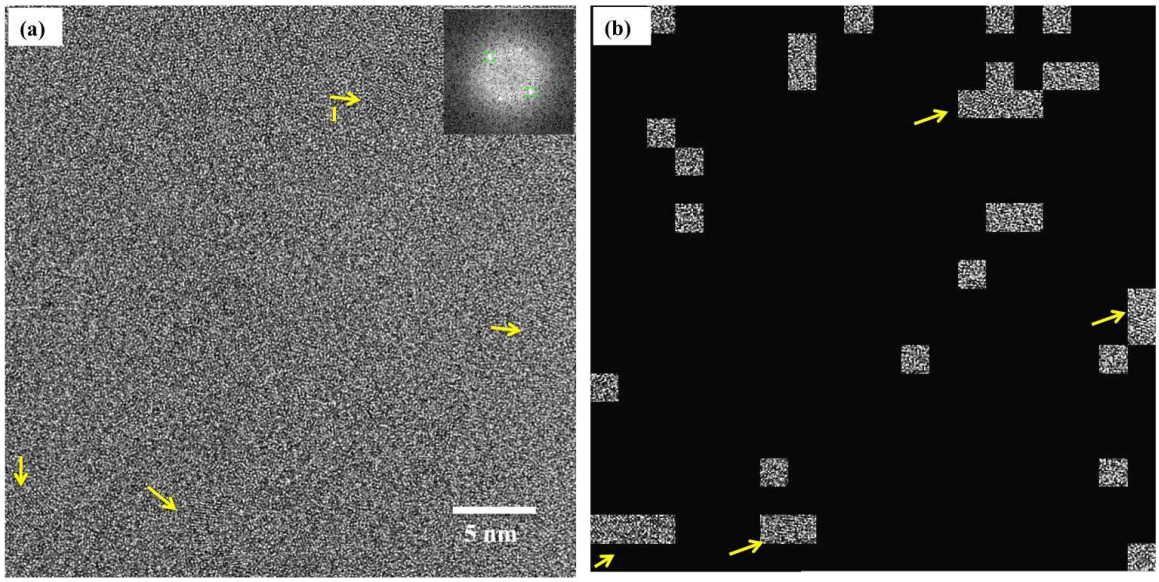

Figure 54 (a) HRTEM image of Sample1, inset contains FFT of region 1 (b) Regions containing nanocrystalline as detected by the MATLAB code. These regions were generated based on the FFT of their individual cell.

To quantify the amount of SiC, Si, C and Al present in the microstructure, XPS was performed on the as-received samples. As mentioned above, a 1:1 ratio is not achieved between Si and C, despite deposition being carried out using SiC target. Therefore, the microstructure is expected to be a combination of Al, Si, C and SiC. Figure 55(a) shows the wide-scan XPS spectrum obtained from the surface of Sample1. A high content of oxygen was detected due to surface contamination. Ar^+ ion bombardment etching was performed to remove these contaminants and obtain a spectrum representative of the bulk microstructure. The wide scan obtained after etching, Figure 55(b) shows a reduction in oxygen peak. Apart from the expected Si 2s, Si 2p, C 1s, Al 2s, Al 2p peaks, Ar peaks (2s and 2p) are also present. This is due to the implanted Ar^+ ions during etching and was not taken in consideration during compositional

analysis.

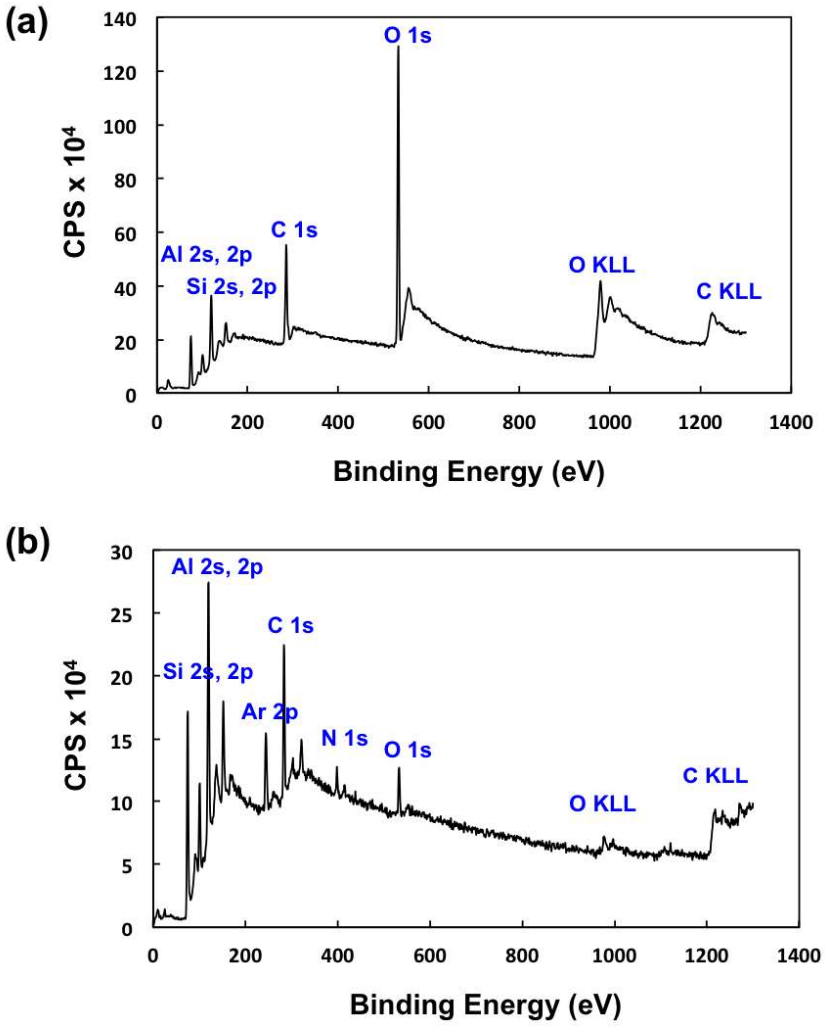

Figure 55: XPS wide-scan for Sample1 (a) as-received sample surface (b) after Ar^+ ion bombardment etching. The first plot shows very high oxygen content due to surface contamination, this is significantly reduced after etching.

High resolution scans of the Al 2p and Si 2p peaks are shown in Figure 56. Differential charging was corrected for by the Al 2p peaks and they are centered on binding energy of 72.8 eV. The asymmetry in shape stems from the closely spaced spin

orbit components of Al $2p_{1/2}$ and Al $2p_{3/2}$.

The Si 2p peaks were away from the binding energy position of 99.8 eV observed for elemental Si (Since & The 1992). Therefore, XPS characterization helped in confirming the results from SADP. Si was present in the microstructure in elemental form as well as SiC. The experimentally obtained peak was fitted with the Si and SiC peak positions to quantify their individual amounts in the samples. A strong peak for Si was seen at 99.8 eV and for SiC at 100.7 eV (Todi et al. 2006). The areas under the corresponding peaks along with the EDS data were used to quantify the amount of Si and SiC present in the sample, as shown in *Table 5*. The samples have been named as Al-x%SiC where x denotes the atomic percentage of SiC.

For Sample1, elemental Si (approximately 70 %) was present in a much higher amount than SiC (~ 30 %). This was also observed in the CDI, which matched very well with the peaks of Si. For the other samples, a higher content of SiC (~ 80 %) is present, which is also confirmed from the peak behavior of their CDIs. As expected, with an increase in Si content, an increase in SiC content was observed for the samples. Though the author understands that quantification from XPS does not yield accurate absolute compositions, it is useful to look at the relative change in amount of SiC in the co-sputtered samples.

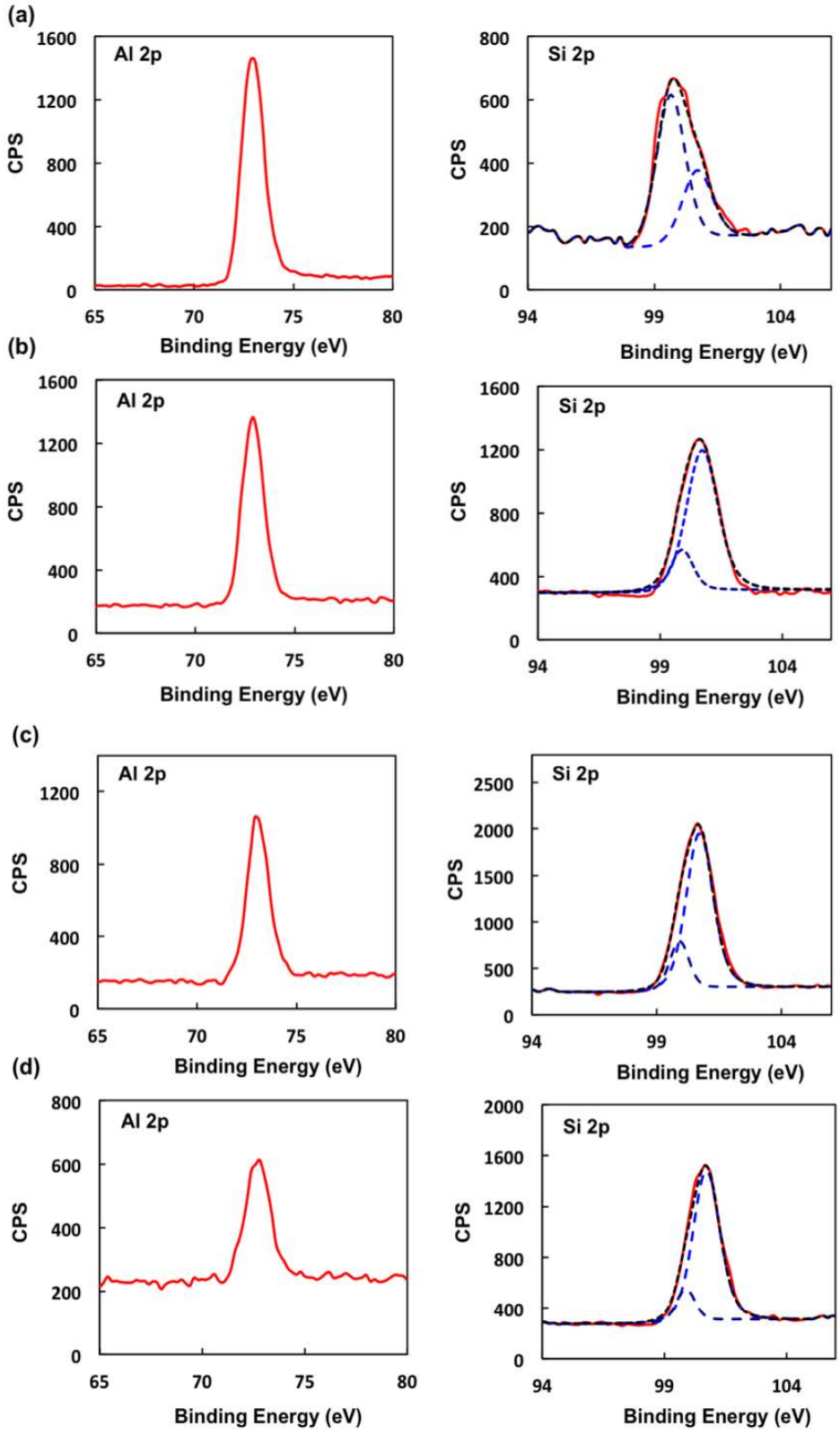
(a)
Al 2p
CPS
Binding Energy (eV)
Si 2p
CPS
Binding Energy (eV)
(b)
Al 2p
CPS
Binding Energy (eV)
Si 2p
CPS
Binding Energy (eV)
(c)
Al 2p
CPS
Binding Energy (eV)
Si 2p
CPS
Binding Energy (eV)
(d)
Al 2p
CPS
Binding Energy (eV)
Si 2p
CPS
Binding Energy (eV)

Figure 56: XPS high resolution scans for Al 2p and Si 2p peak positions of (a) Sample1, (b) Sample2, (c) Sample3 and (d) Sample4. The red curve is experimentally obtained and the blue dashed lines correspond to the fitted curves in Casaxps.

Sample	Al at. %	SiC at. %	Si at. %	C at. %
Al-6%SiC	62	6	14	18
Al-27%SiC	47	27	6	20
Al-34%SiC	40	34	8	18
Al-49%SiC	25	49	8	18

Table 5: Composition of the co-sputtered samples with quantification of SiC from XPS analysis.

6.3.2 Mechanical Properties of Co-sputtered samples

The representative modulus and hardness curves with respect to indentation depth have been shown in Figure 57 and Figure 58 respectively. The substrate effect is clearly visible from the converging modulus curves. Si has a modulus of 120 GPa and therefore the curves for samples Al-6%SiC and Al-27%SiC show an increase in modulus whereas the curves for samples Al-34%SiC and Al-49%SiC show a decrease in modulus, due to an increased contribution from the underlying Si substrate. Measurements for depths below 120 nm were used for calculating the modulus and hardness of the samples.

As expected, significant increase in the hardness and modulus values with an increase in the stiffer SiC content was reported. While the overall microstructure appears to be amorphous for the samples containing 27, 34 and 49 at. % of SiC, a clear right shift

in amorphous humps of CDIs can be observed, Figure 52. These shifts indicate a change in the atomic packing through decrease in bond length. Since the modulus and hardness values are governed by the atomic bonding and packing state it can be understood that the coherent increase in their values is also arising as a result of denser packing state being achieved by increasing the amount of SiC content (Coddet et al. 2012; Chou et al. 2010).

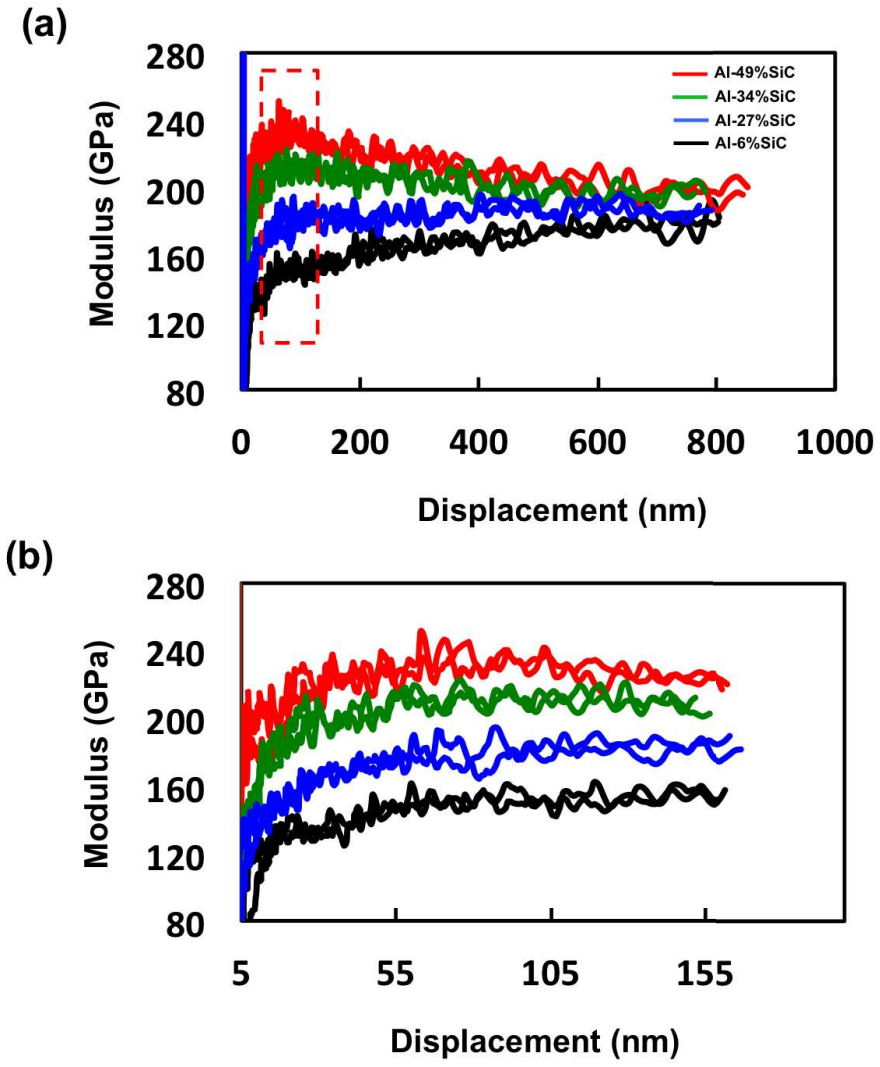

Figure 57: Modulus versus Displacement curves for co-sputtered samples obtained from nanoindentation. 55 – 120 nm was the displacement range used for calculation. An

increase in the modulus value can be seen with an increase in SiC at. %

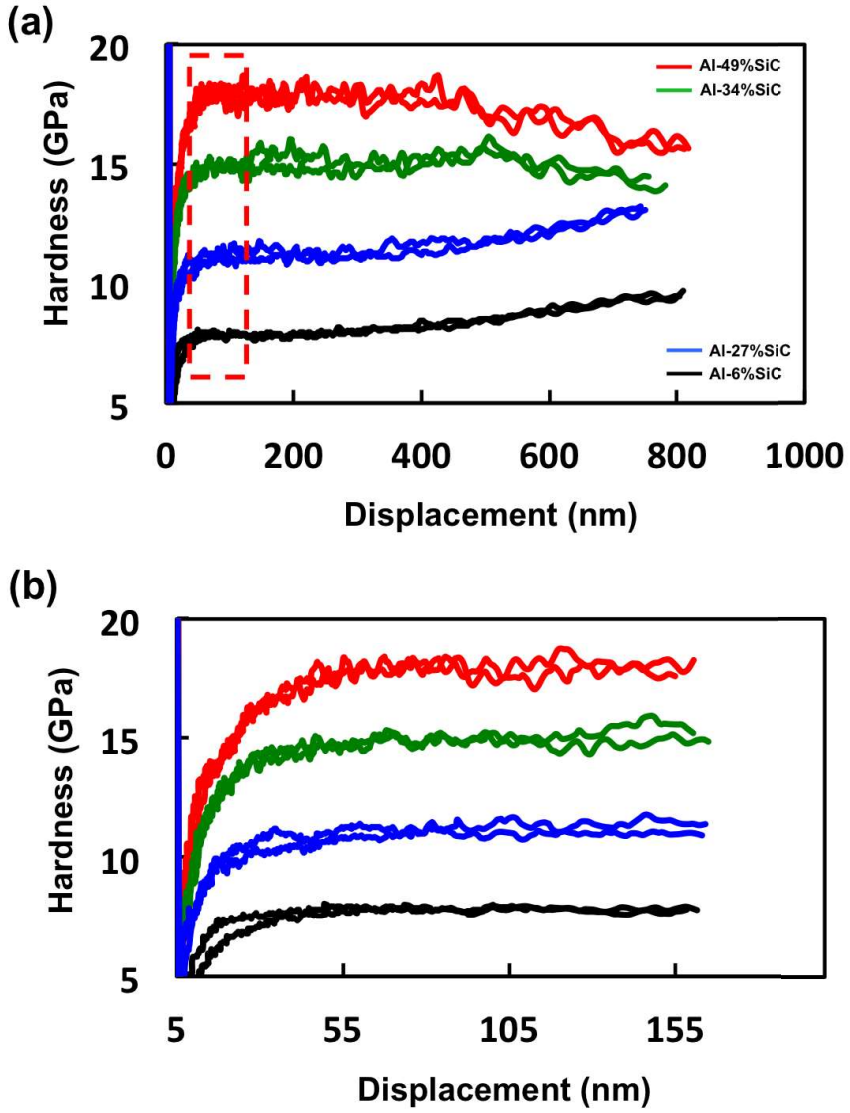

Figure 58: Hardness versus Displacement curves for co-sputtered samples obtained from nanoindentation. 55 – 120 nm was the displacement range used for calculation. An increase in the hardness value can be seen with an increase in SiC at. %.

In order to understand the effect of Al nanodomains on the mechanical properties of the sample a deeper understanding of underlying damage mechanisms is required.

Crack nucleation is effectively suppressed in an amorphous microstructure. However, once nucleated, the crack propagates swiftly leading to catastrophic failure. Severe hydrostatic and shear stress field components are generated due to localized defects, which lead to shear localization and aggravated crack propagation (Pei et al. 2005). The introduction of nanodomains in such a matrix can suppress this by delocalization of shear. However, it has been reported that a considerable improvement is only seen when the particle size, d is similar to the distance between the nanodomains (s) (Pei et al. 2005). For Al-6%SiC, the nanocrystalline aggregates have s>>d and the nanodomains are not closely spaced enough to effectively improve the mechanical properties. This is also visible from Figure 59, where the modulus and hardness values follow a very linear trend with the atomic percentage of SiC, irrespective of presence of nanograins in sample Al-6%SiC. Therefore, the increase in hardness and modulus values with an increase in SiC content can be attributed to change in the composition, related properties of the constituent phases and atomic packing density.

For nanocomposite films, it is also interesting to look at the H/E and H^3/E^2 parameters, which give information about the wear resistance and fracture toughness of materials (Leyland & Matthews 2000). Evaluation of H/E is important since a hard material can resist abrasive wear, and a low Young's modulus better matches with the substrate, which is generally metallic and more compliant. Furthermore, with a lower Young's modulus, a better redistribution of the applied load over a larger area is expected, delaying initiation of fracture in the material system. On the other hand, H^3/E^2 parameter is related to the yield strength and is expected to improve the elastic recovery,

and therefore the toughness. In the present case, an increase in the H/E from 0.05 to 0.08 as well as H^3/E^2 from 0.02 GPa to 1.2 GPa are seen with increase in SiC content. This is an interesting result and indicates that the rate of increase of hardness is greater than modulus for these co-sputtered samples. Therefore, with an increase in SiC content, an increase in the hardness as well as fracture toughness of co-sputtered films is achieved. The modulus and hardness values were compared to traditional nanolaminates with constant Al layer thickness and SiC layer thickness of 50 nm, Figure 59.

For nanolaminates a limited increase in hardness value is observed ~ 3 - 4 GPa on changing the volume fraction or layer thickness (Lotfian et al. 2014). Under indentation loading, SiC layers deform elastically and plastic flow of Al layers is constrained by SiC layers (C. Mayer et al. 2016). With Al layer thickness being constant, the yield strength of Al also remains constant (Lotfian et al. 2014). It has also been reported that the modulus and hardness of SiC layers is independent of layer thickness (Yang et al. 2016). Therefore, in nanolaminates even though SiC layer thickness is being increased from 25 nm to 100 nm, a very small increase in hardness value is obtained, which is mainly attributed to an increase in the imposed constraint (Yang et al. 2016; Lotfian et al. 2014). Further, for same volume fraction of Al and SiC, the hardness of nanolaminates does not increase with a decrease in layer thickness as the increase in yield strength of Al is compensated by the decrease in flexural modulus of SiC (Lotfian et al. 2014). Therefore, by changing the layer thickness of constituents alone, it is challenging to obtain a significant increase in the mechanical properties of nanolaminated Al/SiC composites.

Apart from showing limited variation in mechanical properties, the overall

hardness and modulus values of nanolaminates are also very less compared to the co-sputtered samples, as shown in Figure 59. Nanolaminates, unlike the co-sputtered samples have a layered structure with a high number of interfaces, Al layers are nanocrystalline and the overall film thickness is approximately 20 μm. Therefore, it is difficult to quantitatively discuss the contribution of each of these microstructural differences on modulus and hardness. However, one of the major difference is the presence of columnar boundaries in Al/SiC nanolaminates due to nucleation and growth of nanocrystalline Al (C. R. Mayer et al. 2016). These columnar boundaries are the weakest part in the microstructure and provide an easy path for crack initiation and propagation. Studies have shown that suppressing the columnar boundary enhances the mechanical response of the materials (Galvan et al. 2006). HRTEM investigation at the atomic level shows that such columnar boundaries are not present in the co-sputtered Al-SiC films, and therefore, have a definite contribution towards the high modulus and hardness values. The co-sputtered film can, therefore, be a useful ingredient of multilayered nanolaminates. Substituting the Al or SiC layer with co-sputtered layer is a promising avenue to improve the mechanical properties of metal-ceramic nanolayered composites.

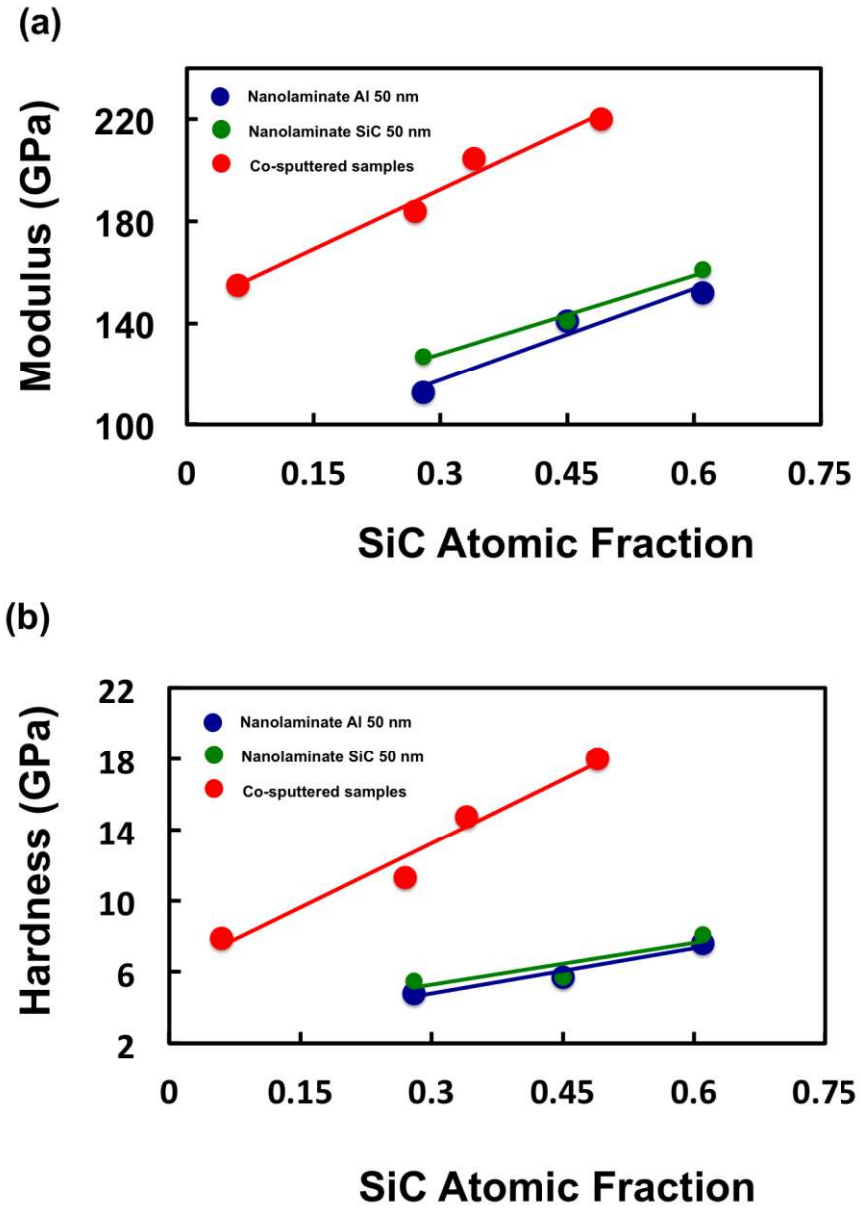

Figure 59: (a) Modulus and (b) Hardness with respect to SiC atomic fraction of Al-SiC co-sputtered samples and Al/SiC nanolaminates. Nanolaminate samples had constant Al layer thickness and SiC layer thickness as shown in Figure (re-plotted from (Yang et al. 2016)). A considerable increase in the modulus and hardness value has been achieved for co-sputtered samples.

6.4 Summary

Co-sputtered Al-SiC monolayers having four different compositions were synthesized using magnetron sputtering. All the samples had an overall amorphous microstructure; sample Al-6%SiC had nanocrystalline aggregates embedded in the amorphous matrix. HRTEM imaging and FFTs at the corresponding locations were used to determine the presence of elemental Al in these nanodomains. A thorough investigation of the lattice spacing and angles between the planes was performed to ensure that other species are not present in these nanodomains. CDIs from SADP and XPS were used to gain insight in the bonding configurations of the atoms. It was concluded that Si is present in the elemental form as well as SiC. The modulus and hardness of the samples increased with an increase in SiC at. %. This increase was expected and was attributed to an increase in the amount of stiffer SiC in these samples and denser atomic packing. Nanocrystalline aggregates present in the sample did not contribute towards significant changes in the mechanical properties. This was due to the large amorphous matrix separating them, which hinders an effective delocalization of shear stress. The modulus and hardness values of co-sputtered samples were higher than traditional nanolaminates. One of the main features that contribute towards this is absence of columnar boundaries in co-sputtered samples that help in crack initiation and propagation.

CHAPTER 7

CONCLUSIONS

7.1 Summary of Research Findings

- *In situ* micropillar compression through lab-based X-ray microscope helped in the 3D rendering of pores present in the microstructure of Al/SiC nanolaminates having layer thickness of 100 nm. These pores are formed due to geometric shadowing during magnetron sputtering. For the first time, the pores present in the microstructure were visualized and quantified in 3D. Further, the images acquired during the interrupted compression revealed shearing as one of the operative damage mechanisms. Moreover, through extensive image analysis the site of damage initiation was correlated with the presence of channel of pores in the microstructure.
- Microscale testing techniques rely heavily on the Ga^+ ion based FIB, whose use has been a matter of concern for material scientists owing to the damage it can cause to the microstructure. In this work, through micropillar compression a comparative study was done on micropillars fabricated from Ga^+ ion and Ne^+ ion sources respectively. Al/SiC nanolaminates having an individual layer thickness of 50 nm was used. It was observed that the strength of micropillars and strain to failure remained unaffected by the sputtering of Ga^+ ions.
- MEMS based tensile tests were performed on Al/SiC nanolaminates having layer thickness of 100 nm and 25 nm under isostrain loading conditions. It was reported

that the tensile strength was independent of individual layer thickness. Under the isostrain condition, SiC layers bear the maximum load. They have an amorphous microstructure and their strength is independent of individual layer thickness.

- The tensile strengths obtained from MEMS based tests were compared to the tensile strengths obtained from FIB milled dog-bone specimens. The FIB milled dog-bone specimens had a lower volume but also lower tensile strengths in comparison to the MEMS based dog-bone samples. This was attributed to a change in the microstructure with respect to distance from the substrate. With an increase in the number of deposited layers, the microstructure becomes wavier and consists of pores. Therefore, the FIB milled dog-bones houses more defects compared to the MEMS based dog-bones, which are close to the substrate and devoid of pores.
- Interrupted *in situ* cyclic loading was performed on Al/SiC nanolaminates having a layer thickness of 100 nm. Fatigue life curve was obtained through cyclic testing of microcantilever beams. The beams failed in a brittle manner and this was depicted in a steep drop in the stiffness plot. From the fracture surface and acquired videos, initial sites of fracture were captured and information about crack growth was obtained. The columnar boundaries and channel of pores assisted in crack propagation leading to immediate failure after the crack initiated at the top of the beam.
- Co-sputtered Al-SiC composites were synthesized with increasing concentration of SiC. The samples had an overall amorphous microstructure. Nanocrystalline Al aggregates were dispersed in the amorphous matrix in the sample containing 58

at. % of Al. With an increase in SiC content a decrease in atomic bond spacing was observed through CDIs. This is indicative of a denser atomic structure and thereby led to higher modulus and hardness values. The co-sputtered samples had higher hardness than that of traditional nanolaminates. A densely packed structure together with the absence of defects such as pores contributed towards an improved mechanical behavior.

7.2 Future Work

Al/SiC nanolaminates exhibit high strength and hardness but limited ductility. A potential avenue of improvement in ductility is through development of layered hybrid microstructures containing alternating metallic and co-sputtered layers. The composition of co-sputtered layers can be altered easily and provides an additional way of tailoring the microstructure to achieve desirable properties. Moreover, by substituting the SiC layer with a co-sputtered layer, the presence of pores in the microstructure can be avoided. Al atoms, after being deposited on the surface, can diffuse and reach the troughs of the microstructure, thereby making it more planar and devoid of pores. This method can be more widely used in other metal-ceramic systems by adding a small atomic percentage of the metallic component in the ceramic layer. Further, due to the low melting point of Al, the strength of Al/SiC nanolaminates reduces drastically with an increase in temperature. Replacing the metallic layer with a co-sputtered layer can help in improving the high temperature mechanical properties of metal/ceramic nanolaminates. Alternatively, this can also be achieved by substituting the Al layer with Ti, which exhibits better high temperature properties.

REFERENCES

Ben Amor, S. et al., 1998. Characterization of zirconia films deposited by r.f. magnetron sputtering. *Materials Science and Engineering: B*, 57(1), pp.28–39.

Anderson, P.M., Foecke, T. & Hazzledine, P.M., 1999. Dislocation-based deformation mechanisms in metallic nanolaminates. *MRS Bulletin*, 24(2), pp.27–33.

Apreutesei, M. et al., 2014. Microstructural, thermal and mechanical behavior of co-sputtered binary Zr-Cu thin film metallic glasses. *Thin Solid Films*, 561, pp.53–59.

Bales, G.S., 1991. Macroscopic model for columnar growth of amorphous films by sputter deposition. *Journal of Vacuum Science & Technology A: Vacuum, Surfaces, and Films*, 9(1), p.145.

Bei, H., Shim, S., George, E.P., et al., 2007. Compressive strengths of molybdenum alloy micro-pillars prepared using a new technique. *Scripta Materialia*, 57(5), pp.397–400.

Bei, H., Shim, S., Miller, M.K., et al., 2007. Effects of focused ion beam milling on the nanomechanical behavior of a molybdenum-alloy single crystal. *Applied Physics Letters*, 91(11).

Bhattacharyya, D. et al., 2011. Compressive flow behavior of Al-TiN multilayers at nanometer scale layer thickness. *Acta Materialia*, 59(10), pp.3804–3816.

Bhattacharyya, D. et al., 2008. Nanoindentation and microstructural studies of Al/TiN multilayers with unequal volume fractions. *Scripta Materialia*, 58(11), pp.981–984.

Bhowmik, A. et al., 2016. Using coupled micropillar compression and micro-Laue diffraction to investigate deformation mechanisms in a complex metallic alloy Al13Co4. *Applied Physics Letters*, 108(11).

Böhringer, K., Jousten, K. & Kalbitzer, S., 1988. Development of a high-brightness gas field-ionization source. *Nuclear Inst. and Methods in Physics Research, B*, 30(3), pp.289–292.

C., K. & Kittel, C., 2004. Introduction to Solid State Physics. *John Wiley and Sons, Inc., New York*, 8th editio, p.704.

Callisti, M. & Polcar, T., 2017. Combined size and texture-dependent deformation and strengthening mechanisms in Zr/Nb nano-multilayers. *Acta Materialia*, 124, pp.247–260.

Carpenter, J.S. et al., 2012. Bulk texture evolution of Cu-Nb nanolamellar composites during accumulative roll bonding. *Acta Materialia*, 60(4), pp.1576–1586.

Cavaliere, P., 2010. Cyclic deformation of ultra-fine and nanocrystalline metals through nanoindentation: Similarities with crack propagation. *Procedia Engineering*, 2(1), pp.213–222.

Chawla, N. et al., 1998. Effect of SiC volume fraction and particle size on the fatigue resistance of a 2080 Al/SiC p composite. *Metallurgical and Materials Transactions A*, 29(11), pp.2843–2854.

Chawla, N. et al., 2008. Indentation mechanics and fracture behavior of metal/ceramic nanolaminate composites. *Journal of Materials Science*, 43(13), pp.4383–4390.

Chawla, N. et al., 2000. The Effect of Matrix Microstructure on the Tensile and Fatigue Behavior of SiC Particle-Reinforced 2080 AI Matrix Composites. *Metallurgical and Materials Transactions Al*, 31(2), pp.531–540.

Chen, Y. et al., 2012. Microstructure and strengthening mechanisms in Cu/Fe multilayers. *Acta Materialia*, 60(18), pp.6312–6321.

Chou, H.S. et al., 2011. Enhanced mechanical properties of multilayered micropillars of amorphous ZrCuTi and nanocrystalline Ta layers. *Intermetallics*, 19(7), pp.1047–1051.

Chou, H.S., Huang, J.C. & Chang, L.W., 2010. Mechanical properties of ZrCuTi thin film metallic glass with high content of immiscible tantalum. *Surface and Coatings Technology*, 205(2), pp.587–590.

Chou, T.C. et al., 1992. Mechanical properties and microstructures of metal/ceramic microlaminates. Part I. Nb/$MoSi_2$ systems. *Journal of Materials Research*, 7(10), pp.2765–2773.

Chu, X. & Barnett, S.A., 1995. Model of superlattice yield stress and hardness enhancements. *Journal of Applied Physics*, 77(9), pp.4403–4411.

Coddet, P. et al., 2012. On the elastic modulus and hardness of co-sputtered Zr-Cu-(N) thin metal glass films. *Surface and Coatings Technology*, 206(17), pp.3567–3571.

Cordes, N.L., 2014. Spectrochimica Acta Part B : Atomic Non-destructive elemental quantification of polymer-embedded thin films using laboratory based X-ray techniques.

Dao, M. et al., 2006. Strength, strain-rate sensitivity and ductility of copper with nanoscale twins. *Acta Materialia*, 54(20), pp.5421–5432.

Deng, X. et al., 2005. Mechanical behavior of multilayered nanoscale metal-ceramic composites. *Advanced Engineering Materials*, 7(12), pp.1099–1108.

Deng, X. et al., 2005. Nanoindentation Behavior of Nanolayered Metal-Ceramic Composites. *Journal of Materials Engineering and Performance*, 14(August), pp.417–423.

Dieter, G.E. et al., 1988. *Mechanical Metallurgy*.

Economou, N.P., Notte, J.A. & Thompson, W.B., 2012. The history and development of the helium ion microscope. *Scanning*, 34(2), pp.83–89.

El-Awady, J. et al., 2009. Effects of focused ion beam induced damage on the plasticity

of micropillars. *Physical Review B*, 80, pp.1–5.

Elswick, D. et al., 2013. Advanced Nanofabrication using Helium, Neon and Gallium Ion Beams in the Carl Zeiss Orion NanoFab Microscope. *Microscopy and Microanalysis*, 19(S2), pp.1304–1305.

Epting, W.K., Gelb, J. & Litster, S., 2012. Resolving the three-dimensional microstructure of polymer electrolyte fuel cell electrodes using nanometer-scale X-ray computed tomography. *Advanced Functional Materials*, 22(3), pp.555–560.

Escudeiro, A. et al., 2015. Structural and mechanical properties of nanocrystalline Zr co-sputtered a-C(:H) amorphous films. *Applied Surface Science*, 325(C), pp.64–72.

Fortunato, E. et al., 2008. Highly stable transparent and conducting gallium-doped zinc oxide thin films for photovoltaic applications. *Solar Energy Materials and Solar Cells*, 92(12), pp.1605–1610.

Frei, H. & Grathwohl, G., 1989. Development of a piezotranslator-based bending device for in situ SEM investigations of high performance ceramics. *Journal of Physics E: Scientific Instruments*, 22(8), pp.589–593.

Freyman, C.A. & Chung, Y.W., 2008. Synthesis and characterization of hardness-enhanced multilayer oxide films for high-temperature applications. *Surface and Coatings Technology*, 202(19), pp.4702–4708.

Galvan, D., Pei, Y.T. & De Hosson, J.T.M., 2006. Deformation and failure mechanism of nano-composite coatings under nano-indentation. *Surface and Coatings Technology*, 200(24), pp.6718–6726.

Gong, J. & Wilkinson, A.J., 2009. Anisotropy in the plastic flow properties of single-crystal ?? titanium determined from micro-cantilever beams. *Acta Materialia*, 57(19), pp.5693–5705.

Greer, A.L., 2009. Metallic glasses...on the threshold. *Materials Today*, 12(1–2), pp.14–22.

Han, S.M., Phillips, M.A. & Nix, W.D., 2009. Study of strain softening behavior of Al-Al3Sc multilayers using microcompression testing. *Acta Materialia*, 57(15), pp.4473–4490.

Hemker, K.J. & Sharpe, W.N., 2007. Microscale Characterization of Mechanical Properties. *Annual Review of Materials Research*, 37(1), pp.93–126.

Hickey, G.S., Lih, S. & Barbee, T., 2002. Development of Nanolaminate Thin Shell Mirrors. , 4849(December 2002), pp.63–76.

Hocheng, H., Kao, K.S. & Fang, W., 2004. Fatigue life of a microcantilever beam in bending. *Journal of Vacuum Science & Technology B: Microelectronics and Nanometer Structures*, 22(6), p.3143.

Hruby, P. et al., 2014. Fatigue crack growth in SiC particle reinforced Al alloy matrix composites at high and low R-ratios by in situ X-ray synchrotron tomography.

International Journal of Fatigue, 68, pp.136–143.

Hull, D., 1996. Interpretation of river line patterns on indentation generated fracture surfaces with comments on the fractal characteristics described by Djordjevic et al. *Journal of Materials Science Letters*, 15(8), pp.651–653.

Jaya, B.N., Kirchlechner, C. & Dehm, G., 2015. Can microscale fracture tests provide reliable fracture toughness values? A case study in silicon. *Journal of Materials Research*, 30(5), pp.686–698.

Ji, Z. et al., 2001. Metastable tetragonal zirconia formation and transformation in reactively sputter deposited zirconia coatings. *Surface and Coatings Technology*, 135(2–3), pp.109–117.

Kaira, C.S. et al., 2017. Probing Novel Microstructural Evolution Mechanisms in Aluminum Alloys Using 4D Nanoscale Characterization. *Advanced Materials*, 1703482, p.1703482.

Kelly, P.. J. & Arnell, R.. D., 2000. Magnetron sputtering: a review of recent developments and applications. *Vacuum*, 56(3), pp.159–172.

Kim, J.Y., Jang, D. & Greer, J.R., 2009. Insight into the deformation behavior of niobium single crystals under uniaxial compression and tension at the nanoscale. *Scripta Materialia*, 61(3), pp.300–303.

Kim, J.Y., Jang, D. & Greer, J.R., 2011. Nanolaminates utilizing size-dependent homogeneous plasticity of metallic glasses. *Advanced Functional Materials*, 21(23), pp.4550–4554.

Kraft, O., Schwaiger, R. & Wellner, P., 2001. Fatigue in thin films: Lifetime and damage formation. *Materials Science and Engineering A*, 319–321, pp.919–923.

Kwak, K., Otsu, M. & Takashima, K., 2010. Resonant Bending Fatigue Tests on Thin Films. *Sensors and Materials*, 22(1), pp.51–59.

Lavenstein, S. et al., 2018. Acta Materialia High frequency in situ fatigue response of Ni-base superalloy Ren e microcrystals. *Acta Materialia*, 144, pp.154–163.

Legros, M., Gianola, D.S. & Hemker, K.J., 2008. In situ TEM observations of fast grain-boundary motion in stressed nanocrystalline aluminum films. *Acta Materialia*, 56(14), pp.3380–3393.

Lekstrom, M. et al., 2008. Using the in situ lift-out technique to prepare TEM specimens on a single-beam FIB instrument. *Journal of Physics: Conference Series*, 126.

Leyland, A. & Matthews, A., 2000. On the significance of the H/E ratio in wear control: A nanocomposite coating approach to optimised tribological behaviour. *Wear*, 246(1–2), pp.1–11.

Li, J. et al., 2016. Comparison of size dependent strengthening mechanisms in Ag/Fe and Ag/Ni multilayers. *Acta Materialia*, 114, pp.154–163.

Li, N. et al., 2015. In situ Nanoindentation Study of Plastic Co-deformation in Al-TiN Nanocomposites. *Scientific Reports*, 4(111), pp.1–6.

Li, X. & Bhushan, B., 2002a. A review of nanoindentation continuous stiffness measurement technique and its applications. *Materials Characterization*, 48(1), pp.11–36.

Li, X. & Bhushan, B., 2002b. Nanofatigue studies of ultrathin hard carbon overcoats used in magnetic storage devices. *Journal of Applied Physics*, 91(10 I), pp.8334–8336.

Lide, D.R., 2008. *CRC Handbook of Chemistry and Physics 88th ed*,

Limodin, N. et al., 2009. Crack closure and stress intensity factor measurements in nodular graphite cast iron using three-dimensional correlation of laboratory X-ray microtomography images. *Acta Materialia*, 57(14), pp.4090–4101.

Liu, M.C. et al., 2013. Assessing the interfacial strength of an amorphous-crystalline interface. *Acta Materialia*, 61(9), pp.3304–3313.

Llorca, J. & Poza, P., 1994. Influence of matrix strength on reinforcement fracture and ductility in AlAl2O3composites. *Materials Science and Engineering A*, 185(1–2), pp.25–37.

Lotfian, S. et al., 2014. Effect of layer thickness on the high temperature mechanical properties of Al/SiC nanolaminates. *Thin Solid Films*, 571(P2), pp.260–267.

Lotfian, S. et al., 2012. High-temperature nanoindentation behavior of Al/SiC multilayers. *Philosophical Magazine Letters*, 92(8), pp.362–367.

Lotfian, S. et al., 2013. High temperature micropillar compression of Al/SiC nanolaminates. *Acta Materialia*, 61(12), pp.4439–4451.

Maaß, R. et al., 2009. In situ Laue diffraction of metallic micropillars. *Materials Science and Engineering A*, 524(1–2), pp.40–45.

Maekawa, S. et al., 1999. Fatigue tests of Ni-P amorphous alloy microcantilever beams. In *1999 International Microprocesses and Nanotechnology Conference*. pp. 132–133.

Maissel, L.I., Glang, R. & Budenstein, P.P., 1970. *Handbook of Thin Film Technology McGraw-Hill*,

Mara, N.A. et al., 2008. Deformability of ultrahigh strength 5 nm Cu/Nb nanolayered composites. *Applied Physics Letters*, 92(23).

Massalski, T.B., 1990. *Binary Alloy Phase Diagrams*.

Matoy, K. et al., 2009. A comparative micro-cantilever study of the mechanical behavior of silicon based passivation films. *Thin Solid Films*, 518(1), pp.247–256.

Mayer, C. et al., 2015. Micromechanical and in situ shear testing of Al-SiC nanolaminate composites in a transmission electron microscope (TEM). *Materials Science and*

Engineering A, 621, pp.229–235.

Mayer, C. et al., 2016. Orientation dependence of indentation behavior in Al-SiC nanolaminate composites. *Materials Letters*, 168, pp.129–133.

Mayer, C.R. et al., 2016. Anisotropy, size, and aspect ratio effects on micropillar compression of Al[sbnd]SiC nanolaminate composites. *Acta Materialia*, 114, pp.25–32.

Mayer, C.R., 2016. Mechanical Behavior of Al-SiC Nanolaminate Composites Using Micro-Scale Testing Methods. *PhD thesis*, (May).

McAdams, S.D., Pharr, G.M. & Oliver, W.C., 1992. Mechanical properties and microstructures of metal/ceramic microlaminates: Part II. A MO/Ai2O3 system. *Journal of Materials Research*, 7(10), pp.2774–2784.

Merkle, A.P. & Gelb, J., 2013. The Ascent of 3D X-ray Microscopy in the Laboratory. *Microscopy Today*, 21(2), pp.10–15.

Mišina, M., Musil, J. & Kadlec, S., 1998. Composite TiN-Ni thin films deposited by reactive magnetron sputter ion-plating. *Surface and Coatings Technology*, 110(3), pp.168–172.

Misra, A. & Hoagland, R.G., 2007. Plastic flow stability of metallic nanolaminate composites. *Journal of Materials Science*, 42(5), pp.1765–1771.

Mook, W.M. et al., 2013. Indentation fracture response of al–TiN Nanolaminates. *Materials Research Letters*, 1(2), pp.102–108.

Moser, B. et al., 2007. Strength and fracture of Si micropillars: A new scanning electron microscopy-based micro-compression test. *Journal of Materials Research*, 22(4), pp.1004–1011.

Movchan, B.A. & Demichishin, A. V., 1969. Study of the Structure and Properties of Thick Vacuum Condensates of Nickel, Titanium, Tungsten, Aluminum Oxide and Zirconium Dioxide. *Fiz Metallov I Metalloved*, 28(4), pp.653–660.

Musil, J. et al., 2002. Relationships between hardness, Young's modulus and elastic recovery in hard nanocomposite coatings. *Surface and Coatings Technology*, 154(2–3), pp.304–313.

Musil, J., Karvánková, P. & Kasl, J., 2001. Hard and superhard Zr-Ni-N nanocomposite films. *Surface and Coatings Technology*, 139(1), pp.101–109.

Nédélec, R. et al., 2012. Dense yttria-stabilised zirconia electrolyte layers for SOFC by reactive magnetron sputtering. *Journal of Power Sources*, 205, pp.157–163.

Nieh, T.G. & Wadsworth, J., 2008. Bypassing shear band nucleation and ductilization of an amorphous-crystalline nanolaminate in tension. *Intermetallics*, 16(9), pp.1156–1159.

Nizolek, T. et al., 2016. Tensile behavior and flow stress anisotropy of accumulative roll

bonded Cu-Nb nanolaminates. *Applied Physics Letters*, 108(5).

Okawa, R. et al., 2011. Stability Measurement of Ion Beam Current from Argon Field Ion Source. *e-Journal of Surface Science and Nanotechnology*, 9(October), pp.371–374.

Pathak, S. et al., 2015. On the origins of hardness of Cu-TiN nanolayered composites. *Scripta Materialia*, 109, pp.48–51.

Patterson, B.M. et al., 2016. In Situ Laboratory-Based Transmission X-Ray Microscopy and Tomography of Material Deformation at the Nanoscale. *Experimental Mechanics*, 56(9), pp.1585–1597.

Patterson, B.M. et al., 2014. Laboratory micro- and nanoscale X-ray tomographic investigation of Al-7 at.%Cu solidification structures. *Materials Characterization*, 95, pp.18–26.

Pei, Y.T., Galvan, D. & De Hosson, J.T.M., 2005. Nanostructure and properties of TiC/a-C:H composite coatings. *Acta Materialia*, 53(17), pp.4505–4521.

Pharr, G.M., W. C. Oliver, Pharr, G.M. & W. C. Oliver, G.M.P., 1992. W.C. Oliver 1992.pdf. *J. Mater. Res.*, 7(6), pp.1564–1583.

Phillips, M.A., Clemens, B.M. & Nix, W.D., 2003. A model for dislocation behavior during deformation of Al/Al3Sc (fcc/L12) metallic multilayers. *Acta Materialia*, 51(11), pp.3157–3170.

Physics, I., Road, B. & Lindfield, W., 1999. Fatigue Tests of Ni – P Amorphous Alloy Microcantilever Beams. *Japanese Journal of Applied Physics*, 38(12), pp.7194–7198.

Procházka, J. et al., 2004. Conditions required for achieving superhardness of ≥45 GPa in nc-TiN/a-Si3N4nanocomposites. *Materials Science and Engineering A*, 384(1–2), pp.102–116.

Raghavan, R. et al., 2014. Mechanical behavior of Cu/TiN multilayers at ambient and elevated temperatures: Stress-assisted diffusion of Cu. *Materials Science and Engineering A*, 620, pp.375–382.

Ritchie, R.O. et al., Cyclic Fatigue of Ceramics

Ritchie, R.O., 1999. Mechanisms of fatigue-crack propagation in ductile and brittle solids. In *International Journal of Fracture*. pp. 55–83.

Ross, C.A., 1994. Electrodeposited Multilayer Thin Films. *Annual Review of Materials Science*, 24(1), pp.159–188.

Schamel, M. et al., 2016. Cyclic loading for the characterisation of strain hardening during in situ microcompression experiments. *Philosophical Magazine*, 96(32–34), pp.3479–3501.

Schuster, B.E. et al., 2008. Size-independent strength and deformation mode in compression of a Pd-based metallic glass. *Acta Materialia*, 56(18), pp.5091–5100.

Sebastiani, M. et al., 2014. A novel pillar indentation splitting test for measuring fracture toughness of thin ceramic coatings. *Philosophical Magazine*, 0(0), pp.1–17.

Shen, T.D., Schwarz, R.B. & Zhang, X., 2005. Bulk nanostructured alloys prepared by flux melting and melt solidification. *Applied Physics Letters*, 87(14), pp.1–3.

Shim, S. et al., 2009. Effects of focused ion beam milling on the compressive behavior of directionally solidified micropillars and the nanoindentation response of an electropolished surface. *Acta Materialia*, 57(2), pp.503–510.

Shirley, D.A., 1972. High-resolution x-ray photoemission spectrum of the valence bands of gold. *Physical Review B*, 5(12), pp.4709–4714.

Since, I. & The, E., 1992. XPS study of a SiC film produced on St (100) by reaction.

Singh, D.R.P. et al., 2010. Micropillar compression of Al/SiC nanolaminates. *Acta Materialia*, 58(20), pp.6628–6636.

Singh, S.S. et al., 2014. *In Situ* Investigation of High Humidity Stress Corrosion Cracking of 7075 Aluminum Alloy by Three-Dimensional (3D) X-ray Synchrotron Tomography. *Materials Research Letters*, 2(4), pp.217–220.

Suzuki, Y. et al., 2012. Stability measurement of neon ion beam current emitted from supertip gas field ion source. *Technical Digest - 25th International Vacuum Nanoelectronics Conference, IVNC 2012*, pp.320–321.

Szczepanski, C.J. et al., 2013. Demonstration of an in situ microscale fatigue testing technique on a titanium alloy. *International Journal of Fatigue*, 57, pp.131–139.

Taiwo, O.O. et al., 2016. The use of contrast enhancement techniques in X-ray imaging of lithium???ion battery electrodes. *Chemical Engineering Science*, 154, pp.27–33.

Thornton, J.A., 1974. Influence of apparatus geometry and deposition conditions on the structure and topography of thick sputtered coatings. *Journal of Vacuum Science and Technology*, 11(4), pp.666–670.

Todi, R.M. et al., 2006. Investigation of oxygen annealing effects on RF sputter deposited SiC thin films. *Solid-State Electronics*, 50(7–8), pp.1189–1193.

Uchic, M.D. et al., 2004. Sample dimensions influence strength and crystal plasticity. *Science*, 305(5686), pp.986–989.

Uchic, M.D., Shade, P.A. & Dimiduk, D.M., 2009. Plasticity of Micrometer-Scale Single Crystals in Compression. *Annual Review of Materials Research*, 39(1), pp.361–386.

Ulrich, S. et al., 1997. Magnetron-sputtered superhard materials. *Surface and Coatings Technology*, 97(1–3), pp.45–59.

Unocic, K.A., Mills, M.J. & Daehn, G.S., 2010. Effect of gallium focused ion beam milling on preparation of aluminium thin foils. *Journal of Microscopy*, 240(3), pp.227–238.

Urban, R., Pitters, J.L. & Wolkow, R.A., 2012. Gas field ion source current stability for

trimer and single atom terminated W(111) tips. *Applied Physics Letters*, 100(26).

Vallabhaneni, R. et al., 2017. In situ tensile testing of tin (Sn) whiskers in a focused ion beam (FIB)/scanning electron microscope (SEM). *Microelectronics Reliability*.

Veprek, S. et al., 2000. Composition, nanostructure and origin of the ultrahardness in nc-TiN/a-Si3N4/a- and nc-TiSi2nanocomposites with Hv= 80 to ≥105 GPa. *Surface and Coatings Technology*, 133–134, pp.152–159.

Wang, C. et al., 2016. Investigation of hardness and fracture toughness properties of Fe/VC multilayer coatings with coherent interfaces. *Surface and Coatings Technology*, 288, pp.179–184.

Wang, J. et al., 2011. Interface-facilitated deformation twinning in copper within submicron Ag-Cu multilayered composites. *Scripta Materialia*, 64(12), pp.1083–1086.

Wang, J. & Misra, A., 2014. Strain hardening in nanolayered thin films. *Current Opinion in Solid State and Materials Science*, 18(1), pp.19–28.

Wang, M. et al., 2015. Size effect on mechanical behavior of Al/Si multilayers by nanoindentation. *Materials Science and Engineering A*, 644, pp.275–283.

Wasa, K., Nagai, T. & Hayakawa, S., 1976. 2.1. SiC film deposition. , 31, pp.235–241.

Wiklund, U., Hedenqvist, P. & Hogmark, S., 1997. Multilayer cracking resistance in bending. *Surface and Coatings Technology*, 97(1), pp.773–778.

Williams, J.J. et al., 2010. Damage evolution in SiC particle reinforced Al alloy matrix composites by X-ray synchrotron tomography. *Acta Materialia*, 58(18), pp.6194–6205.

Windt, D. & Bellotti, J., 2009. Performance, structure, and stability of SiC/Al multilayer films for extreme ultraviolet applications. *Applied optics*, 48(26), pp.4932–41.

Withers, P.J., 2007. X-ray nanotomography. *Materials Today*, 10(12), pp.26–34.

Yang, H. et al., 2014. In situ bending of layered compounds: The role of anisotropy in Ti 2AlC microcantilevers. *Scripta Materialia*, 89, pp.21–24.

Yang, L.W., 2017. Deformation , Strengthening and Fracture Mechanisms of Nanoscale Al / SiC Multilayers.

Yang, L.W. et al., 2016. Deformation mechanisms of ultra-thin Al layers in Al/SiC nanolaminates as a function of thickness and temperature. *Philosophical Magazine*, 96(32–34), pp.3336–3355.

Yang, L.W. et al., 2018. Mechanical properties of metal-ceramic nanolaminates: Effect of constraint and temperature. *Acta Materialia*, 142, pp.37–48.

Ye, J.C. et al., 2012. Hardness, yield strength, and plastic flow in thin film metallic-glass. *Journal of Applied Physics*, 112(5).

Zhang, J.Y. et al., 2012. Transition from homogeneous-like to shear-band deformation in nanolayered crystalline Cu/amorphous Cu-Zr micropillars: Intrinsic vs. extrinsic size effect. *Acta Materialia*, 60(20), pp.7183–7196.

Zhang, S. et al., 2005. Toughening of hard nanostructural thin films: A critical review. *Surface and Coatings Technology*, 198(1–3 SPEC. ISS.), pp.2–8.

Zimmermann, J. et al., 2010. Effects of focused ion beam milling and pre-straining on the microstructure of directionally solidified molybdenum pillars: A Laue diffraction analysis. *Scripta Materialia*, 62(10), pp.746–749.